

DISSERTATION

QUANTITATIVE COMPARISONS OF SATELLITE OBSERVATIONS AND CLOUD
MODELS

Submitted by

Fang Wang

Department of Atmospheric Science

In partial fulfillment of the requirements

For the Degree of Doctor of Philosophy

Colorado State University

Fort Collins, Colorado

Fall 2011

Doctoral Committee:

Advisor: Christian D. Kummerow

Thomas H. Vonder Haar

William R. Cotton

Jorge A. Ramírez

ABSTRACT

QUANTITATIVE COMPARISONS OF SATELLITE OBSERVATIONS AND CLOUD MODELS

Microwave radiation interacts directly with precipitating particles and can therefore be used to compare microphysical properties found in models with those found in nature. Lower frequencies (< 37 GHz) can detect the emission signals from the raining clouds over radiometrically cold ocean surfaces while higher frequencies (≥ 37 GHz) are more sensitive to the scattering of the precipitating-sized ice particles in the convective storms over high-emissivity land, which lend them particular capabilities for different applications. Both are explored with a different scenario for each case: a comparison of two rainfall retrievals over ocean and a comparison of a cloud model simulation to satellite observations over land.

Both the Goddard Profiling algorithm (GPROF) and European Centre for Medium-Range Weather Forecasts (ECMWF) one-dimensional + four-dimensional variational analysis (1D+4D-Var) rainfall retrievals are inversion algorithms based on the Bayes' theorem. Differences stem primarily from the *a-priori* information. GPROF uses an observationally generated *a-priori* database while ECMWF 1D-Var uses the model forecast First Guess (FG) fields. The relative similarity in the two approaches means that

comparisons can shed light on the differences that are produced by the *a-priori* information. Case studies have found that differences can be classified into four categories based upon the agreement in the brightness temperatures (T_b s) and in the microphysical properties of Cloud Water Path (CWP) and Rain Water Path (RWP) space. We found a category of special interest in which both retrievals converge to similar T_b through minimization procedures but produce different CWP and RWP. The similarity in T_b can be attributed to comparable Total Water Path (TWP) between the two retrievals while the disagreement in the microphysics is caused by their different degrees of constraint of the cloud/rain ratio by the observations. This situation occurs frequently and takes up 46.9% in the one month 1D-Var retrievals examined. To attain better constrained cloud/rain ratios and improved retrieval quality, this study suggests the implementation of higher microwave frequency channels in the 1D-Var algorithm.

Cloud Resolving Models (CRMs) offer an important pathway to interpret satellite observations of microphysical properties of storms. High frequency microwave brightness temperatures (T_b s) respond to precipitating-sized ice particles and can, therefore, be compared with simulated T_b s at the same frequencies. By clustering the T_b vectors at these frequencies, the scene can be classified into distinct microphysical regimes, in other words, cloud types. The properties for each cloud type in the simulated scene are compared to those in the observation scene to identify the discrepancies in microphysics within that cloud type. A convective storm over the Amazon observed by the Tropical Rainfall Measuring Mission (TRMM) is simulated using the Regional Atmospheric Modeling System (RAMS) in a semi-ideal setting, and four regimes are defined within the scene using cluster analysis: the ‘clear sky/thin cirrus’ cluster, the

‘cloudy’ cluster, the ‘stratiform anvil’ cluster and the ‘convective’ cluster. The relationship between T_b difference of 37 and 85 GHz and T_b at 85 GHz is found to contain important information of microphysical properties such as hydrometeor species and size distributions. Cluster-by-cluster comparison between the observations and the simulations discloses biases in the model including overproduction of supercooled water and large hail particles. The detected biases shed light on how the model should be adjusted to generate more realistic microphysical relationships for each cluster. Guided by the model/observation discrepancies in the ‘convective’ cloud cluster, a new simulation is performed to provide dynamic adjustments by generating more but smaller hail particles.

ACKNOWLEDGEMENTS

My foremost appreciation is extended to my advisor Professor Christian Kummerow for giving me the precious opportunity to work with him, for giving me the freedom to pursue my research interests and guiding me through it, and for teaching me to view new ideas in a critical and comprehensive way. My acknowledgements also is given to my committee members including Professors Thomas Vonder Haar, William Cotton, and Jorge Ramírez for their support, encouragement, and help all through this process. I thank Drs. Peter Bauer and Alan Geer for the ECMWF 1D+4D-Var data and for insightful discussions, Dr. Carrío Gustavo for provision of the RAMS model, Adrian Loftus, Steve Saleeby, and Dr. Kenta Suzuki for beneficial discussions on cloud microphysics, and Greg McGarragh for his tremendous help on the T-matrix implementation. I am also indebted to Drs. Greg Elsaesser, Joe Munchak, Dave Randel, Wesley Berg, Tristan L'Ecuyer, Matt Lebsock, Anita Rapp, and Sarah Ringerud for inspiring discussions. I also thank Mark Ringerud for solving all my technical problems, and Becky Burke and Amariah Lebsock for encouragement and proofreading of the manuscripts. Finally, I would like to thank my current and previous office mates including Veljko Petkovic, Kathryn Boyd, Becky Smith, Anita Rapp, and Janice Bytheway for their friendship and all the cheerful moments. I feel very lucky for belonging to this happy and fun Kummerow Research group.

Moreover, I feel that it is my privilege to be able to take classes from our department's prestigious professors and be surrounded by so many bright and self-motivated peers. I treasure all the precious friendship harvested from our department, you know who you are, and I truly appreciate it.

I surely cannot thank my dear husband Qiao Xing enough for supporting and encouraging me all the time. There were so many times of frustration for me, and it was you who accompanied me and helped me wade through all those hard times. It was you who were always there to share all the happiness with me. It was also you who helped me find myself. Thank you for being my friend and my soul mate and I hope our love lasts forever. To my daughter Mila: I love you!

Most importantly, I would like to thank my parents Xiaozhou Wang and Ruilan Huang for giving me their unconditional love whenever and wherever. Without you, nothing would have been possible. So, thank you!

TABLE OF CONTENTS

ABSTRACT.....	ii
ACKNOWLEDGEMENTS.....	v
TABLE OF CONTENTS.....	vii
LIST OF TABLES.....	x
LIST OF FIGURES.....	xi
CHAPTER 1.....	1
INTRODUCTION.....	1
1.1 Background.....	1
1.2 Objectives.....	4
1.3 Roadmap of the Dissertation.....	4
CHAPTER 2.....	5
INTERACTION WITH HYDROMETEORS AT MICROWAVE FREQUENCIES.....	5
2.1 Microwave Radiometry and Interaction with Atmospheric Constituents.....	5
2.1.1 <i>Microwave Radiometry and Microwave Imagers</i>	5
2.1.2 <i>Advantages of Microwave Radiometry</i>	9
2.1.3 <i>Interaction with Atmospheric Constituents</i>	10
2.1.3.1 ABSORPTION AND EMISSION BY ATMOSPHERIC GASES.....	10
2.1.3.2 RAYLEIGH SCATTERING REGIME.....	11
2.1.3.3 MIE SCATTERING REGIME.....	13
2.2 Radiative Transfer in a Precipitating Atmosphere.....	15
2.2.1 <i>Surface Properties</i>	15
2.2.4 <i>T-matrix for Nonspherical Particles</i>	18
2.3 Rainfall Algorithms.....	19
CHAPTER 3.....	21
COMPARING RAIN RETRIEVALS FROM GPROF WITH ECMWF 1D-VAR PRODUCTS.....	21
3.1 Introduction.....	21
3.2 GPROF <i>A-priori</i> Database and 1D-Var Retrieval Algorithm.....	23
3.2.1 <i>GPROF Rainfall Algorithm</i>	23
3.2.2 <i>Observationally Generated GPROF A-priori Database</i>	25
3.2.3 <i>ECMWF 1D+4D-Var Algorithm</i>	27
3.3 Case Studies.....	30
3.3.1 <i>Data</i>	31
3.3.2 <i>GPROF A-priori Database and 1D-Var Retrieval Comparisons</i>	33

3.3.2.1 PIXEL 1.....	35
3.3.2.2 PIXEL 2.....	37
3.3.2.3 PIXEL 3.....	41
3.4.1 <i>Data</i>	44
3.4.2 <i>Categorization</i>	44
3.4.3 <i>Microphysics Biases in Category 2</i>	47
3.4.3.1 GLOBAL MICROPHYSICS BIAS.....	47
3.4.3.2 REGIONAL DIFFERENCES.....	49
3.4.3.3 DISCUSSION.....	53
3.5 Impact of Higher Frequencies on Constraining the Cloud/rain Ratio.....	54
3.5.1 <i>Case 1</i>	56
3.5.2 <i>Case 2</i>	57
3.5.3 <i>Case 3</i>	57
3.5.4 <i>Case 4</i>	58
3.5.5 <i>Case 5</i>	58
3.5.6 <i>Case 6</i>	59
CHAPTER 4.....	60
A CLUSTERING APPROACH TO COMPARE CLOUD MODEL SIMULATIONS TO SATELLITE OBSERVATIONS.....	60
4.1 Introduction.....	60
4.2 Satellite Observation and RAMS Simulation of a Convective Event over LBA Region.....	63
4.2.2 <i>Regional Atmospheric Modeling System (RAMS) Simulation</i>	69
4.3 Cluster Analysis.....	74
4.3.1 <i>Description of Analysis</i>	75
4.3.2 <i>Determining the Number of Clusters to Use</i>	76
4.3.3 <i>The Observed Clusters</i>	79
4.4 Analysis and Discussion.....	83
4.4.1 <i>Assigning Simulation Pixels to Clusters</i>	83
4.4.2 <i>Analysis by Cluster</i>	84
4.4.2.1 T_B COMPARISONS FOR CLUSTER 1.....	86
4.4.2.2 T_B COMPARISONS FOR CLUSTER 2.....	88
4.4.2.3 T_B COMPARISONS FOR CLUSTER 3.....	90
4.4.2.4 T_B COMPARISONS FOR CLUSTER 4.....	90
4.4.3 <i>General Relationships</i>	91
CHAPTER 5.....	98
CONCLUSIONS AND FUTURE WORK.....	98
REFERENCES.....	103
APPENDIX A.....	115
IMPLEMENTATION OF T-MATRIX TO THE EDDINGTON RTM FOR STRATIFORM/CONVECTIVE SEPARATION.....	115
A.1 Introduction.....	115
A.1.1 <i>Observed Polarization Signals in Stratiform Clouds</i>	115
A.1.2 <i>Sensitivity of Polarization to Nonspherical Ice Particle Properties</i>	117
A.2 Implementation of the T-matrix Method in the Eddington RTM.....	118

<i>A.2.1 Eddington Approximation and Mie Scattering</i>	118
<i>A.2.2 T-Matrix Method</i>	120
<i>A.2.3 Implementation of the T-Matrix Algorithm in the RTM</i>	122
A.3 Examples.....	125
<i>A.3.1 Polarization Difference over One Profile</i>	127
<i>A.3.2 Discussion</i>	128
LIST OF ABBREVIATIONS.....	131

LIST OF TABLES

3.1	Bias corrected T_b departures at channel 19V, 19H, and 22V for GPROF maximum likelihood entry, ECMWF 1D-Var FG and ECMWF 1D-Var analysis.....	36
3.2	Same as in Table 3.1 except for pixel 2.....	38
3.3	Same as in Table 3.1 except for pixel 3.....	42
3.4	Percentage of each category in the database.....	46
3.5	Percentage of cases in category 2 with different CWP and RWP ratio ranges. Values in the parentheses are the percentages for GPROF surface rain rate $\geq 1 \text{ mm/h}^{-1}$	48
3.6	Sensitivity test results for all cases.....	56
4.1	Simulated T_{bs} at 19 to 85 GHz for the control simulation and six sensitivity tests	66
4.2	RAMS model configuration for the simulation.....	72
A.1	Output parameters of the T matrix code.....	122
A.2	Input parameters of the T matrix code.....	123
A.3	T_{bs} for 37 and 85 GHz using Mie code and T-matrix code individually.....	128

LIST OF FIGURES

2.1	The electromagnetic spectrum (Figure 3.1 of Petty 2006)	7
2.2	Spectrum of microwave transmittance from surface to space in the 15° Annual Atmosphere. Transmittance is the fraction of power emitted from the surface that is measured by the satellite without being absorbed by atmosphere. (http://amsu.cira.colostate.edu/spectrum.html)	8
2.3	Relationship between particle size, radiation wavelength and scattering behavior for atmospheric particles. Diagonal dashed lines represent rough boundaries between scattering regimes (Figure 12.1 of Petty 2006).....	12
3.1	(a) SSM/I 19V T_b between 0900 to 2100 UTC on 30 September 2007. (b) 19V T_b pixels used in the 1D+4D-Var assimilation. The box centered at 120°W and 10°N includes the area for further investigation.....	32
3.2	Observed T_{bs} at 19V within the area of interest. The three pixels chosen for case studies are illustrated.....	33
3.3	The GPROF retrieval weighting contour as a function of CWP and RWP, overlaid by the 1D-Var FG water paths (black triangle), 1D-Var analysis water paths (red triangle), GPROF weighted/retrieved water paths (asterisk) and GPROF maximum weighted water paths (red circle) for pixel 1. The rain rate for each retrieval is shown in the upper left box.....	35
3.4	Same as in Figure 3.3 except for pixel 2.....	38
3.5	Profiles of cloud, rain, and ice for GPROF retrieval, 1D-Var FG, and 1D-Var analysis for pixel 2.....	39
3.6	(a) The cloud and rain profiles for the T_b sensitivity test. (b) T_b sensitivity test of the emission signal to the cloud and rain ratios keeping constant liquid water content.....	40
3.7	Same as in Figure 3.3 except for pixel 3	42
3.8	Illustration of the procedure to define the match of microphysics. (a) Same as in Figure 3.3 with the dash lines showing the 20% RWP variability range. (b) The CWP distribution within the 20% RWP range. The weighted mean CWP and 95% mark on both sides are drawn	45
3.9	Normalized frequency contour of CWP ratio over RWP ratio for category 2 with (a) all rain rates and (b) rain rate ≥ 1 mm/h. The contour intervals for panel a are 1e-5, 1e-4, 1e-3, and 1e-2. The contour intervals for panel b are 0.0005, 0.001, 0.0015, and 0.002.....	47
3.10	(a) GPROF retrieved cloud/(cloud+rain) map for October 2008. (b) 1D-Var	

	FG and (c) 1D-Var analysis cloud/(cloud+rain) map for the same month. The four selected regimes are enclosed in boxes.....	50
3.11	Normalized frequency contour of CWP over RWP in category 2 for all four regimes in GPROF (left panels), 1D-Var (middle panels), and convective 1D-Var pixels (right panels).....	52
3.12	Six representative hydrometeor profiles for the case studies.....	55
4.1	The representative hydrometeor profiles including cloud, rain, pristine, snow, graupel, and hail.....	66
4.2	(left) TMI observed 85v T_b (right) and 37v T_b over a 3° by 3° scene. The 1° by 1° box enclosed by the dashed line is the focused area for this study.....	68
4.3	(left) Simulated 37 GHz and (right) 85 GHz T_b for the 1° by 1° study area at 1950 UTC during the decaying stage.....	74
4.4	T_b distributions (mean and standard deviation) at 37 GHz and 85 GHz for each cluster at the case of (a) 3 clusters, (b) 4 clusters, (c) 5 clusters, and (d) 6 clusters.....	77
4.5	Physical property comparisons for using 3 clusters (left panels), 4 clusters (middle panels), and 5 clusters (right panels) including PR surface rainfall (upper panels), 85 GHz polarization information (middle panels), and T_b relationship between 85 GHz and 37 GHz T_b s (lower panels).....	79
4.6	The 4 clusters for observation with clustering criteria defined by observation T_b scenes.....	80
4.7	VIRS (left) visible and (right) infrared image at 10.8 μm . Cluster 1 contour is overlaid.....	80
4.8	Reflectance ratio of the visible versus near-infrared channel on VIRS as a function of the cluster number with standard deviation imposed.....	81
4.9	PR reflectivity cross section at 10.3°S overlaid by the cloud type classification from PR 2A25 algorithm.....	82
4.10	Simulation clusters at T47 based on the observation cluster criteria.....	84
4.11	Mean profile of each hydrometeor species for each simulation cluster.....	85
4.12	(left) Cloud field at T35 with contour mixing ratio of 0.0 g kg ⁻¹ ; (right) Cloud (blue), aggregates (yellow), and hail (orange) fields at T47 with contour mixing ratios of 0.0 g kg ⁻¹ , 1.0 g kg ⁻¹ , and 1.0 g kg ⁻¹	86
4.13	T_b comparison of cluster 1 at each frequency between observation and simulation in which (a) surface emissivity for each channel is set to 0.93; (b) water vapor profiles are set to saturation for each pixel; (c) all cloud particles are removed; d) surface emissivities are updated for each frequency.....	87
4.14	The dT_b over $T_b(85)$ relationship comparison between the observation and the simulation (a) for cluster 2 in the control run, (b) for cluster 2 in the sensitivity test when all the supercooled water is removed, (c) for cluster 3 in the control run, (d) for cluster 3 in the sensitivity test when all the supercooled water is removed, (e) for cluster 4 in the control run, and (f) for cluster 4 in the sensitivity test when the intercept of hail PSD is increased. Diamonds stand for the observed values, overlaid by its linear regression; Gray scale contours stand for the simulated values.....	89
4.15	The relationship of dT_b over $T_b(85)$ as a function of (a) hydrometeor species,	

	(b) hydrometeor combination, and (c) hail PSD. Squares denote the cases with the same hail IWP	91
4.16	Mie extinction efficiency as a function of x for particles with different refractive indexes	92
4.17	The dT_b over $T_b(85)$ slope comparisons for cluster 4. (a) control run with hail shape parameter set to 2; (b) sensitivity run with hail shape parameter set to 5..	95
4.18	(a-n) Comparison of the mean density and number concentration N_t of cluster 4 for each hydrometeor species. (note that the scale for N_t is different for each species); (o) comparison of the mean hail D_m of cluster 4; (p) comparison of the hail mean D_m comparison for the simulation with $\nu=2, 5,$ and 10 individually	96
A.1	The selected raining scene to test the implementation.....	127

CHAPTER 1

INTRODUCTION

1.1 Background

Observations and models complement each other in many ways. Observations from ground measurements, radars, and satellites have been used to evaluate and validate models. Observed discrepancies have helped improve the models. Models, on the other hand, are used to understand the physical processes associated with the observations. Observations can also be assimilated into well-performing models as constraints. Broadly speaking, there are two approaches with which satellite observations and models can be compared: the ‘satellite-to-model approach’ and the ‘model-to-satellite approach’. In the first approach, satellite retrievals are performed to convert radiances to the physical variables that are directly used by the models. The variables may include surface rain rate and cloud properties. This approach suffers primarily from the uncertainties associated with the retrieval algorithms. In the second approach, observation operators that are usually radiative transfer models (RTMs) are used to simulate the satellite radiances (or brightness temperatures, denoted by T_b) using the model outputs so that the radiances can be compared directly. This comparison will reveal whether the model’s microphysical properties can lead to the same radiative properties. This approach avoids the retrieval

uncertainties, but is affected by errors brought in from the radiative transfer calculation processes such as the amount and placement of clouds (especially in the models with coarse resolutions, denoted as the cloud overlapping scheme or beam-filling effects), the clouds' microphysical properties (such as particle size distribution and density), and the accuracy of the RTM.

Passive microwave observations are unique in that they represent the entire column of hydrometeors in cloudy or precipitating atmospheres. Therefore, passive microwave methods bear great advantages over traditional visible and infrared imager methods. Frequencies from 10 to 85 GHz have been used in microwave imagers (e.g., Special Sensor Microwave/Imager [SSM/I] and the Tropical Rainfall Measuring Mission [TRMM] Microwave Imager [TMI]) on the polar-orbiting satellites. Lower frequencies (<37 GHz) respond to total liquid water content directly and are used in the 'emission' based rainfall retrieval algorithms over radiometrically cold ocean surfaces. Higher frequencies (≥ 37 GHz) are vulnerable to Mie scattering of precipitation-sized ice particles including snow, graupel, and hail. This 'scattering' signal is used for rainfall retrieval algorithms over land.

The focus of this study is on the comparison of cloud microphysics using passive microwave observations. Because of the direct relationship between microwave radiances and cloud microphysics, the derived microphysical properties from observations can be used to evaluate the model microphysics directly in the 'satellite-to-model' approach. These radiances can also be used as proxies of a storm's microphysical properties and T_b simulations can then be compared using the 'model-to-satellite' approach. Both approaches will be explored in this study.

An observationally generated cloud-radiation database has been built from the TRMM radar and radiometer combination aboard the TRMM satellite. The cloud database will be used as an observation database to compare with the model's cloud schemes. In this work, the 1-D cloud model in the European Centre for Medium-Range Forecasts (ECMWF) 1D+4D-Var rain retrieval algorithm over ocean is evaluated using this database to identify discrepancies of the algorithm in generating microphysics properties. The biases are discussed and solutions to mitigate the bias are investigated.

Cloud Resolving Models (CRMs) explicitly resolve convective clouds and cloud systems on fine spatial and temporal scales. They have been used to simulate individual clouds as well as mesoscale convective systems (Tao and Simpson 1989; Skamarock et al. 1994; Parker and Johnson 2004; and many others), to understand cloud and precipitation ensembles and the radiative-convective equilibrium (Zeng et al. 2008; Zhou et al. 2007; Blossey et al. 2007; and many others), to develop and even replace the cloud parameterizations in GCMs (Randall et al. 1996; Randall et al. 2003; Khairoutdinov et al. 2003), and to build *a-priori* radiative-cloud databases for physical microwave rainfall retrievals (Bauer et al. 2001, Kummerow et al. 2001; Marzano et al. 1999). However, CRMs still need parameterizations on scales smaller than their grid resolutions and have many known and unknown deficiencies. To fulfill these important applications, the robustness of CRMs in simulating cloud and rain processes must be tested against observations. In this work, the microphysics in a convective storm over land is evaluated against observations using direct satellite observations to avoid the uncertainties in the retrieved physical parameters. The identified biases in microphysics can then lead to

improvement of the simulations, especially in the microphysical parameterization schemes.

1.2 Objectives

The objective of this work is using satellite observations to quantitatively evaluate model representations of convection, and more specifically, using microwave observations to evaluate the simulated microphysics of models. Biases are identified and suggestions are given to mitigate these biases and improve the model performances.

1.3 Roadmap of the Dissertation

Chapter 2 describes the interaction of cloud microphysics with microwave frequencies in greater detail. Chapters 3 and 4 compose individual papers. Chapter 3 compares rain retrievals over the oceans from the Goddard Profiling algorithm (GPROF) with ECMWF 1D-Var products using the ‘satellite-to-model’ approach. Chapter 4 presents a clustering approach to compare cloud model simulations to satellite observation over a convective storm over land using the ‘model-to-satellite’ approach, followed by Chapter 5, which includes conclusions and future work.

CHAPTER 2

INTERACTION WITH HYDROMETEORS AT MICROWAVE FREQUENCIES

The utilization of microwave frequencies in investigating and retrieving cloud microphysics is based on the physical interactions between microwave radiation and hydrometeors within the cloud. In this chapter, these interactions and the microwave radiative transfer in a precipitating atmosphere are described, which lay down the physical basis of understanding the applications of comparing cloud microphysics in satellite observations and in model simulations in the future chapters.

2.1 Microwave Radiometry and Interaction with Atmospheric Constituents

2.1.1 *Microwave Radiometry and Microwave Imagers*

Radiometry is the measurement of electromagnetic radiation. Passive microwave sensors whose function is to measure the radiant intensity are often referred to as microwave radiometers. To understand the fundamentals of microwave radiometry, the concept of an ideal blackbody needs to be introduced. A blackbody refers to a material that absorbs all incident radiation completely at all frequencies. Matter radiates at all frequencies and an ideal blackbody radiates at frequency ν (or wavelength λ with the light speed $c = \lambda\nu$) in accordance with the Planck function in units of energy/area/time/sr/frequency, or [Watt/m²/sr/Hz]:

$$B_{\nu}(T) = \frac{2h\nu^3}{c^2(e^{h\nu/KT} - 1)} \quad \text{or} \quad B_{\lambda}(T) = \frac{2hc^2}{\lambda^5(e^{hc/K\lambda T} - 1)} \quad (2.1)$$

where,

$h = 6.626 \times 10^{-34}$ J s is the Planck constant,

$c = 3.0 \times 10^8$ m s⁻¹ is the speed of light in vacuum,

$K = 1.3806 \times 10^{-23}$ J K⁻¹ is the Boltzmann constant, and

T is the absolute temperature.

By inverting Eq. (2.1), the brightness temperature, denoted by T_b , is derived as:

$$T_b = \frac{h\nu}{K(\ln(1 + \frac{2h\nu^3}{B_{\nu}(T)c^2}))}. \quad (2.2)$$

T_b is the temperature of the blackbody that possesses the brightness of $B_{\nu}(T)$. However, in the real world, many objects such as the Earth's surface or clouds are not blackbodies and they may reflect or scatter some of the incident radiation. How 'black' is an object is described by the emissivity ϵ with $\epsilon = 1$ for a blackbody and $\epsilon < 1$ for a gray body with incomplete absorption. For a gray body, its emissivity is

$$\epsilon_{\nu} = B_{\nu}(T_b) / B_{\nu}(T). \quad (2.3)$$

Kirchhoff's Law states that upon thermodynamic equilibrium, as an object absorbs radiation, it emits a spectrum of radiation at the same temperature at the same time, and its absorptivity a_{ν} is equal to its emission ϵ_{ν} .

There is no firm definition for the exact range of the microwave region, but a reasonable convention states that the microwave spectrum extends from 0.3 to 300 GHz (1 GHz = 1 gigahertz = 10^9 Hz), that is equivalent to 1 mm to 1 m in wavelength (Ulaby et al. 1981). Figure 2.1 shows the electromagnetic spectrum.

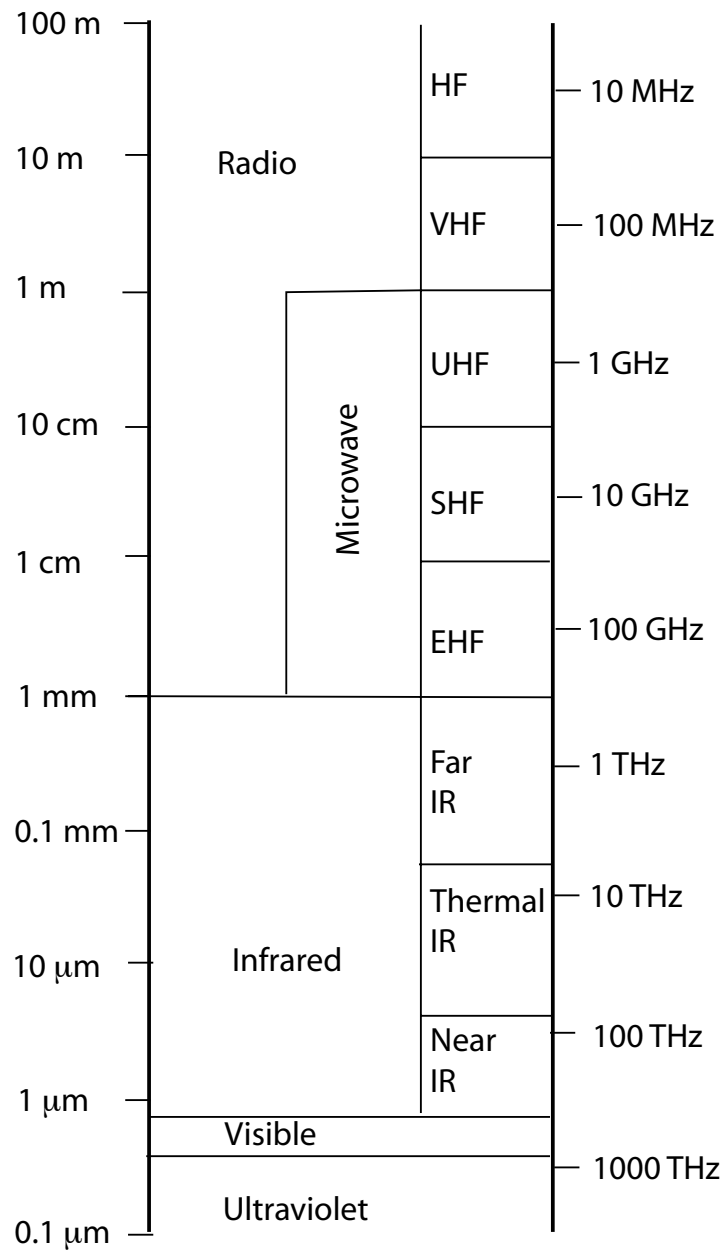


Figure 2.1 The electromagnetic spectrum (Figure 3.1 of Petty 2006).

Figure 2.2 shows the microwave total vertical transmittance through a cloud-free atmosphere. There are weakly absorbing pressure-broadened 22.235-GHz resonance water vapor lines and strong resonant water vapor absorption bands near 183.3 GHz.

There are two strong oxygen resonance absorption bands near 60 and 118.75 GHz that can be used for temperature sounding in less cloudy atmospheres. Between the absorption lines lie the window regions such as at about 31.4 GHz where the air is relatively transparent.

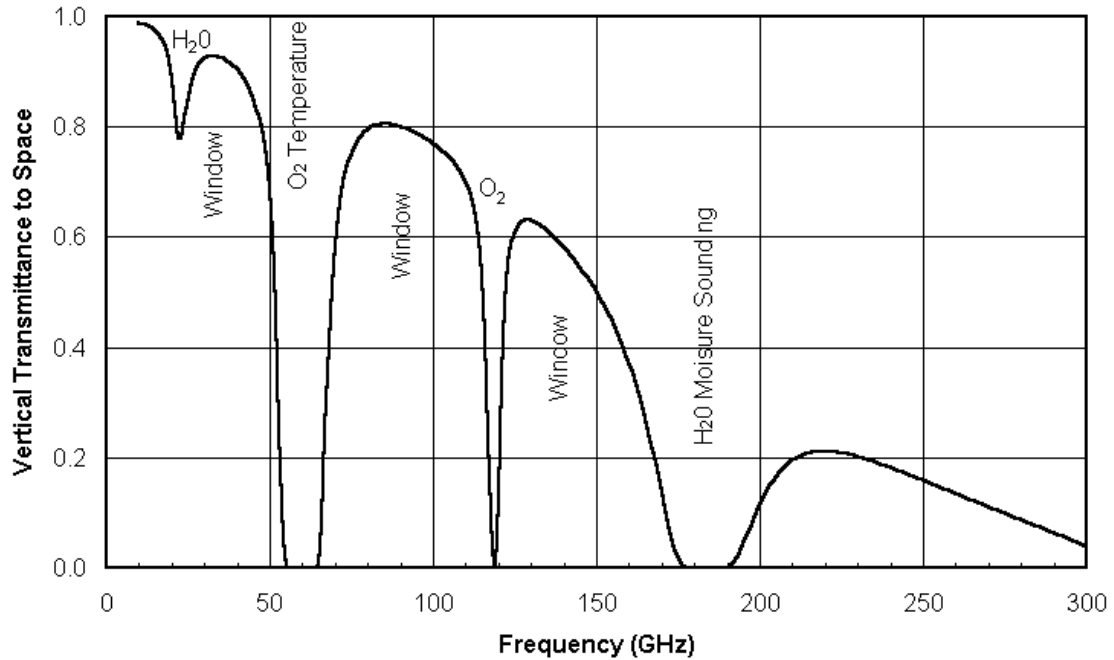


Figure 2.2 Spectrum of microwave transmittance from surface to space. Transmittance is the fraction of power emitted from the surface that is measured by the satellite without being absorbed by the atmosphere. (<http://amsu.cira.colostate.edu/spectrum.html>)

Microwave imagers utilize the transparent (window) channels so that the surface features and precipitation can be observed while microwave sounders utilize the strong rotational lines of oxygen in the 50 - 60 GHz portion and the water vapor lines around 183 GHz for temperature and humidity soundings, individually. Temperature retrieval from microwave sounders utilizes the weighting function of each oxygen band that peaks at different heights. Compared with infrared sounders, microwave radiation is less impacted by clouds and precipitation due to its longer λ . However, microwave sounding

is not the focus of this study. Two microwave imagers utilized in the following studies will be described in more details: the Special Sensor Microwave/Imager (SSM/I) and the TRMM Microwave Imager (TMI).

The SSM/I (Hollinger 1989) is carried aboard Defense Meteorological Satellite Program (DMSP) F8, F10, F11, F12, F13, and F15. It has seven separate conically scanning total-power radiometers at frequencies of 19.35, 22.235, 37, and 85.5 GHz with dual polarizations except that 22.235 GHz observes only with vertical polarization. The incidence angle is 53.1° and the spatial resolutions range from 69×43 km at 19 GHz to 15×13 km at 85 GHz.

The TRMM satellite (Kummerow et al. 1998) was launched in November 1997. It is the first mission dedicated to measure tropical and subtropical rainfall to help better understand rainfall and latent heating distributions. The orbit is inclined at 35° to maximize observations in the Tropics. TMI is a descendent of SSM/I and it measures radiance at viewing angle of approximately 53° for nine polarized channels at five frequencies of 10.65, 19.35, 21.3, 37.0, and 85.5 GHz. Detailed description of this instrument can be found in Kummerow et al. (1998).

2.1.2 Advantages of Microwave Radiometry

Microwave is advantageous over visible and infrared because its longer wavelength allows its capability to penetrate clouds, and to some extent, even rain so that the direct interactions can help establish the relationships between radiation and cloud microphysics. It therefore, provides an all-weather measurement capability.

2.1.3 *Interaction with Atmospheric Constituents*

To calculate the radiative transfer of microwave radiation through an atmosphere, it is important to know the atmosphere's state (temperature, pressure, and composition) and understand the radiative properties (absorption, emission, and scattering) of the various atmospheric constituents that interact with the radiation. This section will discuss the interactions in detail with the subsections of absorption and emission by atmospheric gases, the Rayleigh scattering regime, and the Mie scattering regime.

2.1.3.1 ABSORPTION AND EMISSION BY ATMOSPHERIC GASES

In clear-sky conditions, the absorption and emission are due solely to atmospheric gases. In the microwave spectrum, atmospheric gases and pollutants including O₂, H₂O, O₃, SO₂, NO₂, and N₂O all have absorption lines. But compared with the primary gaseous absorbers O₂ and H₂O, the relative concentration of the other gases at sea level are so small that their contributions to the microwave gaseous absorption spectrum is negligible (Ulaby et al. 1981).

As shown in Figure 2.2, the 60-GHz oxygen complex including a large number of absorption lines spreading out over the 50 to 70-GHz frequency range under pressure broadening and the transitional 118.75-GHz absorption line compose the microwave absorption spectrum of oxygen under 300 GHz. Water vapor has a weak pressure-broadened absorption line at 22.235 GHz and a strong absorption line at 183 GHz. Measurements near 22.235 GHz have been used by both SSM/I (22.235 GHz) and TMI (21.3 GHz), and column water abundance can be obtained using these measurements (Grody et al. 1980). The absorption/emission coefficients of these gases at certain frequency can be calculated given the line shapes and their concentration. In this study,

the O₂ and H₂O absorptions are calculated using Liebe's MPM93 model. The Liebe's model is an accurate physical model that calculates the attenuation introduced by atmospheric gases and its allowed frequency range extends from 1 to 1000 GHz (Liebe et al. 1993).

2.1.3.2 RAYLEIGH SCATTERING REGIME

When particles are present in the atmosphere, their interactions with radiation may involve both absorption and scattering. The significance of scattering by the particles is determined by the scattering regime in which they belong (Rayleigh, Mie, or geometric optics). The regime is defined by the value of the non-dimensional size parameter x , which describes the relative size of the particle with respect to the incident wavelength and is defined as the ratio of the particle circumference to the wavelength:

$$x \equiv \frac{2\pi r}{\lambda} \quad (2.4)$$

where, r is the radius of a spherical particle (or equivalent radius for a nonspherical particle) and λ is the incoming wavelength.

Figure 2.3 shows the scattering regimes as a function of the particle size and the wavelength. For the microwave range that is of interest to our applications (10 - 85 GHz), scattering from air molecules and atmospheric aerosols is negligible; scattering from cloud droplets (5 - 50 μm), pristine ice crystals (10 - 100 μm), and drizzle ($\sim 100 \mu\text{m}$) belongs to the Rayleigh scattering regime; scattering from rain drops (0.1 - 3 mm), graupel (0.1 - 3 mm), and hail ($\sim 1 \text{ cm}$) belongs to the Mie regime. Typical size range for each particle species is adapted from Table 12.1 of Petty (2006).

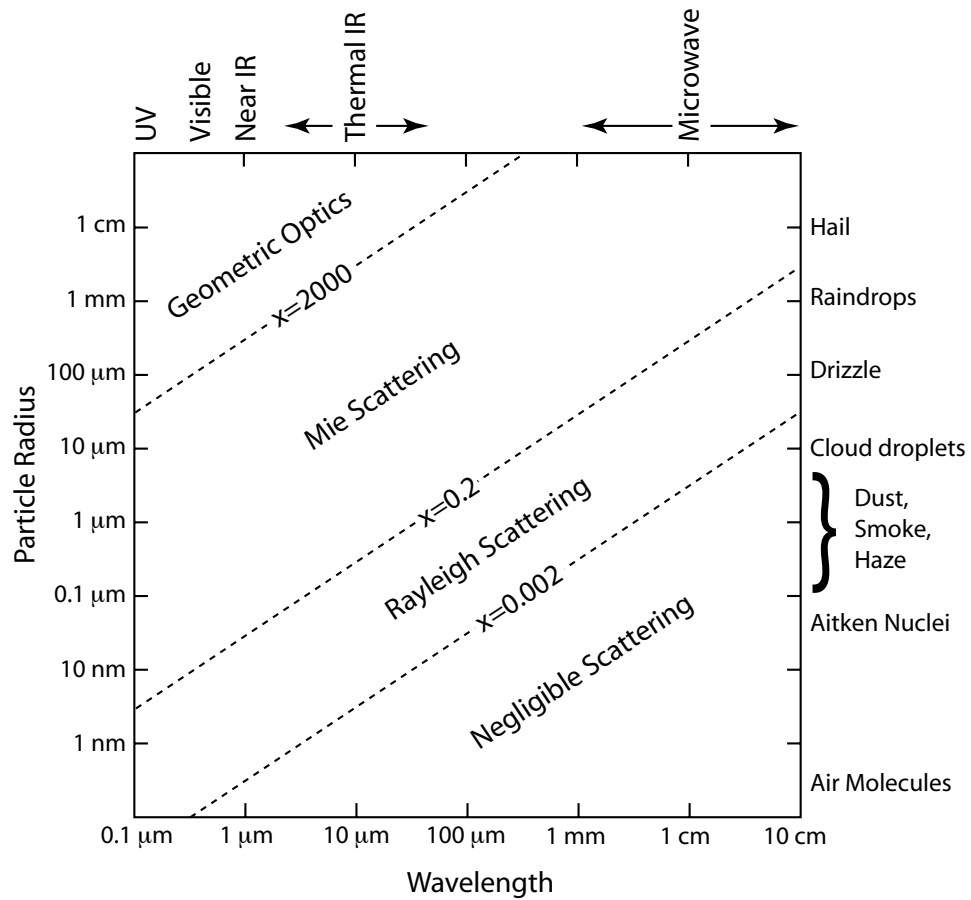


Figure 2.3 Relationship between particle size, radiation wavelength and scattering behavior for atmospheric particles. Diagonal dashed lines represent rough boundaries between scattering regimes (Figure 12.1 of Petty 2006).

Under the assumption of ‘homogeneous, isotropic, and spherical’ particles for the Rayleigh scattering regime, where $|mx \ll 1|$, in which m is the index of refraction, the corresponding scattering and absorption cross-sections Q_s and Q_a , respectively, can be expressed as:

$$Q_s = \frac{2\lambda^2}{3\pi} x^6 |K|^2 \quad (2.5)$$

$$Q_a = \frac{\lambda^2}{\pi} x^3 \text{Im}\{-K\} \quad (2.6)$$

where K is a complex quantity defined in terms of m :

$$K = \frac{m^2 - 1}{m^2 + 2} . \quad (2.7)$$

By comparing Eqs. (2.5) and (2.6), it can be seen that in the Rayleigh region where $x \ll 1$, Q_a is usually much larger than Q_s and, therefore, extinction is dominated by absorption. For example, at the frequencies that are commonly used for remote sensing of the troposphere (approximately 20 – 90 GHz), absorption exceeds scattering by at least two orders of magnitude and, therefore, the interaction of microwave radiation with cloud droplets is dominated by absorption/emission instead of scattering. The absorption coefficient is proportional to the cloud liquid water and is independent of the drop size distribution. Absorption by liquid water clouds increases with frequency monotonically. Microwaves provide the only direct means for remote-sensing of cloud water content.

However, when the particle is made of very weakly absorbing materials with m having a very small imaginary part, $\text{Im}\{-K\} \ll |K|^2$, scattering will be dominant in the extinction. For example, extinction of microwave radiation by the ice particles is mostly caused by scattering with a very large single scattering albedo even though the total extinction $Q_e = Q_a + Q_s$ is much smaller compared with that of the liquid particles.

2.1.3.3 MIE SCATTERING REGIME

As x increases with increased r and/or decreased λ , the interaction enters the Mie scattering regime where the scattering becomes more and more important and cannot be ignored. By solving the Maxwell equations for a spherical particle, the extinction and scattering efficiencies of a sphere may be written as:

$$Q_e(x, m) = \frac{2}{x^2} \sum_{n=1}^{\infty} (2n+1) \operatorname{Re}(a_n + b_n) \quad (2.8)$$

$$Q_s(x, m) = \frac{2}{x^2} \sum_{n=1}^{\infty} (2n+1) (|a_n|^2 + |b_n|^2), \quad (2.9)$$

where a_n and b_n are referred to as the Mie scattering coefficients that are functions of x and m and involve the spherical Bessel functions. Therefore, the relative importance of absorption and scattering depends both on the relative size of the particle and its properties (e.g., density). Liquid, ice, and mixed hydrometeor species are, therefore, discussed separately due to their varied dielectric properties. For the polydispersed hydrometeors, the drop/particle size distributions are important in determining the T_{bs} .

For water particles such as rain droplets, both the real and imaginary parts of m are functions of frequency and temperature (refer to Figure 5.16 in Ulaby et al. 1981) with the same order of magnitude. The real part corresponds to the scattering process and the imaginary part corresponds to the absorption process. Therefore, both scattering and absorption are important in the microwave radiation extinction process.

The refractive index of ice is smaller than that of water in the microwave region. Its real part is approximately independent of frequency and temperature at the value of 1.77. Its imaginary part changes with frequency and temperature but with a magnitude that is two orders smaller than that of its real part (Ulaby et al. 1981). Therefore, scattering is dominant in the extinction process for ice particles (e.g., hail).

Snow, aggregates, and graupel particles are all mixtures of ice crystals and dry air. Therefore, the calculation of their refractive indexes depends on their densities that are functions of the fraction of ice. The density of pure ice is 917 kg m^{-3} , and the density of a snowflake is usually between 50 and 300 kg m^{-3} depending on the percentage of the air

inclusion. Thus, for mixed hydrometeors, the extinction efficiency depends not only on the particle's size, but also on its density.

2.2 Radiative Transfer in a Precipitating Atmosphere

How radiation travels through a precipitating atmosphere is described in this section. Satellite observations using microwave radiometers that operate near the window regions are strongly affected by surface emissivity, which varies greatly over different surfaces.

2.2.1 Surface Properties

The observed microwave radiances at the Top Of the Atmosphere (TOA) may consist of radiation from both the Earth's surface and the atmospheric constituents. The contribution from the surface depends on the surface type and its temperature. The surface emissivity ε is a key parameter for the interpretation of satellite microwave data and is a function of frequency, polarization, incident angle, index of refraction of the surface, and the surface roughness. Ocean and land surfaces need to be treated separately due to their distinct differences in the emissivities. Usually, the ε over both land and ocean varies by about 10% from its mean value (Grody 1993).

Over ocean, ε is modeled as a function of surface temperature, salinity, and the near-surface wind speed and foam that are closely related to the surface roughness caused by wind-driven waves. The model of Wilheit (1979) is used in this study to account for the wind speed. The Wilheit model is a physically based sea surface emissivity model that considers the sea surface emissivity as a combination of the emissivity given by an ensemble of flat facets and the reduction of the facets due to a layer of absorbing nonpolarized foam.

ε over land is highly variable and depends on many surface characteristics including the surface composition (soil type, soil moisture, snow cover, and vegetation cover) and surface geometry (incident angle, surface roughness, canopy geometry, and topography) (Prigent et al. 1997; Lin and Minnis 2000; Prigent et al. 2006). Over most land surfaces, high ε makes it difficult to separate atmospheric contribution from the total signal observed by the spaceborne sensors. Microwave land emissivity models are being built (Weng et al. 2001; Bytheway and Kummerow 2010) for the benefit of many applications including physical land rainfall retrievals.

2.2.2 Radiative Transfer

The theory of radiative transfer is concerned with the equilibrium balance between the radiation emitted, absorbed, and scattered throughout the atmosphere. The radiative transfer equation at frequency ν in a local thermodynamic equilibrium is given by:

$$\begin{aligned}
 I_{\nu}(\tau; \mu, \phi) = & \varepsilon_{\nu} B_{\nu}(T_s) \mathbf{T}_{\nu}(p_s, 0) + (1 - \varepsilon_{\nu}) \mathbf{T}_{\nu}(p_s, 0) \int_0^{p_s} B_{\nu}[T(p)] \frac{\partial \mathbf{T}_{\nu}(p_s, p)}{\partial p} dp \\
 & + \int_{p_s}^0 B_{\nu}[T(p)] \frac{\partial \mathbf{T}_{\nu}(p, 0)}{\partial p} dp + \frac{\omega}{4\pi} \int_0^{2\pi} \int_{-1}^1 I(\tau; \mu', \phi') P(\mu, \phi; \mu', \phi') d\mu' d\phi'
 \end{aligned}
 \tag{2.10}$$

where,

I is the radiance,

τ is the optical depth,

μ is the cosine of the zenith angle,

ϕ is the azimuth angle,

ε is the surface emissivity,

B is the Planck function,

T stands for temperature and T_s is the surface temperature,

T is the transmittance,

p stands for pressure and p_s is the surface pressure,

ω is the single scattering albedo, and

P is the phase function.

The radiances I_ν observed at TOA in the direction of μ and ϕ is composed of the contributions from: surface emission (term 1 in the RHS), reflection of downward atmospheric emission by the surface into the atmosphere (term 2 in the RHS), the atmospheric emission (term 3 in the RHS), and scattering of radiation from other directions to the observing direction (term 4 in the RHS).

In the microwave regime with frequency less than 100 GHz, at terrestrial temperatures of 300 K and below, considering the low-frequency limit ($h\nu/KT \ll 1$ or $\lambda \sim 1$ mm or longer), Rayleigh-Jeans approximation applies and allows the Planck function to be simplified as:

$$B_\nu(T) \cong (2\nu^2 K / c^2) T. \quad (2.11)$$

The significant feature of Eq. (2.11) is that the Planck radiance is proportional to the physical temperature of the object. This approximation significantly simplifies the radiative transfer calculations and sensor calibration relationships in the microwave band.

An equivalent brightness temperature T_b is defined such that

$$I_\nu = (2\nu^2 K / c^2) T_b(\nu). \quad (2.12)$$

Replacing $B_\nu(T)$ and I_ν into the RTE of Eq. (2.10):

$$\begin{aligned}
T_b(\nu) = & \epsilon_\nu T_s \mathbf{T}_\nu(p_s, 0) + (1 - \epsilon_\nu) \mathbf{T}_\nu(p_s, 0) \int_0^{p_s} T(p) \frac{\partial \mathbf{T}_\nu(p_s, p)}{\partial p} dp \\
& + \int_{p_s}^0 T(p) \frac{\partial \mathbf{T}_\nu(p, 0)}{\partial p} dp + \frac{\omega}{4\pi} \int_0^{2\pi} \int_{-1}^1 I(\tau, \mu', \phi') P(\mu, \phi; \mu', \phi') d\mu' d\phi'
\end{aligned} \quad (2.13)$$

2.2.3 Eddington Approximation

Diffusion approximation can be made with multiple scattering since there is no directional dependence. It is appropriate to consider the transfer of hemispheric upward and downward flux densities F^\uparrow and F^\downarrow so that the coefficients in the solutions of the RTE can be analytically solved and efficient computations can be carried out, which is critical in many general circulation and climate models. This simplification is made in the two-stream and Eddington approximations. More details of Eddington approximation is described in the Appendix Section A.2.1.

2.2.4 *T*-matrix for Nonspherical Particles

For smaller raindrops, the shapes are nearly spherical where surface tension dominates over hydrodynamic forces; while larger drops exhibit nonspherical behavior. The differences between assuming spherical drops and accounting for the nonspherical nature of raindrops are usually smaller than the statistical uncertainties due to other parameters such as the drop-size distribution (Ulaby et al. 1981). Ice particles exist with a wide range of habits, while RTMs often use a spherical ice shape due to simplicity and lack of more suitable models. However, the particle's shape may play a large role in determining its radiative properties and is found to be able to cause polarization differences of up to 10 K at 85 GHz in stratiform-anvil regions of Mesoscale Convective Systems (MCSs). Spencer et al. (1983) observed a polarization difference of 10 to 12 K

at 37 GHz at heavy rain events that can only be explained by the nonspherical shape of the particles. The polarization differences have been utilized in stratiform/convective separation algorithms including Anagnostou and Kummerow (1997), Hong et al. (1999), Olson et al. (2001), and Varma and Liu (2010). Therefore, to simulate this polarization signal, the nonspherical shape of the snow and aggregate particles in the stratiform anvil need to be considered. The T-matrix method was implemented and the details of implementation are described in Appendix A.

2.3 Rainfall Algorithms

The relationships between microwave radiation and cloud microphysics have been utilized in the rainfall retrieval algorithms. Different relationships at different frequencies have been utilized for over ocean and over land. Generally speaking, the techniques to extract rainfall signature at microwave frequencies primarily rely on the emission signals from raindrops at frequencies at or below 37 GHz over the oceans where thermal emission from liquid water droplets dominate the atmospheric effects; and the scattering signals from precipitating ice particles at frequencies at or above 37 GHz over land where propagation of microwave radiation is affected by the interactions with ice particles. Specifically, passive microwave rainfall algorithms generally fit in one of the following three classes (Kummerow et al. 2007): 1) the emission type algorithms (Wilheit et al. 1991; Berg and Chase 1992; Chang et al. 1999) that use the warm signals from raining cloud over radiometrically cold ocean surfaces; 2) the scattering type algorithms (Spencer et al. 1983; Grody 1991; Ferraro and Marks 1995) that correlate rainfall with T_b depressions that are caused by Mie scattering of the precipitation-sized ice particles above the rain layer, this is a less direct measurement compared with the

emission approach, but it is applicable in a wide range of rain events; and 3) the multichannel inversion type algorithms (Olson 1989; Mugnai et al. 1993; Kummerow and Giglio 1994; Smith et al. 1994; Petty 1994; Bauer et al. 2001; Kummerow et al. 2001) that invert the observed radiances simultaneously to retrieve the rain parameters. The application of the inversion type of algorithms over land requires sophisticated surface emissivity models.

Accordingly, for the applications utilizing microwave imagers (TMI or SSM/I), lower frequency channels (e.g., 10, 19, 22 GHz) are used for ocean scenes such as in Chapter 3 and higher frequency channels (e.g., 37 and 85 GHz) are used for land scenes such as in Chapter 4.

CHAPTER 3

COMPARING RAIN RETRIEVALS FROM GPROF WITH ECMWF 1D-VAR PRODUCTS

3.1 Introduction

Accurate rainfall measurements over the oceans are crucial for many applications and microwave radiometers provide physically reasonable rainfall estimates due to the direct interaction of the radiation with water in the rain column. Passive microwave rainfall algorithms generally fit into one of the following three classes (Kummerow et al. 2007): 1) the emission type algorithms (Wilheit et al. 1991; Berg and Chase 1992; Chang et al. 1999) that use the warm signals from raining cloud over radiometrically cold ocean surfaces; 2) the scattering type algorithms (Spencer et al. 1983; Grody 1991; Ferraro and Marks 1995) that correlate rainfall with T_b depressions that are caused by Mie scattering of the precipitation-sized ice particles in the raining clouds; and 3) the multichannel inversion type algorithms (Olson 1989; Mugnai et al. 1993; Kummerow and Giglio 1994; Smith et al. 1994; Petty 1994; Bauer et al. 2001; Kummerow et al. 2001) that invert the observed radiances simultaneously to retrieve the rain parameters.

The future Global Precipitation Mission (GPM, Kummerow et al. 2007; Hou et al. 2008) will utilize all available polar orbiting satellites, supplemented with a core satellite

that will utilize a Dual-frequency Precipitation Radar (DPR) with a multichannel microwave imager (GMI) to provide frequent, global, and accurate precipitation measurements. To avoid configuration-dependent retrieval biases between the sensors, a transparent and parametric algorithm that is based on the same physical principles is being developed that does not depend on specific frequencies and therefore ensures uniform rainfall products across all sensors (Kummerow et al. 2007). This requirement confines the adoptable algorithms only to those that involve physical forward/inverse modeling. The Goddard Profiling Algorithm (GPROF, Kummerow et al. 2001) approach has been utilized for TRMM Microwave Imager (TMI), Special Sensor Microwave Imager (SSM/I) and Advanced Microwave Scanning Radiometer – Earth Observing System (AMSR-E) and served as a prototype for a single retrieval approach (Ferraro 2007). ECMWF in the meantime, has begun assimilating radiances corresponding to raining scenes using the Bauer et al. (2001a, 2006a) radiative transfer and a retrieval algorithm referred to as 1D+4D-Var (Bauer et al. 2006b,c).

Both algorithms are based on the Bayes' theorem but vary in the implementation process such as *a-priori* information, usage of frequencies, and algorithm formulation. The most recent version of GPROF relies on an observationally generated database of precipitation profiles that uses a combination of active and passive microwave sensors (Kummerow et al. 2011). This database constitutes a pseudo-observational microphysics space that defines the cloud/rainwater path ratios that have been observed using the active/passive microwave combination flying on TRMM.

These 'observations' are compared to the ECMWF results. Generally, there are two approaches to perform the comparisons between observations and models: the

‘satellite-to-model’ approach and the ‘model-to-satellite’ approach. In the first approach, retrievals are performed to convert satellite observations to model output variables (e.g., Zhou et al. 2007; Geer et al. 2008). In the second approach, observation operators such as Radiative Transfer Models (RTMs) are used to simulate observed radiances or T_b s from the model variables (e.g., Panegrossi et al. 1998; Chaboureau et al. 2002; Chevallier and Kelly 2002; Chevallier and Bauer 2003; Matsui et al. 2009). However, both approaches ultimately lead to comparing either rainfall or radiance maps where the comparison in radiance space has the advantage that at least the observations are very accurately known. In conducting this research, we seek to better understand the microphysical properties that lead to differences in the GPROF and ECMWF rainfall, particularly for cases where both methods successfully minimize the differences between the model and the observed T_b . Detailed descriptions of the GPROF and 1D-Var algorithms are provided in Section 3.2. Comparisons between them using case studies are depicted in Section 3.3, while the statistical analyses of the differences are examined and analyzed in Section 3.4. In Section 3.5, solutions to resolve the discrepancies are proposed.

3.2 GPROF *A-priori* Database and 1D-Var Retrieval Algorithm

3.2.1 GPROF Rainfall Algorithm

GPROF is a Bayesian retrieval scheme, which is currently used operationally for radiometers such as TMI, SSM/I, and AMSR-E. GPROF aims to retrieve the instantaneous rainfall and the rainfall vertical structure from the satellite microwave observations. The original algorithm is described in Kummerow et al. (1996) and was further extended to include the latent heating estimation (Olson et al. 1999).

Rainfall retrieval from passive microwave radiances is an ill-conditioned inverse problem in the sense that the total information content of the observations is less than the independent variables within raining clouds that must be retrieved. Therefore, there is no unique solution that can be obtained without introducing prior knowledge and the derived solution may even be non-optimal. The Bayesian theorem provides a rigorous mathematical formulation to introduce this *a-priori* knowledge. Following Bayes' formulation, the probability of observing a particular hydrometeor profile \mathbf{R} , given the observed brightness temperature vector T_b can be written as:

$$Pr(\mathbf{R} | T_b) = Pr(\mathbf{R}) \times Pr(T_b | \mathbf{R}), \quad (3.1)$$

where $Pr(\mathbf{R})$ is the probability of observing a certain rain profile \mathbf{R} and $Pr(T_b|\mathbf{R})$ is the probability of observing T_b given a particular rain profile \mathbf{R} .

Older versions of GPROF used Cloud Resolving Models (CRMs) to define $Pr(\mathbf{R})$. $Pr(T_b|\mathbf{R})$ in those versions of GPROF was calculated from the CRM output using a Radiative Transfer Model (RTM). More details of the CRMs and the RTM applied in GPROF are described in Kummerow et al. (2001). In practice, the available sets of CRM simulations constituted the assumed *a-priori* probability of finding a particular profile \mathbf{R} in nature. In the retrieval process, given an observed T_b , profiles in the database that have consistent simulated T_b will be selected and weighted to give the expected value that is considered to be the 'best' estimate. With \mathbf{x} representing the vector of all the physical quantities to be retrieved, the expected value of \mathbf{x} is given by:

$$\hat{\mathbf{E}}(\mathbf{x}) = \sum_i \mathbf{x}_i \frac{\exp\{-0.5[\mathbf{y} - \mathbf{H}(\mathbf{x}_i)]^T (\mathbf{O} + \mathbf{S})^{-1} [\mathbf{y} - \mathbf{H}(\mathbf{x}_i)]\}}{A}, \quad (3.2)$$

where \mathbf{x}_i represents all model simulated profiles in the database, \mathbf{y} represents the observation vector, $H(\mathbf{x}_i)$ is the simulated observation vector corresponding to profile \mathbf{x}_i with H representing the observation operator, \mathbf{O} and \mathbf{S} are the observation and model error covariance matrices, respectively, and A is the normalization factor, which is a scalar constant. For further descriptive details relating to the retrieval process see Kummerow et al. (1996) and Kummerow et al. (2001).

This algorithm has undergone many improvements over the years. Examples include an improved freezing level over oceans to reduce the artificially high rainfall at high latitudes, improved convective-stratiform discrimination to significantly decrease the precipitation in stratiform areas especially in areas far from convection, including melting layers in the RTM (Bauer 2001b), and use of improved rainfall relationship over land (Kummerow et al. 2001). Recently, an important improvement consisted of replacing the original CRM-based database with an observationally-generated database (Kummerow et al. 2011). The choice of database is very important because it is assumed that the database accurately represents the true probability of observed situations.

3.2.2 Observationally Generated GPROF A-priori Database

The traditional databases generated by CRM simulations suffered from issues including the correctness and completeness issues described in Kummerow et al. (2006). To avoid these shortcomings, an observationally-generated database of precipitation profiles has been constructed using the combination of active and passive microwave sensors (i.e., the Precipitation Radar [PR] and TRMM Microwave Imager [TMI] on board the Tropical Rainfall Measuring Mission [TRMM] satellite; Kummerow et al. 1998).

One year of TRMM observations of TMI and PR from 1 June 1999 to 31 May 2000 were used to build the database. The TRMM operational PR algorithm (TRMM 2A25, V6) was used as the starting point. When PR indicated no rain, an optimal estimation procedure was used to retrieve nonraining geophysical parameters including surface wind, Total Precipitable Water (TPW) and cloud Liquid Water Path (LWP) from the TMI observations (Elsaesser and Kummerow 2008). The Sea Surface Temperature (SST) is specified from the Reynolds weekly climatology (Reynolds et al. 2002). When PR indicates rain, the TRMM 2A25 rainfall profiles are used as the first guess. The SST and wind speed are interpolated from the neighboring nonraining fields. Cloud water, water vapor and profiles of rain and ice hydrometeors are obtained by matching radar profiles to CRM. When matched, CRM hydrometeor profiles are used. This step is important in that the CRM provides a first guess for cloud liquid and cloud ice water content that are not sensed directly by the PR. RTMs are used to compute the simulated T_b s from these hydrometeors and the resulting T_b s are compared to coincident TMI observations. Comparisons are accumulated as a function of SST and TPW at 1 K and 1 mm intervals. Where disagreements at 19 and 85 GHz vertically polarized T_b s occurred, an adjustment procedure was performed by first adding rainwater that is below the detection threshold of the PR. If the addition of light rain did not correct mean biases, the adjustment procedure then focused on rain drop size distributions and ice density to match the modeled and observed T_b . The adjusted profiles are then adopted for the database construction. Complete details of the procedure, which is only summarized here, can be found in Kummerow et al. (2011). The one-year pseudo-observed microphysical database will be used to evaluate the modeled microphysics. It should be noted here that

because the PR is sensitive primarily to precipitation while TMI is sensitive primarily to TPW, there is good reason to assume that the rain and cloud water amounts may, to the first order, be representative of observed clouds.

3.2.3 ECMWF 1D+4D-Var Algorithm

The ECMWF 1D+4D-Var algorithm has been operational since June 2005 (Bauer et al. 2006b,c; Geer et al. 2008) over cloudy and rainy SSM/I observations and may be considered as an intermediate step towards the direct 4D-Var assimilation of all-sky microwave radiances, which was made operational in March 2009 (Bauer et al. 2010; Geer et al. 2010). The 1D+4D-Var algorithm includes two parts: the 1D-Var that includes an optimal estimation procedure to retrieve the microphysical properties and TPW from SSM/I radiance observations, and the 4D-Var analysis (Rabier et al. 2000) that assimilates the TPW as a pseudo-observation. The observation operator includes three components: a convection scheme that represents subgrid-scale processes and treats convection types defined as shallow, mid-level and deep convection in a unified way; a large-scale condensation scheme that uses the convective detrainment prescribed by the convection model with a similar precipitation generation formulation; and a multiple-scattering radiative-transfer model RTTOV-SCATT (Bauer et al. 2006a) with scattering calculated using the delta-Eddington approach. The advantage of the 1D-Var over ordinary variational retrievals is that it uses the same background state, background errors, and moist physics package as the 4D-Var (Bauer et al. 2010). Therefore, its *a-priori* information (short-range forecast) is more accurate than the statistical climatology as it contains information about physically important features such as fronts, inversions, and the tropopause heights. Using 1D-Var allows an extra step of quality control before

assimilating radiances into 4D-Var (Bauer et al. 2010). An important aspect of the 1D-Var retrieval is that the control vector consists of temperature and humidity profiles as well as surface wind speed. Cloud and precipitation are calculated from the moist physics parameterizations before running a radiative transfer scheme. The optimization is thus constrained by the models, the observations and the background fields for temperature, moisture and wind speed with associated errors and not by model background cloud/precipitation fields and their errors.

The processing of rain-affected SSM/I T_b s used in 1D-Var retrieval involves several steps including: removing the scan-position-dependent biases known to affect SSM/I, a pre-screening process including a land surface and sea-ice check, a check for valid T_b observations, and the screening of clear-sky observations not to be treated in the retrieval. A check for cloud liquid water and precipitation presence is applied that is based on a cloud identification algorithm (Karstens et al. 1994) and the polarization signal at 37 GHz. A check of excessive falling snow in the 1D-Var FG profile is also performed to avoid unreliable radiative transfer simulations in such conditions (Geer et al. 2007). Then the bias correction is performed that is a correction of systematic differences between observed and simulated T_b s (Bauer et al. 2006b).

In general, it is not uncommon for simulations to have large biases compared to the observations, and it is crucial to correct these biases for achieving good assimilation results. A multiple linear regression between FG departures (observation minus FG) and FG TWP, surface wind speed, and column rain amount is performed to predict the biases in the 1D+4D-Var system. The bias correction is then applied to the observation T_b s to make them less biased with respect to the 1D-Var FG prior to the assimilation (Geer et al.

2008). The bias correction is applied to the 19-GHz vertical polarization channel (shortened as 19V hereafter), 19-GHz horizontal polarization channel (shortened as 19H hereafter), and 22V.

The bias correction scheme may not be proper for cloudy observations because of the usage of an asymmetric predictor (Geer and Bauer 2011) that is the FG rain amount in the 1D+4D-Var system. Some biases are very large, and they may be due to errors in the structure and intensity of forecast cloud and rain, but may also be due to displacement errors. The largest error might be coming from the improper cloud overlap scheme (Geer et al. 2009) in which assumptions regarding the subgrid-scale cloud variability are made. These are known as beam filling biases in the satellite community.

The model forecast provides the FG fields including temperature profiles, water vapor profiles, surface fields, which include latent heat and sensible heat fluxes, and wind stress. These FG fields all serve as inputs to the convection scheme that in turn produces detrained convective cloud water, and rain and snow fluxes. Together with the FG fields and the detrained cloud water, the large-scale condensation scheme produces cloud-cover fraction and models the clouds and precipitation when they are formed by model-resolved processes. Using the thermodynamic and hydrometeor information generated above, the multiple-scattering microwave RTM is used to calculate the simulated radiances.

In a variational retrieval (e.g., Rodgers 2000), the optimal estimation of a state vector \mathbf{x} is acquired by minimization of a cost function using the *a-priori* information from the FG. The cost function J is defined as:

$$J(\mathbf{x}) = (\mathbf{x} - \mathbf{x}_b)^T \mathbf{B}^{-1} (\mathbf{x} - \mathbf{x}_b) + (\mathbf{y} - \mathbf{H}[\mathbf{x}])^T \mathbf{R}^{-1} (\mathbf{y} - \mathbf{H}[\mathbf{x}]), \quad (3.3)$$

where J is the cost function, \mathbf{x} is the state vector, containing vertical profiles of temperature and specific humidity on 91 model levels in this case, \mathbf{x}_b is the *a-priori* state vector acquired from model simulation, \mathbf{y} is the observation vector, \mathbf{H} stands for the observation operator that maps geophysical space to observational space, \mathbf{B} is the background error covariance matrix, \mathbf{R} is the observation error covariance matrix, which includes both the observation error and the errors originating from observation operators.

The first term is the fit of the solution to the background estimate of the atmospheric state weighted inversely by the background error covariance \mathbf{B} . The second term is the fit of the solution to the measured radiances \mathbf{y} weighted inversely by the measurement error covariance \mathbf{R} . The solution obtained is optimal in that it fits the *a-priori* (or background) information and measured radiances respecting the uncertainty in both.

1D-Var produces outputs including vertical profiles of humidity, temperature, cloud and precipitation. The TPW derived from the retrieved humidity profile is assimilated in the main 4D-Var analysis (Rabier et al. 2000). It should be noted that the 1D+4D-Var algorithm is affected by a sampling bias, which comes from applying 1D+4D-Var when the observations are cloudy or rainy, but not when the FG is rainy or cloudy and the observations are clear (Geer et al. 2008).

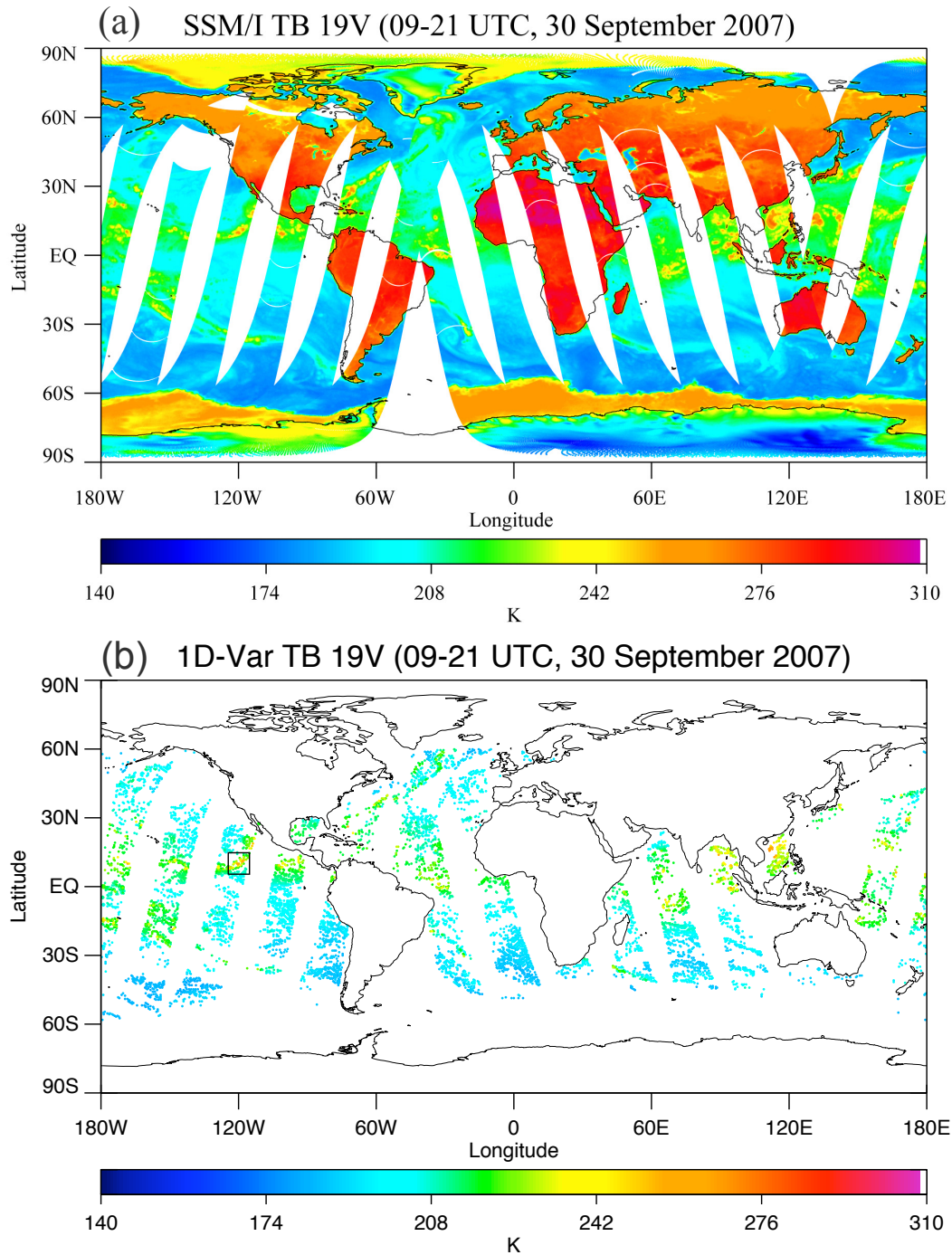
3.3 Case Studies

Comparing the GPROF retrieval in Eq. (3.2) and the 1D+4D-Var assimilation in Eq. (3.3), one can see that these two methods are very similar in the sense that they are both performing under-constrained retrievals given the observations. Both methods use *a-priori* information. The primary differences are: 1) the GPROF retrieval is constrained by

the observation database consisting of PR/TMI observations and CRM simulations, while 1D-Var retrieval is constrained by the ECMWF model's FG and the 1D cloud model; 2) the \mathbf{x} to be minimized in GPROF represents the microphysics profiles, while in 1D-Var it represents the thermodynamic profiles. In this section, detailed comparisons of the retrievals are made utilizing several case studies.

3.3.1 Data

Data collected within a 12-hour window extending from 0900 to 2100 UTC on 30 September 2007 are used in this case study. The data are based on a T511 run using the default configuration of cycle 35r1 of the Integrated Forecasting System (IFS) and include 6619 1D-Var retrievals over the ocean between 60°S and 60°N. The product consists of SSM/I T_b vectors, thermodynamic profiles, and microphysical profiles of cloud liquid water, cloud ice water, rain flux, and snow flux at 91 levels for both the FG and the analysis generated in the 1D-Var observation operator. Figure 3.1a shows the SSM/I 19V T_b for 30 September 2007, while Figure 3.1b shows the 19V T_b for all the pixels that are used in the assimilation. Over the ocean, the background is radiometrically cold due to its low emissivities. Emissions from water vapor, clouds, and rain will increase the 19-GHz T_b and, therefore, appear warmer against the background (Chevallier and Bauer 2003).



A 10° by 10° area at [115°W, 125°W] and [5°N, 15°N] as shown in the enclosed box in Figure 3.1b, was selected for the case study. Pixels from this area are expanded in Figure 3.2. Three representative pixels along a line are chosen to include a variable range of T_b values for case studies, as illustrated in Figure 3.2.

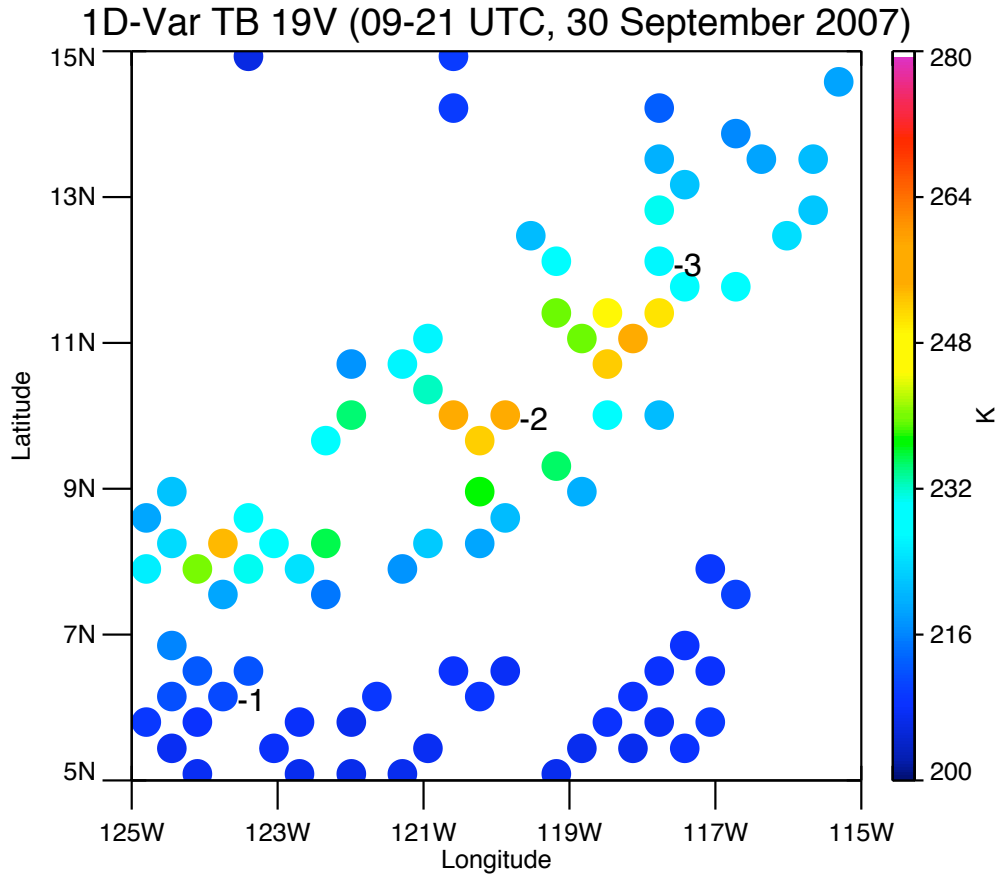


Figure 3.2 Observed T_b s at 19V within the area of interest. The three pixels chosen for case studies are illustrated.

3.3.2 GPROF A-priori Database and 1D-Var Retrieval Comparisons

In the 1D-Var retrieval algorithm, only the lower frequency channels including 19V, 19H, and 22V are used. The higher frequencies are not used due to the non-Gaussian shape of the histogram of FG departures, the complexity of nonlinearity in the

RTM, and the sensitivity to surface emissivity modeling biases (Bauer et al. 2006b). Accordingly, the observation vector \mathbf{y} in Eq. (3.2) was modified to include only those three channels in the GPROF retrieval as well. Given an observation T_b vector \mathbf{y} , each entry in the *a-priori* database \mathbf{x}_i within the TPW and SST ranges (TPW is defined by the 1D-Var analysis field and SST is defined by climatology) is assigned a weighting based on the closeness between the simulated T_b vector $H(\mathbf{x}_i)$ and the observation T_b vector \mathbf{y} . From Eq. (3.2), the *weighting* for entry \mathbf{x}_i can be expressed as:

$$weighting = \frac{e^{-\sqrt{\sum_{j=1}^3 0.5[\mathbf{y}_j - H(\mathbf{x}_i)_j]^T (O_j + S_j)^{-1} [\mathbf{y}_j - H(\mathbf{x}_i)_j]}}}{A} \quad (3.4)$$

where j is the channel number. Gaussian error distribution is assumed and O_j and S_j are the diagonal values of the error covariance matrices (off-diagonal elements are not taken into account because it is assumed that the errors of different channels are uncorrelated).

Eq. (3.4) indicates that more similar T_b vectors will receive larger weight. It will be assigned a greater weight in the final solution than a pixel whose T_b s differ significantly. All the possible solutions defined by the database within given TPW and SST ranges are considered by using the normalized weighting to produce a statistically averaged GPROF retrieval. The entry that produces the closest T_b vector is called the ‘GPROF maximum likelihood’, which has the highest probability of being the solution. Comparisons between GPROF retrieval and 1D-Var retrieval are made for all of the selected pixels, and the results for pixels 1, 2, and 3 as shown in Figure 3.2 are discussed in the following subsection.

3.3.2.1 PIXEL 1

Given TPW and SST, the gray envelope in Figure 3.3 represents the range of selected *a-priori* database profiles with respect to Cloud Water Path (CWP) and Rain Water Path (RWP) for the retrieval of this pixel using a cut-off weighting of 0.01. A cut-off weight of 0.01 as defined in Eq. (3.4) is used to eliminate entries that are too dissimilar to the observations. The relationship between CWP, RWP, and Ice Water Path (IWP) is considered separately. The basic envelope constitutes a pseudo-observation space (that is, for a given 3-channel T_b vector, this is what PR/TMI considers to be

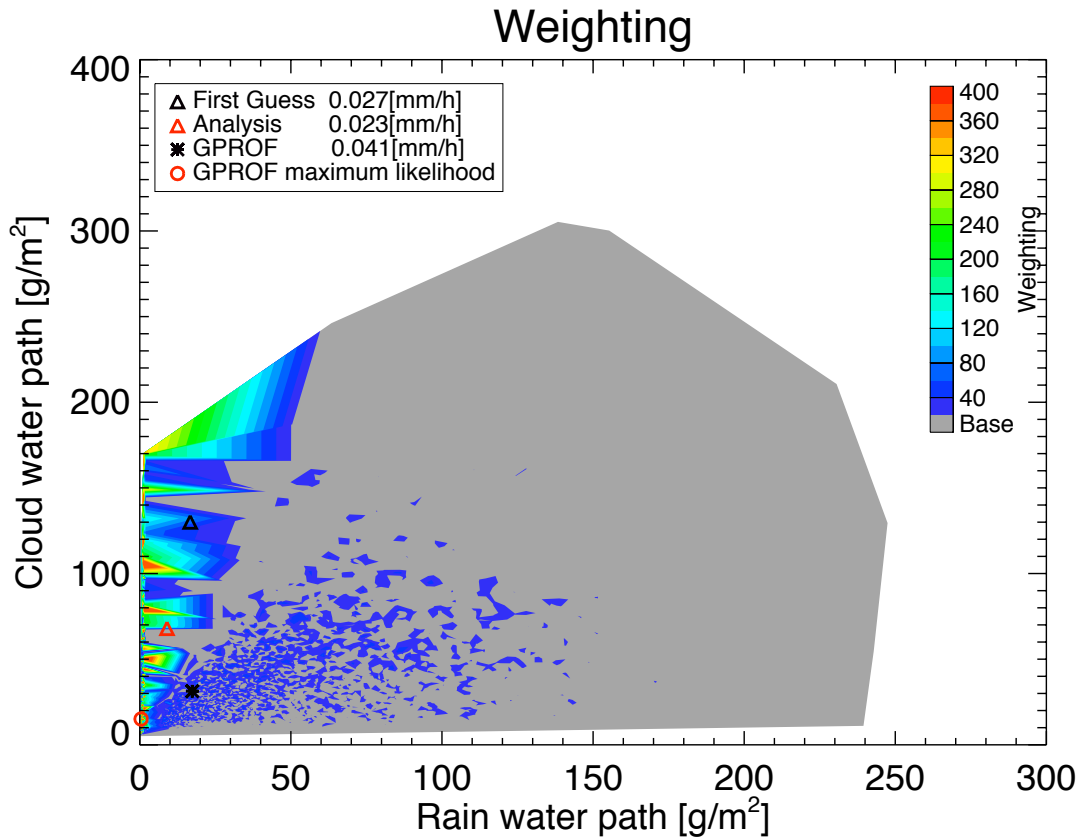


Figure 3.3 The GPROF retrieval weighting contour as a function of CWP and RWP, overlaid by the 1D-Var FG water paths (black triangle), 1D-Var analysis water paths (red triangle), GPROF weighted/retrieved water paths (asterisk) and GPROF maximum weighted water paths (red circle) for pixel 1. The rain rate for each retrieval is shown in the upper left box.

possible) to evaluate the 1D-Var retrieved microphysics. CWP and RWP values for the GPROF retrieval, GPROF maximum likelihood, 1D-Var FG, and 1D-Var analysis are all shown in the figure. Corresponding rain rates are 0.041 mm h^{-1} for GPROF retrieval, 0.027 mm h^{-1} for FG, and 0.023 mm h^{-1} for analysis. This pixel represents a light rainfall case.

The goal of the 1D-Var retrieval is to adjust the temperature and moisture (and cloud and precipitation) profiles to minimize the difference between the simulated and observed T_b vectors under the constraints of the background field and the background error covariance matrix, as shown in Eq. (3.3). Table 3.1 shows the comparison of T_b departures from the observation of the GPROF maximum likelihood, 1D-Var FG and analysis, and also the ECMWF bias correction for the purpose of assimilation. For ECMWF, the departures are bias-corrected.

Table 3.1 Bias corrected T_b departures at channel 19V, 19H, and 22V for GPROF maximum likelihood entry, ECMWF 1D-Var FG and ECMWF 1D-Var analysis solution.

T_b departures (K)	19V	19H	22V
GPROF maximum likelihood departures	-2.177	-0.471	-0.546
ECMWF 1D-Var FG departures	-1.662	-5.583	-1.739
ECMWF 1D-Var analysis departures	0.236	-2.104	0.204
ECMWF bias correction	-0.043	0.037	2.003

Table 3.1 shows that T_b s for all channels move closer to the observations in going from 1D-Var FG to analysis. This produces a comparable 3-channel departure RMS to that of the GPROF maximum likelihood. Figure 3.3 demonstrates that both the FG and analysis solutions are enclosed in the database envelope, meaning that both solutions are included in GPROF's possible solutions. FG T_b departure is defined as:

$$\text{FG departure} = \mathbf{y} - \mathbf{b} - \mathbf{H}(\mathbf{x}_b) \quad (3.5)$$

where \mathbf{b} is the bias correction. Analysis departure is defined similarly. Negative departures indicate that the FG may contain too much water. The correct microphysical adjustment should, therefore, decrease the emission. In the analysis, both CWP and RWP are decreased from FG and, therefore, T_b s are reduced and the analysis solution moves closer to the GPROF solution. This is consistent with the direction of the T_b adjustments in Table 3.1. In this case, both GPROF and 1D-Var reach similar results in terms of T_b as well as rain and cloud water.

3.3.2.2 PIXEL 2

Pixel 2 has the highest 19V T_b among all the selected pixels, indicating that this pixel has the strongest rain signal (see Figure 3.2). The retrieved rain rates for GPROF, 1D-Var FG and analysis are 6.527, 1.889, and 5.111 mm h⁻¹, respectively. Figure 3.4 demonstrates that the selected GPROF database for the observed T_b vector contains profiles with RWP ranging from 500 g m⁻² to 5000 g m⁻² and CWP ranging up to approximately 700 g m⁻². The closest T_b match from the GPROF database produces less than a 1 K bias from the observation for all channels, as shown in Table 3.2. From Table 3.2, it can also be seen that the 1D-Var FG has overwhelmingly large T_b departures from the observation. This means that the FG profile does not match observations particularly well. The prominent positive T_b biases in the FG indicate that the modeled liquid water must be increased in the analysis. Figure 3.4 shows that the FG solution resides outside of the observation based envelope, which is considered to be all the possible observed solutions defined by the database. The FG has a CWP that is too large and a RWP that is too small. The small RWP corresponds to a smaller retrieved rain rate (1.889 mm h⁻¹)

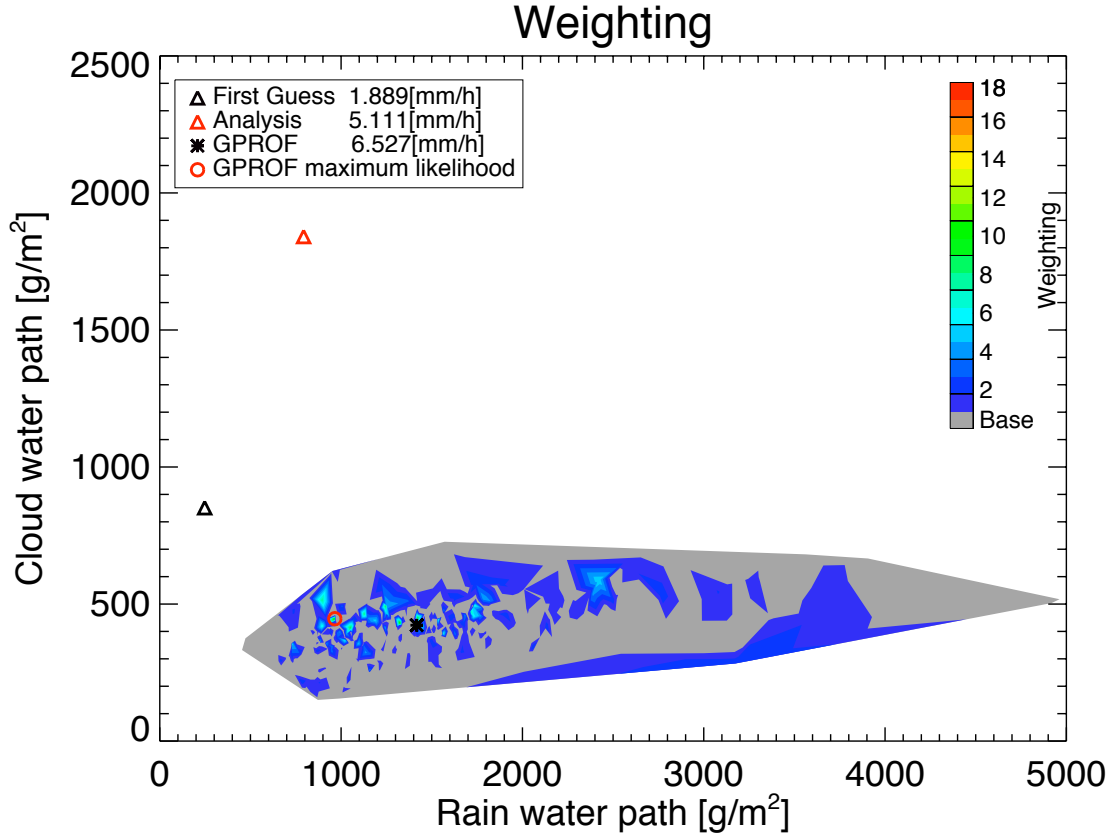


Figure 3.4 Same as in Figure 3.3 except for pixel 2.

Table 3.2 Same as in Table 3.1 except for pixel 2.

T_b departures (K)	19V	19H	22V
GPROF maximum likelihood departures	-0.041	0.912	0.843
ECMWF 1D-Var FG departures	30.448	57.784	9.600
ECMWF 1D-Var analysis departures	9.190	19.011	2.200
ECMWF bias correction	-9.030	-17.146	-1.701

compared to the GPROF retrieval (6.527 mm h⁻¹). To produce realistic cloud ranges defined by the database, the CWP needs to be reduced and RWP needs to be increased. After the 1D-Var retrieval, the bias-corrected T_b departures are greatly reduced from 30.448 K, 57.784 K, and 9.600 K to 9.190 K, 19.011 K, and 2.200 K, respectively, for

channels 19V, 19H, and 22V, and the retrieval has also managed to adjust the microphysics to produce a better T_b match to the observation although the departures remain larger than those from GPROF. However, Figure 3.4 shows that besides adding in some rainwater, the analysis cloud liquid water is moving away from the GPROF. Figure 3.5 displays the profile distributions of cloud, rain, and ice for GPROF retrieval, 1D-Var FG, and analysis. Evidently, GPROF produces more rain than cloud and 1D-Var produces more cloud than rain at each level.

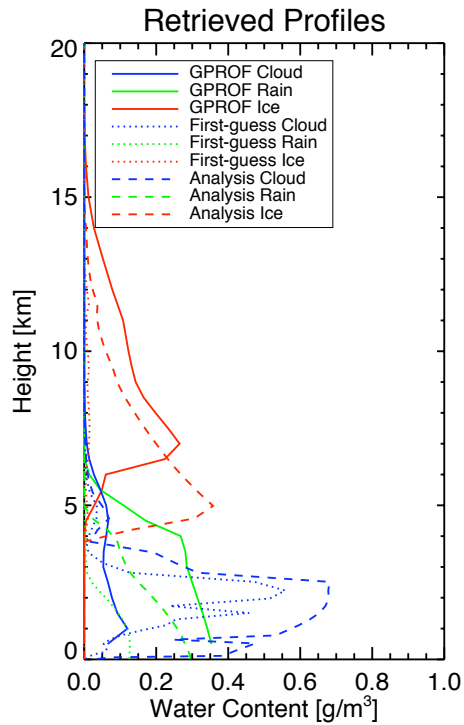


Figure 3.5 Profiles of cloud, rain, and ice for GPROF retrieval, 1D-Var FG, and 1D-Var analysis for pixel 2.

The CWP and RWP are 1840 g m^{-2} and 790 g m^{-2} , respectively, for the analysis, and 440 g m^{-2} and 970 g m^{-2} for the GPROF maximum likelihood entry. Although the Total Water Path (TWP) for the analysis (2630 g m^{-2}) is much larger than the TWP for the GPROF maximum likelihood entry (1410 g m^{-2}), they produce similar emission

signals, as seen from the analysis T_b biases with bias corrections, shown in Table 3.2. This is because the absorption/emission efficiency for clouds in the Rayleigh regime is much smaller than that of the rain in the Mie regime as rain droplets have much larger size parameters at the same microwave frequency.

To demonstrate the efficiency difference, a T_b sensitivity calculation is performed using a 1D raining column over ocean, which is shown in Figure 3.6a. In the sensitivity test, TPW is kept constant, and rainwater is converted to cloud water. The rain ratio increment as the x -axis is defined as the percentage of rainwater content that is converted to cloud water with -100% representing the all-cloud-scenario. As rain is converted to cloud along the negative direction of the increment ratio, T_b s at all three channels decrease, as shown in Figure 3.6b.

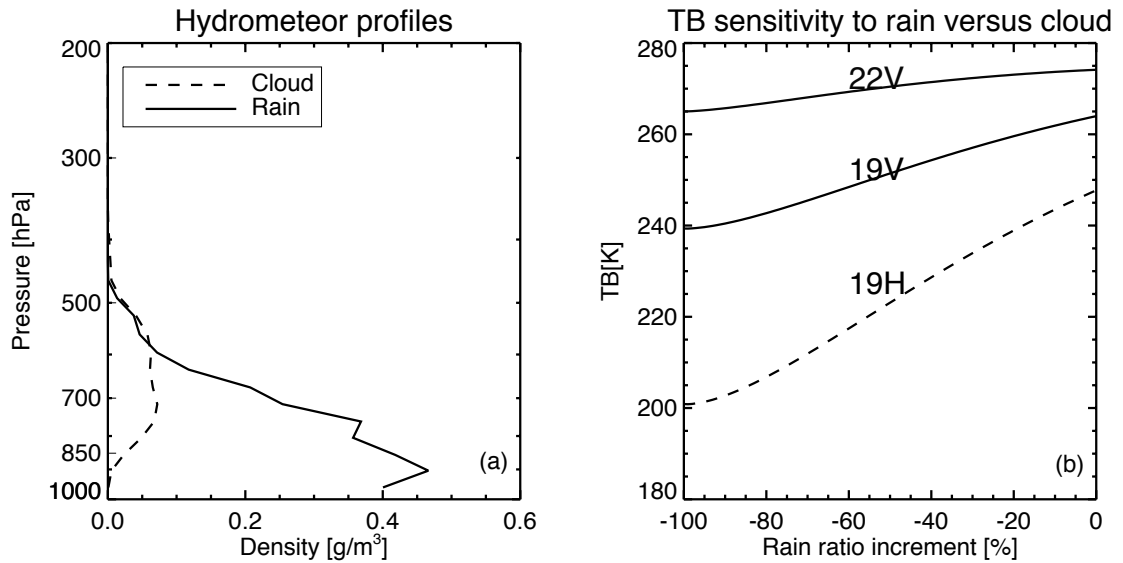


Figure 3.6 (a) The cloud and rain profiles for the T_b sensitivity test. (b) T_b sensitivity test of the emission signal to the cloud and rain ratios keeping constant liquid water content.

The two retrievals for pixel 2 differ primarily in the CWP/RWP ratios. This can also be attributed to the under-constrained nature of the retrieval problem and their non-unique solutions. Even though the analysis rain rate of 5.111 mm h^{-1} gets closer to the GPROF retrieval, and the T_b departures are greatly reduced, the cloud/rain ratio is significantly different from what was ever observed by PR/TMI. In 1D-Var, the microphysics are generated by the linearized moist physics scheme run at a single point and a single time step, with thermodynamic profiles as inputs. Although producing a similar rain rate, the difference in the CWP/RWP points to issues in other aspects, especially with the linearized moist physics scheme that deserves further investigation and improvement. In this case, GPROF and 1D-Var analysis have large differences, but it may be argued that the analysis did not quite converge on the observed T_b . As such, these differences may not be very meaningful.

3.3.2.3 PIXEL 3

For pixel 3, the rain rates are 0.364 , 4.477 , and 1.244 mm h^{-1} , respectively, for GPROF, 1D-Var FG, and analysis. The analysis rain rate is reduced from FG and moves closer to the GPROF retrieval. The FG has large negative T_b biases for all channels, as seen in Table 3.3, indicating too much emission from liquid compared to the observation. Figure 3.7 shows that the FG CWP and RWP are approximately 2300 and 900 g m^{-2} and significantly outside GPROF's envelope range of 300 and 600 g m^{-2} .

Table 3.3 Same as in Table 3.1 except for pixel 3.

T_b departures (K)	19V	19H	22V
GPROF maximum likelihood departures	-0.191	-1.105	-0.222
ECMWF 1D-Var FG departures	-13.212	-23.246	-4.788
ECMWF 1D-Var analysis departures	-0.684	0.603	-1.809
ECMWF bias correction	-22.403	-41.388	-6.961

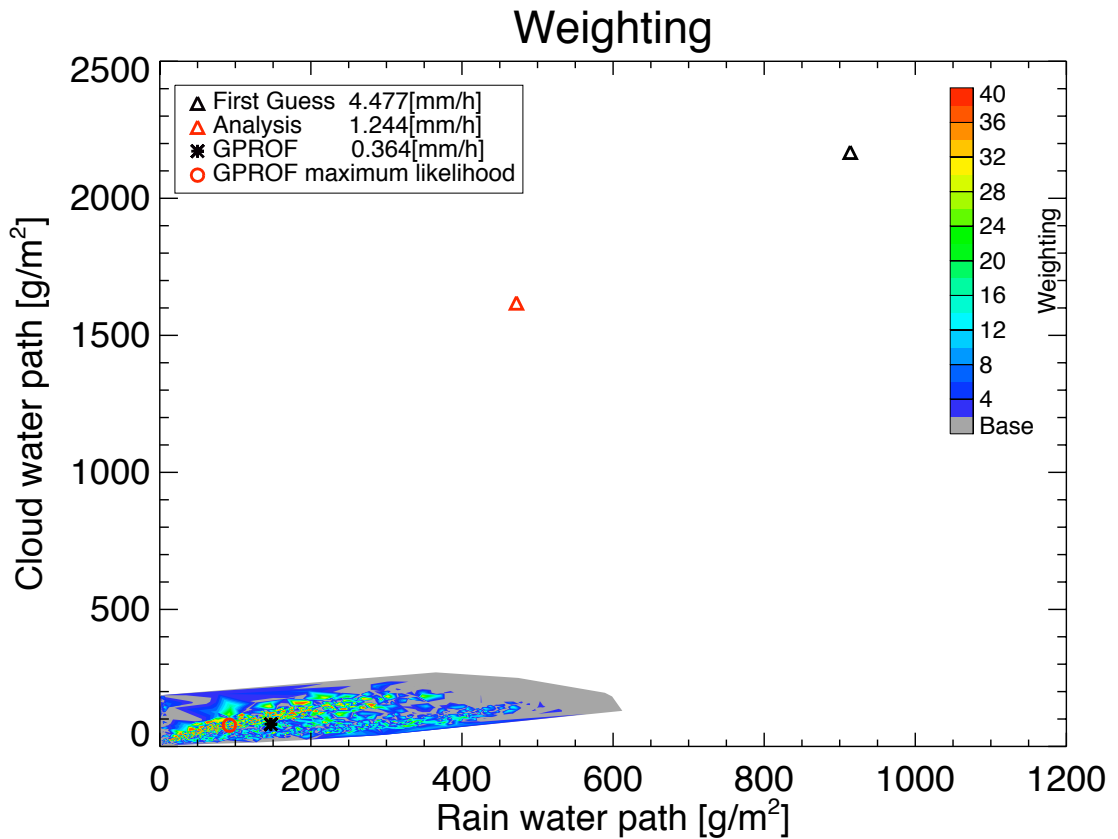


Figure 3.7 Same as in Figure 3.3 except for pixel 3.

After the 1D-Var, the analysis reduces the T_b departures to substantially lower values by reducing both cloud and rainwater. The analysis RWP is brought into the database range while the analysis CWP is still several times larger than the maximum value of GPROF's envelope. In other words, although the minimization process is

successful in matching the T_b vectors, the CWP/RWP ratio is highly biased with an extremely large CWP value (1620 g m^{-2}). As the minimization process is trying to produce a simulated T_b vector that is close to the bias-corrected observed T_b vector instead of the real T_b , large bias corrections may cause 1D-Var to produce biased microphysics with respect to the observed one. Also, the analysis IWP of 180 g m^{-2} is larger than the GPROF IWP of 60 g m^{-2} , which will increase the scattering slightly and, therefore, reduce the T_b s in the analysis. In this case, both GPROF and 1D-Var reach similar results to T_b , while at the same time having very different cloud and rainwater solutions.

3.4 Statistical Analysis

Differences between the GPROF and 1D-Var retrievals can be categorized into four scenarios. 1) T_b s match within given uncertainty ranges and the cloud water/rainwater paths are in general agreement defined as the analysis being within the observational envelope (e.g., pixel 1). This category includes the cases in which the 1D-Var retrieval produces CWP/RWP ratios that are observationally possible. 2) T_b s match but the CWP/RWP ratios do not (e.g., pixel 3). This category includes the cases in which the 1D-Var retrieval successfully matches the observation but allocates microphysical properties that are not observed in the PR/TMI database. 3) T_b s do not match and microphysics do not match either (e.g., pixel 2). This category includes the cases in which the liquid species of rain and clouds match but the rest such as ice species do not, which contribute to the unmatched T_b s. 4) T_b s do not match while the investigated microphysics properties do match (examples of this were not presented in the examined scene). Among these, category 2 is of special interest because in this category, the

optimal estimation procedure successfully minimizes the cost function yet the cloud does not converge to a solution that is similar or even allowed in the GPROF algorithm; in other words, the retrieval results are biased even when the retrieval is successful. Now two compelling questions become: How often does this condition occur? And, what are the microphysical biases in this category? The statistical analysis in this section strives to answer these questions.

3.4.1 Data

ECMWF Cycle 35r1 was operational from 30 September 2008 to 10 March 2009. One month of 1D+4D-Var data from October 2008 were extracted from the operational ECMWF analysis to perform further statistical analysis. Cloudy and rainy observations were assimilated into 4D-Var system and only 1D-Var retrievals that converge and pass the ‘excess snow’ check from SSM/I on DMSP F-13 are analyzed. For each pixel, the data includes stratiform surface precipitation flux, convective precipitation flux, total column water vapor, water paths of rain, snow, cloud and ice, SSMI observed T_b vector, simulated T_b vector, and bias corrections for both the FG and analysis. The data represent a later version of the assimilation used in the case studies.

3.4.2 Categorization

The GPROF Bayesian retrieval is performed over each 1D-Var pixel utilizing the analyzed 1D-Var TPW and SST to ensure consistency between model and retrieval. This process is equivalent to assigning weights to qualified entries within the given SST and TPW ranges from the observationally constrained *a-priori* database. To avoid using entries in the higher latitude out of the TMI-orbit range that have colder SSTs, the comparisons are constrained to 40°S and 40°N. Comparisons between GPROF and 1D-

Var retrievals are classified into four categories based on the T_b and microphysical agreement.

GPROF retrievals use estimated uncertainties in each of the channels; 1.45 K, 1.87 K, and 1.46 K at 19V, 19H, and 21V, respectively, to assign weights to individual profiles (Elsaesser and Kummerow 2008). The same values are used to determine if the 1D-Var method has converged as well. If the 1D-Var values differ by more than the stated T_b , the pixel is deemed not to have converged for the analysis.

The microphysical properties to be examined in this study include the RWP and CWP. To determine whether the 1D-Var retrieved RWP and CWP are within the database envelope that was described in Section 3.3 for each pixel, a procedure is defined as follows and an example is shown in Figure 3.8. First, if the 1D-Var RWP is outside of the GPROF envelope, the microphysics are considered unmatched. Otherwise, the 1D-Var RWP's 20% uncertainty values are calculated, which is illustrated with dashed lines in Figure 3.8a. The database's CWP distribution within this RWP range is determined.

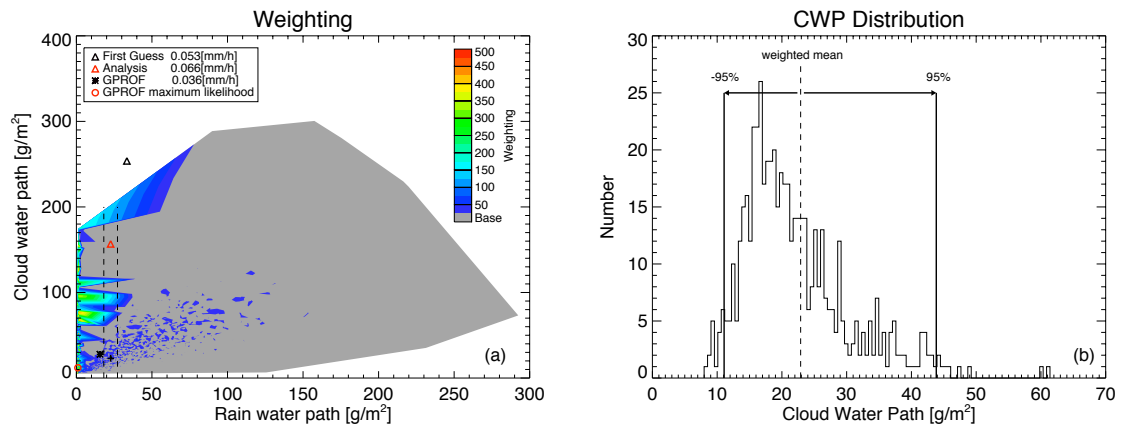


Figure 3.8 Illustration of the procedure to define the match of microphysics. (a) Same as in Figure 3.3 with the dash lines showing the 20% RWP variability range. (b) The CWP distribution within the 20% RWP range. The weighted mean CWP and 95% mark on both sides are drawn.

With reference to the distribution's weighted mean value (weighting is determined by Eq. (3.4) in Section 3.3), the distribution's 95% ranges (95% is equivalent to the 2σ range in the Gaussian distribution) on both sides are calculated and illustrated in Figure 3.8b. If the 1D-Var CWP falls outside of the 95% range, the microphysics is considered to be unmatched. Otherwise, when both the 1D-Var analysis CWP and RWP fall within the allowed ranges, the microphysics is considered to be matched, implying that the 1D-Var retrieved microphysics falls within the range of values that GPROF deems possible.

Based on whether the T_b s and/or microphysics match, each pixel in the one-month period is assigned to one of the four categories defined in Section 3.2.3. The percentage of each category is 40.7%, 46.9%, 4.5%, and 7.9%, as shown in Table 3.4. It is worthwhile to note that category 2 takes up 46.9% of all of the retrievals. In this scenario, the variational method works successfully to minimize the cost function with respect to the T_b s, but does not converge to the 'observed' microphysical properties from the cloud schemes. The incorrect properties especially the rain structures, will inevitably impact the rain retrieval results.

Table 3.4 Percentage of each category in the database.

Percentage	T_b s match	T_b s don't match
RWP and CWP match	Category 1: 40.7%	Category 3: 4.5%
RWP and CWP don't match	Category 2: 46.9%	Category 4: 7.9%

3.4.3 Microphysics Biases in Category 2

This section explores the nature of the microphysical biases between GPROF and 1D-Var. It also tries to ascertain if these biases are consistent and universal or have a dependence on the regional meteorology.

3.4.3.1 GLOBAL MICROPHYSICS BIAS

The bias is first explored using the whole month's global data between 40°N and 40°S. The ratio of 1D-Var over GPROF retrieved CWP as a function of RWP is plotted in Figure 3.9. The prominent feature of Figure 3.9b is that a very large percentage of the category 2 entries in the database produce much larger CWP in the 1D-Var analysis than in GPROF for pixels with rain rates greater than 1 mm h⁻¹. Table 3.5 shows the

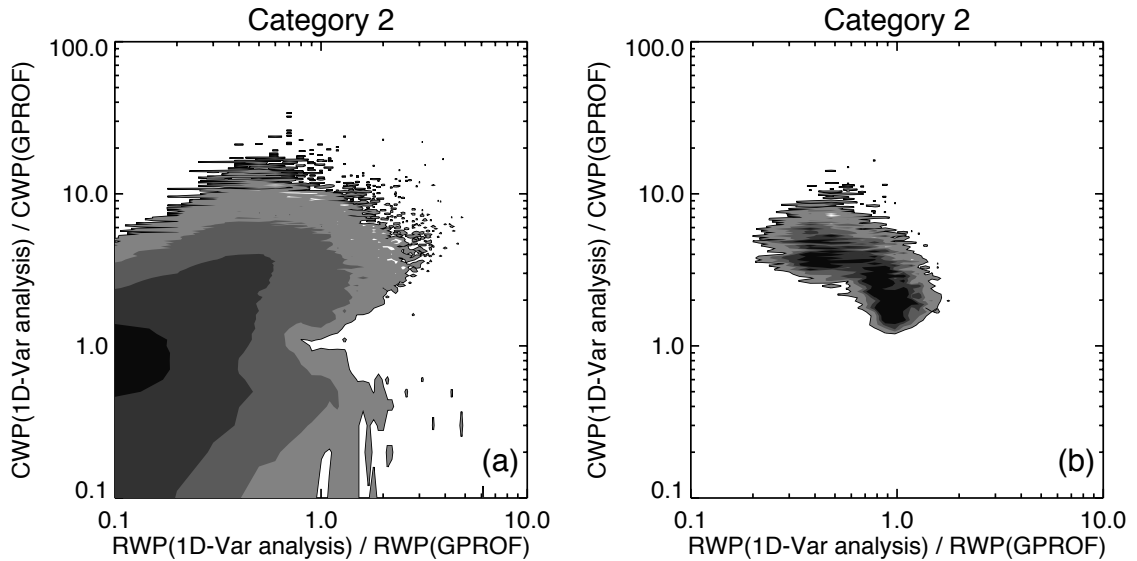


Figure 3.9 Normalized frequency contour of CWP ratio over RWP ratio for category 2 with (a) all rain rates and (b) rain rate ≥ 1 mm h⁻¹. The contour intervals for panel a are 1e-5, 1e-4, 1e-3, and 1e-2. The contour intervals for panel b are 0.0005, 0.001, 0.0015, and 0.002.

Table 3.5 Percentage of cases in category 2 with different CWP and RWP ratio ranges. Values in the parentheses are the percentages for GPROF surface rain rate $\geq 1 \text{ mm h}^{-1}$.

Percentage	CWP ratio < 0.5	$0.5 \leq \text{CWP ratio} \leq 2.0$	CWP ratio > 2.0
RWP ratio < 0.5	20.50% (0.01%)	41.96% (0.01%)	17.14% (18.17%)
$0.5 \leq \text{RWP ratio} \leq 2.0$	0.56% (0.12%)	2.87% (9.30%)	15.59% (71.35%)
RWP ratio > 2.0	0.06% (0.01%)	0.09% (0.01%)	1.24% (1.04%)

percentages of different CWP and RWP ratio ranges for category 2. It can be seen that only 2.87% of the retrievals can be considered comparable in both CWP and RWP; in 79.6% of the time, 1D-Var produces less than half of the GPROF-retrieved RWP (in 93.6% of the time, 1D-Var retrieval produces smaller RWP than GPROF retrieval.), and in 34.0% of the time, 1D-Var produces more than two times of GPROF-retrieved CWP. Removing the impact of drizzle cases that produce very large ratios, only cases whose GPROF-retrieved surface rain rate is greater than 1 mm h^{-1} are kept for analysis and the percentages are shown in the parentheses of Table 5. 90.6% of the time, 1D-Var retrieved CWP is at least two times that of the GPROF retrieval. It is clear that large discrepancies exist between the two retrieval algorithms in allocating the water content between different liquid hydrometeor species, i.e., cloud water and rainwater. The ratio is directly responsible for the unmatched microphysical properties in category 2. In GPROF retrievals, the rainwater estimate is driven by PR retrievals and the cloud water estimate is driven by CRM simulations but constrained by the PR and TMI observations. In the case of 1D-Var retrievals, both are the result of microphysical parameterizations that are used in the minimization and are linked by common hydrological processes in clouds and convection.

3.4.3.2 REGIONAL DIFFERENCES

Figure 3.10 shows the 1 by 1 degree binned monthly mean cloud/(cloud+rain) maps for GPROF, 1D-Var FG, and 1D-Var analysis. Both 1D-Var FG and 1D-Var analysis retrievals produce overwhelmingly larger cloud percentages compared with GPROF, which is consistent with Figure 3.9. 1D-Var quality control and linearization do not account for the large discrepancies. The little difference between Figure 3.10b and 3.10c indicates that the cloud/rain ratio is not being changed by the observations in the 1D-Var but instead is completely controlled by the moist physics. However, the two algorithms produce similar spatial patterns although with different magnitude (note that the scales are different). To explore the regional dependence, four representative regions associated with different meteorological regimes are selected based on the difference in cloud water/rainwater ratios. The four specific regions are:

Regime 1: [10°S, 30°S] and [100°W, 70°W]. This is the SE Pacific regime, which is identified as the region with relatively low SST, low total precipitable water, and frequent stratocumulus and trade cumulus occurrence. The abundance of clouds with relatively low rain efficiency associated with the subsidence of air in the high pressure system in these clouds cause high cloud/rain ratios.

Regime 2: [0°N, 10°N] and [120°E, 180°E]. This is the West Pacific regime associated with higher SSTs in the warm pool and high relative humidity that provide a favorable environment for tropical convections.

Regime 3: [0°N, 15°N] and [140°W, 100°W]. This is the East Pacific regime. Regime 3 has relatively lower cloud/rain ratio compared to regime 2. Berg et al. (2002) investigated the differences of the storm systems between the East and West Pacific and

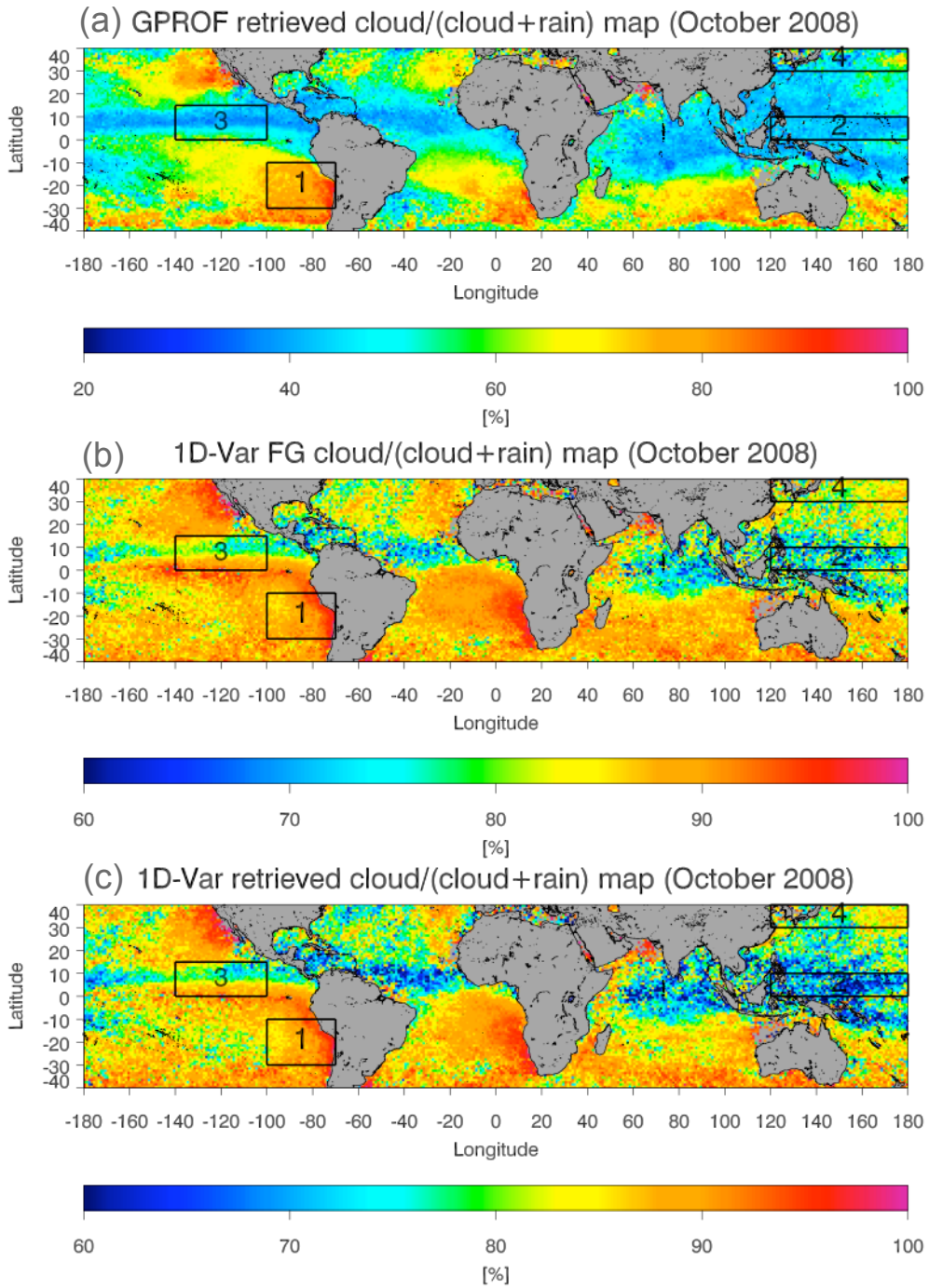


Figure 3.10 (a) GPROF retrieved cloud/(cloud+rain) map for October 2008. (b) 1D-Var FG and (c) 1D-Var analysis cloud/(cloud+rain) map for the same month. The four selected regimes are enclosed in boxes.

found that the storms over the East Pacific have shallower clouds with warmer cloud tops, larger proportion of stratiform rain, less ice for similar amounts of rainwater, and lower melting layers.

Regime 4: [30°N, 40°N] and [120°E, 180°E]. This is the Northern Hemisphere storm track regime. This regime is generally associated with mid-level convection within the mid-latitude frontal storms. This regime may also be influenced by the increased aerosol concentration that will increase the ratio of cloud water to rainwater (Berg et al. 2008).

CWP/RWP ratios that are not observed in the GPROF database differ systematically across the four regimes. Percentage of category 2 is 41.4% in the SE Pacific regime, 58.2% in the West Pacific regime, 73.1% in the East Pacific regime, and 46.0% in the storm track regime.

The frequency contours of CWP versus RWP for category 2 in each regime of both GPROF and 1D-Var are shown in Figure 3.11. Regime 1 is characterized by small RWP and little correlation between CWP and RWP. This is consistent with the relatively small rain rates in the stratocumulus and trade cumulus within this regime. For GPROF, the relationships of CWP versus RWP are similar for regimes 2, 3, and 4 at a RWP range of up to 100 g m^{-2} . At higher RWP values, the amount of CWP needed per amount of RWP is highest at regime 2 and lowest at regime 4. This is found to be associated with the stratiform portion within each regime. In stratiform rain, GPROF consistently retrieves very little cloud water. The relative larger portion of stratiform clouds in regime 3 compared to regime 2 is consistent with Berg et al. (2002). On the other hand, the 1D-Var retrieved CWP is much larger than the GPROF retrieved CWP for the same amount of RWP for all regimes. A ‘convective fraction’ parameter, defined for 1D-Var as the

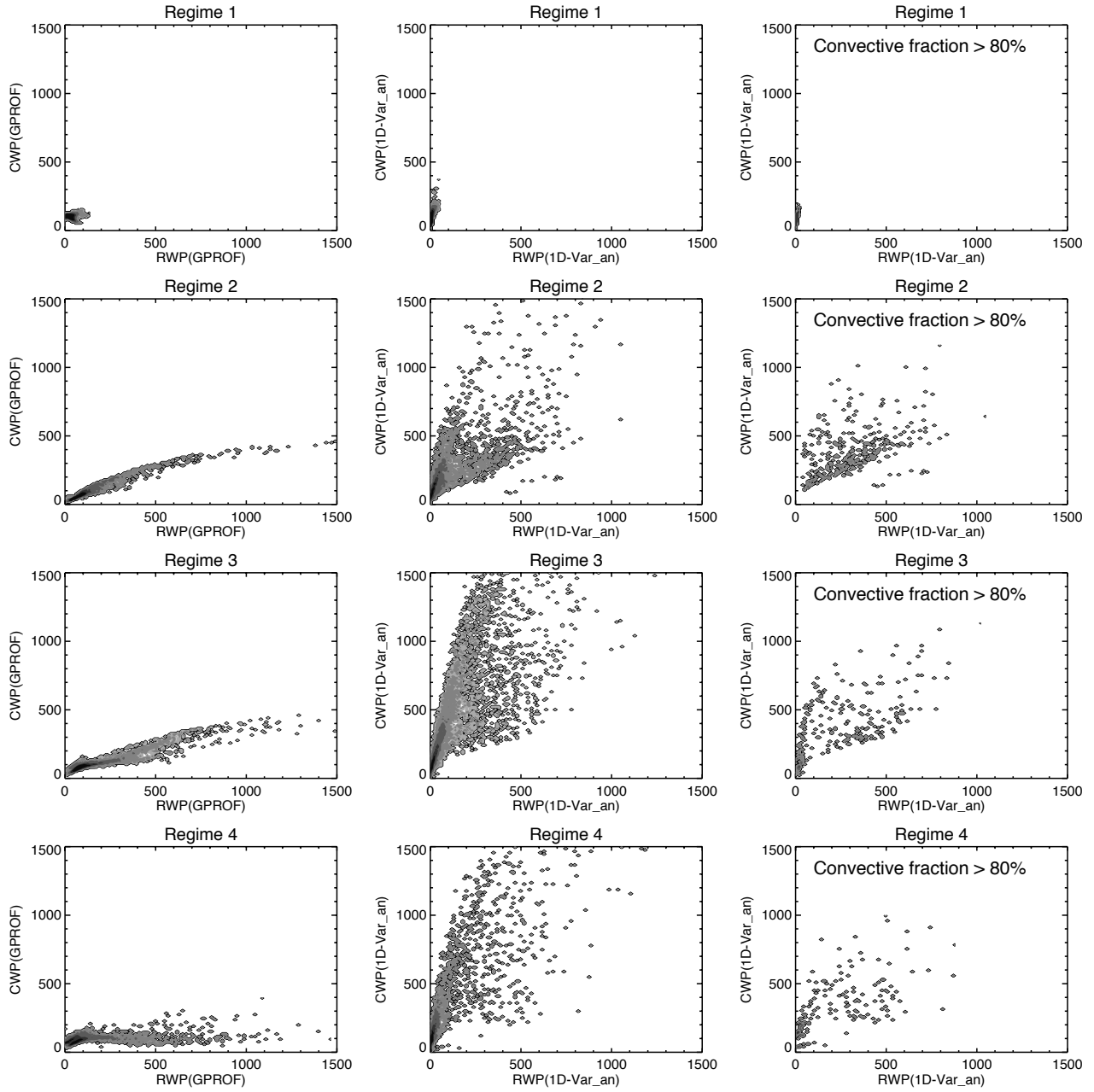


Figure 3.11 Normalized frequency contour of CWP over RWP in category 2 for all four regimes in GPROF (left panels), 1D-Var (middle panels), and convective 1D-Var pixels (right panels).

ratio of convective rain to total rain produced by the cumulus parameterization and the large-scale condensation scheme. It appears that in 1D-Var, the CWP/RWP ratio is related to the convective fraction with smaller convective fractions producing larger CWP for the same amount of RWP. This indicates that larger CWP in 1D-Var is produced by the stratiform rain in the large scale parameterization.

If the cases with larger convective fractions (>80%) are selected out, their ratios fall closer to those of GPROF, as shown in the right columns of Figure 3.11. It is worthwhile to note here that the definition of ‘stratiform’ is not equivalent in GPROF and 1D-Var. Regardless the detailed differences, all regimes contain a consistently different distribution of cloud water and rainwater in the 1D-Var algorithm when compared to GPROF.

3.4.3.3 DISCUSSION

The previous section shows that GPROF and the 1D-Var solutions tended to differ quite dramatically in their CWP, and to a lesser extent, in their RWP, despite matching the observed T_b . This is further examined below.

For each pixel, the Total Water Path (TWP) distribution of the possible solutions in the GPROF database is calculated. Similar to Section 3.4.2, the boundary values of 95% range on each side of the weighted mean TWP is determined. If the 1D-Var analyzed TWP falls within this range, it is 95% probable that the analysis TWP is within the GPROF observed TWP solutions. For the global dataset, it is found that in category 2, although the cloud and rain microphysics do not match, 83.8% of the 1D-Var analysis pixels fall within the 95% ranges of GPROF solutions. Specifically, the TWP match ratio takes 93.1%, 90.9%, 96.7%, and 80.8%, respectively, for the four selected regimes above.

The smaller percentage in regime 4 compared with the other three regimes could potentially be caused by a larger portion of ice hydrometeors in the included storms. This is consistent with the expectation, and together with the larger amount of cloud liquid water, it is clear that although 1D-Var finds comparable TWP in order to match the T_{bs} , it allocates different amounts of cloud and rainwater relative to the GPROF solution.

3.5 Impact of Higher Frequencies on Constraining the Cloud/rain Ratio

As previously mentioned, only three channels (e.g., 19V, 19H, and 22V) are used in the 1D-Var algorithm. At these lower microwave frequencies, cloud droplets belong to the Rayleigh scattering regime in which absorption/emission dominates and scattering is only a minor effect. Raindrops begin to fall in the Mie regime – particularly for larger rainfall rates. With higher frequencies such as 37 and 85 GHz, cloud droplets still belong to the Rayleigh scattering regime, but the absorption and scattering process increased more rapidly in the Mie regime due to increased size parameters. It is, therefore, possible to differentiate these two hydrometeor species with information from these higher frequency channels.

Forward model uncertainties also increase somewhat at higher frequencies. Elsaesser and Kummerow (2008) used values of 1.45, 1.87, 1.46, 1.50, 2.38, 2.15, and 3.54 K for 19V, 19H, 22V, 37V, 37H, 85V, and 85H, respectively, as was introduced in Section 3.4.2. To perform the sensitivity of using higher frequency channels on the cloud/ratio change, three channel combination schemes are evaluated. The 3-channel case uses 19V, 19H, and 22V; the 5-channel case uses 19V, 19H, 22V, 37V, and 37H; and the 7-channel case uses 19V, 19H, 22V, 37V, 37H, 85V, and 85H. Several raining cases are examined below. For each case, rainwater and cloud water are converted between each

other by redistributing the water content at each level while holding TWP constant. A ratio increment is defined with negative values to indicate that rainwater was redistributed to the cloud water category while positive values convert cloud water to rainwater. For instance, -60% means that 60% of the rainwater at each layer is removed and redistributed as cloud. If the changes are less than the T_b uncertainty values for all the channels used, the microphysical change is considered too small to be detected by these channels. Otherwise, if the T_b change goes beyond the uncertainty value for any channel, the microphysics change is detectable. Several representative profiles that produce surface rain rates of 0.05, 0.52, 1.00, 5.09, 10.06, and 21.15 mm h⁻¹ are used to explore the impact of adding high frequency channels, shown in Figure 3.12, and the results are summarized in Table 3.6.

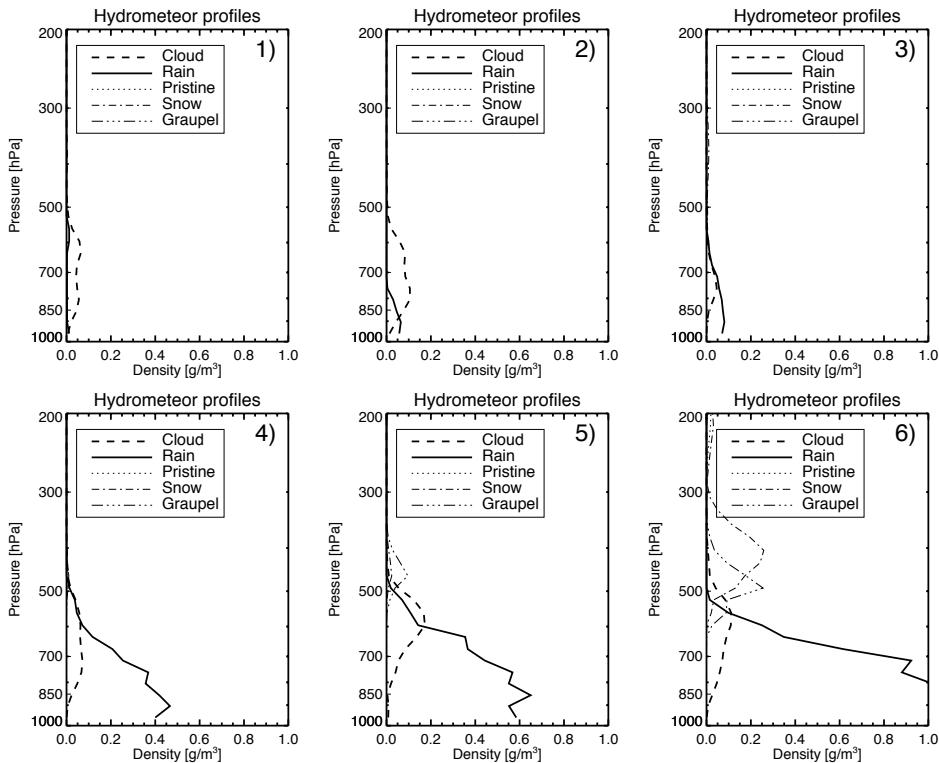


Figure 3.12 Six representative hydrometeor profiles for the case studies.

Table 3.6 Sensitivity test results for all cases.

Case	Rain rate (mm h ⁻¹)	Channel Combination	Rain to cloud Detection threshold (channel)	Cloud to rain Detection threshold (channel)
1	0.05	3 channel	None (---)	+41% (19H)
		5 channel	None (---)	+17% (37H)
		7 channel	None (---)	+17% (37H)
2	0.52	3 channel	-59% (19H)	+12% (19H)
		5 channel	-24% (37H)	+ 7% (37H)
		7 channel	-24% (37H)	+ 7% (37H)
3	1.00	3 channel	-26% (19H)	+21% (19H)
		5 channel	-14% (37H)	+12% (37H)
		7 channel	-14% (37H)	+12% (37H)
4	5.09	3 channel	- 4% (19H)	+36% (19H)
		5 channel	- 4% (19H)	+36% (19H)
		7 channel	- 4% (19H)	+25% (85V)
5	10.06	3 channel	- 7% (19H)	+85% (22V)
		5 channel	- 7% (19H)	+29% (37V)
		7 channel	- 7% (19H)	+19% (85V)
6	21.15	3 channel	-36% (19H)	None (---)
		5 channel	- 4% (37V)	+44% (37V)
		7 channel	- 2% (85V)	+30% (85V)

3.5.1 Case 1

Case 1 rains at only 0.05 mm h⁻¹ with a CWP of 210 g m⁻² and a RWP of 20 g m⁻². As a result, even when all the rainwater is converted to cloud water, the T_b changes are still within the uncertainty ranges for all the seven channels. However, when cloud water is converted to rainwater, T_{bs} increase for 19, 22, and 37 GHz due to the increased emission efficiency from cloud to rain, as previously discussed in Section 3.3.2.2. T_{bs} decrease for 85 GHz due to increased Mie scattering caused by rain drops as well as decreased emission from elevated weighting functions that are associated with lower temperatures.

Considering differences between the cloud and rain profiles, the positive and negative ratio increment regimes are discussed separately. Qualitatively, converting

rainwater to cloud water cannot be detected because of the small amount of rainwater for this case even if all the seven channels are used. When cloud water is converted to rainwater, a sensitivity of +41% ratio increment is found for three channel combinations with channel 19H first detecting the difference. When 37 GHz is used, the detectable ratio increment moves up to +17% at channel 37H but when 85 GHz is added, the sensitivity remains at 17%. In this very light rain case, adding 37 GHz is beneficial to separate cloud from rain for the retrieval because the emission/absorption efficiency of water increases with microwave frequency. However, further adding 85 GHz is not useful in this respect because the T_b uncertainty range of 85 GHz masks the signal.

3.5.2 Case 2

Profiles and sensitivity results for case 2 are displayed in Figure 3.12(2) and Table 3.6. This profile includes 330 g m^{-2} of CWP and 70 g m^{-2} of RWP. By moving from three channels to five channels and then to seven channels, the detectable ratio increment of converting rainwater to cloud water moves from -59% (the detection channel is at 19H, shortened as 'at 19H' hereafter) to -24% (at 37H) to -24% (at 37H), and the detectable ratio increment of converting cloud water to rainwater improves from +12% (at 19H) to +7% (at 37H) to +7% (at 37H). For this drizzle case (0.52 mm h^{-1}), adding 37 GHz improves the sensitivity significantly while adding 85 GHz does not further improve the result. The increased sensitivity at 85 GHz is once again masked by the greater uncertainty in these channels. Scattering is still relatively unimportant for this profile.

3.5.3 Case 3

The rain rate increases to 1 mm h^{-1} in this case, which contains more rainwater with less cloud water compared to case 2 as seen from Figure 3.12(2) and 3.12(3). The

detectable ratio increment of converting rainwater to cloud water moves from -26% (at 19H) to -14% (at 37H) to -14% (at 37H), and converting cloud water to rainwater improves from +21% (at 19H) to +12% (at 37H) to +12% (at 37H). As the rain rate is still relatively small, the results match case 2.

3.5.4 Case 4

Case 4 rains at 5.09 mm h^{-1} . With the increased rain content, the detection sensitivity of converting rain to cloud further increases from previous cases. The detectable ratio increment is held constant at -4% for all channel combinations because 19H sets the strongest constraint. When rain is converted to cloud, channels 19H, 19V, and 22V decrease monotonically due to the decreased emission efficiency of the clouds, while the sensitivity to channels 37H, 37V, 85H, and 85V increases at first due to decreased scattering from rain drops and then it decreases. When cloud water is converted to rainwater, the detectable ratio increment moves from +36% (at 19H) to +36% (at 19H) to +25% (at 85V). In this scenario, 19V, 19H, and 22V increases with an increased emission signal from more rain, while 37H, 37V, 85H, and 85V decreases with an increased scattering signal from rain. For 37 GHz, increased scattering and increased emission cancel each other out in providing higher sensitivity. The 85-GHz channel is beneficial in constraining the cloud/rain ratio in this case.

3.5.5 Case 5

Snow and graupel particles start to appear in this case, as seen in Figure 3.12(5). The existence of these ice particles masks some of the sensitivity to cloud and rainwater changes. The sensitivity mark is held constant at -7% because 19H again sets the strongest constraint for all channel combinations when rain is converted to cloud. In the

other direction, the detectable ratio increment moves from +85% (at 22V) to +29% (at 37V) to +19% (at 85V). In this large rain case (10.06 mm h^{-1}), both 37 and 85 GHz bring more sensitivity for differentiating cloud and rain.

3.5.6 Case 6

In this intense raining case (21.15 mm h^{-1}) that contains large amounts of snow and graupel lying above the liquid layer, the sensitivity moves from -36% (at 19H) to -4% (at 37V) to -2% (at 85V), and from no signal to +44% (at 37V) to +30% (at 85V). When rain is converted to cloud, T_{bs} at all frequencies increase in the beginning due to decreased scattering followed by a decrease due to decreased emission from cloud. The sensitivity to the cloud/rain ratio is enhanced by adding in 37 GHz and further enhanced by the incorporation of 85 GHz. It is worthwhile to note that these tests are based on theoretical sensitivity studies in which the ice contents are fixed. In reality, 85 GHz is more sensitive to ice instead of the cloud/rain ratios. It is, therefore, difficult to detect these ratios without prior knowledge of the ice.

From the case studies above, it is found that higher frequency channels are able to constrain the cloud/rain ratio with increased sensitivity. However, 37 GHz is sufficient for drizzle cases (rain rate $\leq 1 \text{ mm h}^{-1}$) and 85 GHz is beneficial for large rain rate cases (rain rate $\geq 5 \text{ mm h}^{-1}$) due to the increased scattering signal from raindrops. It is, therefore, helpful to include the higher frequency channels into the retrieval to improve the cloud and rain differentiation.

CHAPTER 4

A CLUSTERING APPROACH TO COMPARE CLOUD MODEL SIMULATIONS TO SATELLITE OBSERVATIONS

4.1 Introduction

Precipitation over land is important in a vast range of applications. Despite its importance, global rain gauge networks remain sparse, while the low penetrating capabilities of operational infrared and visible sensors (Kidder and Vonder Haar 1995) make those measurements reliable only in a statistical sense. Over many parts of the world, passive microwave satellite sensors offer the best hope for quantitative rainfall estimates. Microwave radiation is able to penetrate clouds and interact directly with precipitation-sized hydrometeors. Large ice particles will cause noticeable T_b depressions over land at frequencies greater than 30 GHz. The relationships between ice scattering represented by indicators such as T_b depressions and surface rain rate form the basis for current rainfall retrieval algorithms over land (Spencer et al. 1983; Grody 1991; Ferraro and Marks 1995; Conner and Petty 1998; Grecu and Anagnostou 2001; McCollum and Ferraro 2003). However, these scattering algorithms implicitly accept a relationship between ice aloft and surface rainfall that is known to vary by storm as well as region (Kummerow et al. 1996; Kidd 1998). The variations in location, storm type, and

microphysical mechanisms will cause variations in the scattering/rainfall relationship of or even within the storm. These variations, therefore, need to be accounted for. Cloud Resolving Models (CRMs), through their explicit descriptions of cloud microphysical properties, offer a convenient tool to interpret remotely sensed data. In particular, they can offer important additional information when the remotely sensed data contains insufficient information to fully constrain a solution. In this context, CRMs can provide the dynamical connection between ice aloft and precipitation at the surface. A requirement, however, is that the CRM properly represents the ice microphysics of the scene in question.

CRMs employing the non-hydrostatic governing equations may be used to simulate cloud-scale circulations and individual cloud element's microphysical processes at grid spacing of less than a few kilometers. Despite significant advances in cloud physics, many issues still exist in microphysical cloud modeling (Khain et al. 2000), especially in CRM bulk microphysical parameterizations, in which all microphysical processes are described in terms of integral parameters such as mass contents and/or number concentrations of a few types of cloud and precipitation particles. These parameterizations are known to be imperfect and have limitations. Particularly, cloud models tend to produce excessive high-density ice particles (Bauer 2001a; Biggerstaff et al. 2006; McFarquhar et al. 2006), and the excessive ice in many simulations was found to be problematic even for oceanic rainfall retrievals that relied on CRM simulations as described by Smith et al. (1992), Mugnai et al. (1993), Kummerow et al. (1996), Panegrossi et al. (1998), and Biggerstaff et al. (2006). Kummerow et al. (2006) quantitatively evaluated the retrieval errors associated with the databases built from

CRMs in a Bayesian framework. It was stressed that the simulated T_b -rain rate relations are sensitive to the sophistication of the models' microphysical parameterizations, which could affect the simulated T_b manifold and thus cause sensitivity to the latent heating and hydrometeor profile retrievals (Smith et al. 1992; Panegrossi et al. 1998; Biggerstaff et al. 2006). There is no universally correct cloud microphysical scheme and different cloud types within a storm may possess different dynamical and microphysical properties such that they contain diverse ice and rainfall relationships. Therefore, it is informative and imperative to evaluate the simulated microphysical properties of each cloud type to examine whether the CRM simulation is appropriate for retrieving a given storm. To improve retrieval accuracy over land, the potential biases in the CRM microphysical properties need to be identified and corrected to build more realistic and representative databases of precipitating clouds. Panegrossi et al. (1998) emphasized that similar characteristics between the observation- and simulation-generated databases are desired to provide numerical stability in rainfall retrievals. If suitable, the scattering database built from the simulation is also expected to evolve along with the storm development so that more realistic and reliable microphysical scenes can be reproduced from the observations.

Qualitative discrepancies in storm properties such as location, morphology, intensity, and time evolution are evaluated in some observation and simulation comparison studies (Chaboureau et al. 2002). In this study, it is not expected that CRM simulations match the satellite observations in space and time, especially in a semi-ideal setting wherein these discrepancies may originate from model initialization, boundary conditions, and/or large-scale forcing. Furthermore, satellite sensors can easily detect the

location of the storms. The goal of this work is thus not to produce a perfect model simulation, but instead to quantitatively evaluate the microphysical properties of different cloud types to ensure realistic and unbiased microphysics in each cloud regime including the convective core and the stratiform regime. Therefore, in this study, the criteria of defining a good simulation is not based on storm location, morphology, or intensity, but on unbiased statistical microphysical properties for each cloud type.

In this chapter, cluster analysis of microwave T_b s is used to quantitatively define cloud regimes. A numerical simulation of a convective case over the Amazon is compared with contemporary satellite observations cluster by cluster to quantitatively understand the microphysics discrepancies. This helps clarify the direction of improvement for the cloud model. The satellite observation and CRM simulation of this convective storm are described in Section 4.2. Section 4.3 describes the cluster analysis while Section 4.4 provides the analysis of individual cloud clusters.

4.2 Satellite Observation and RAMS Simulation of a Convective Event over LBA Region

A tropical squall line event on 23 February 1999 was observed during the TRMM-Large scale Biosphere-Atmosphere experiment in the Amazon (TRMM-LBA) field campaign. This convective event occurred in the westerly regime wherein the convective characteristics are oceanic and monsoon like: weaker, less organized, more widespread, and propagating slowly from the west (Cifelli et al. 2002; Rickenbach et al. 2002). Widespread convection broke out due to daytime heating and gradually formed into lines parallel to the deep tropospheric wind shear. Scattered weak convective cells in the late morning around 1400 UTC (1000 LT) initiated the convection; the cells became

widespread and were loosely organized into SE-NW bands by early afternoon around 1700 UTC (1300 LT). The convection was only weakly organized with light environmental winds. A relatively long, thin convective line developed by 2000 UTC but did not persist for long. The convection died out and completely dissipated from the LBA domain by the evening at 0000 UTC on 24 February (Lang et al. 2007). The TRMM satellite took a snapshot of this squall line at 2100 UTC during its decaying stage.

4.2.1 TRMM Observations

The TRMM satellite (Kummerow et al. 1998) was launched in November 1997. It is the first mission dedicated to measure tropical and subtropical rainfall to help better understand rainfall and latent heating distributions. The orbit is inclined at 35° to maximize observations in the Tropics. Of primary interest to this study are TRMM's Microwave Imager (TMI), the Precipitation Radar (PR), and the Visible and Infrared Scanner (VIRS).

TMI is a descendent of the Special Sensor of Microwave/Imager (SSM/I) and it measures radiance at a viewing angle of approximately 53° over a swath width of 760 km for nine polarized channels at five frequencies: 10.65, 19.35, 21.3, 37.0, and 85.5 GHz. Hereafter, the channels will be referred to 10v, 10h, 19v, 19h, 21v, 37v, 37h, 85v, and 85h (v represents vertical polarization and h represents horizontal polarization) to identify the measurement frequency and polarization in a simple fashion. The spatial resolution ranges from 63 × 37 km at 10.65 GHz to 7 × 5 km at 85.5 GHz.

PR operates at 13.8 GHz and has a horizontal resolution of approximately 4.3 km, a vertical resolution of 250 m, and a swath width of 217 km. TRMM PR data product 2A25 (Iguchi et al. 2000) is used in this study to provide the retrieved surface rain rate,

liquid and ice water paths, and cloud type classification. VIRS senses upwelling radiation over a swath width of 720 km in five spectral regions ranging from visible to infrared with central wavelength residing at 0.63, 1.60, 3.75, 10.8, and 12 μm . Cloud top properties and cloud phase can be inferred from the measured T_b s at a horizontal resolution of 2.1 km at nadir.

TMI's 37 and 85 GHz are sensitive to precipitating-size ice particles due to Mie scattering of snow, graupel, and/or hail. T_b depressions at these frequencies can, therefore, be used to detect convection that is producing large ice particles. The two frequencies respond to somewhat different ice particle properties. To demonstrate the physical relationship between microwave T_b depressions and hydrometeors more intuitively, sensitivity experiments are performed using a set of hydrometeor profiles containing large graupel and hail concentration intended to represent deep convection situations over land, as shown in Figure 4.1.

The hydrometeor species consist of cloud water, rain, pristine ice, snow, graupel, and hail. The hail category also represents frozen raindrops. In the calculations, the densities for mixed particles (snow and graupel) are prescribed and held constant. To eliminate sensitivity from non-microphysical factors, the surface temperature is set to 294.3 K and surface emissivity to 1. The surface is assumed Lambertian. T_b sensitivities of four frequencies (19, 22, 37, and 85 GHz) to hydrometeors are shown in Table 4.1. Hereafter in this paper, lower frequencies refer to 19 and 22 GHz and higher frequencies refer to 37 and 85 GHz. Here, 10 GHz is not used because it depends heavily on the surface. T_b s calculated from hydrometeors shown in Figure 4.1 serve as the control run, and seven sensitivity experiments and results are described

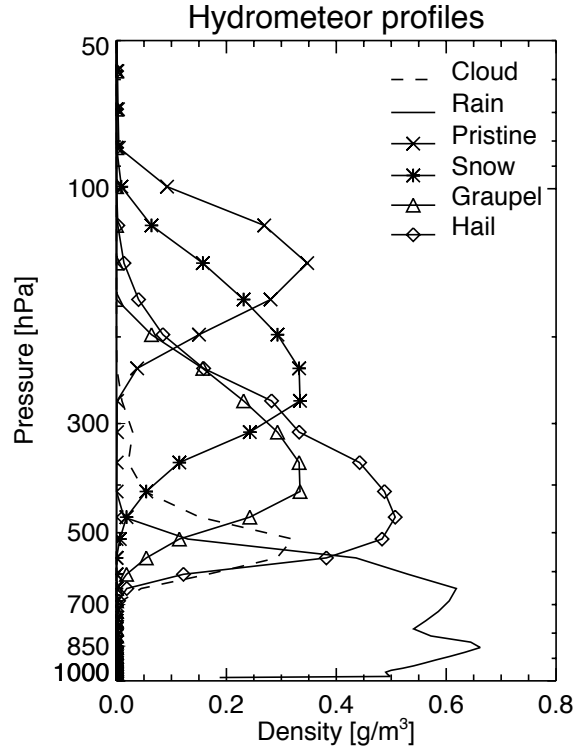


Figure 4.1 The representative hydrometeor profiles including cloud, rain, pristine, snow, graupel, and hail.

Table 4.1 Simulated T_b s at 19 to 85 GHz for the control simulation and six sensitivity tests.

	19 GHz	22 GHz	37 GHz	85 GHz
Control simulation	266.40	258.76	211.60	124.49
Test 1	268.47	261.73	221.03	135.88
Test 2	271.51	265.95	239.43	176.39
Test 3	263.32	256.59	223.85	147.94
Test 4	269.99	263.74	227.54	136.16
Test 5	254.63	243.30	173.66	97.19
Test 6	224.71	207.89	123.54	76.10

below. In test 1, high-density graupel particles are converted to low-density snow particles. All frequencies experience a T_b increase with higher frequencies gaining larger increases. In test 2, all hail is converted to snow. Results are the same as in test 1 except with larger magnitude. The particle density is a critical parameter that determines the heterogeneous particle's dielectric properties. The density of hail is larger than that of

graupel, which is larger than that of snow. Larger density ice particles have larger scattering efficiencies. Higher frequencies correspond to larger size parameters, which further raises the efficiency. As a consequence, higher-density particles produce stronger scattering signals at higher frequencies. Meirold-Mautner et al. (2007) explored the impact of snow density on simulated microwave T_b s and provided similar results. This will be examined in more detail in Section 4.3. In test 3, the supercooled water content is increased. Lower frequency experiences some decrease in T_b s due to lower emission temperature at elevated weighting function peaks, while higher frequency T_b s experience increases for this convective profile. The effect of supercooled cloud water at reducing the minima in T_b at high frequencies was identified by Adler et al. (1991) and was found to be associated with lowering of the single scattering albedo when liquid is mixed with ice particles. Biggerstaff et al. (2006) also reported an average warming of 15 K in T_b at 85 GHz over the convective region in one of their simulations. However, for non-convective profiles, cooling at higher frequencies may take place due to the lower emission temperature from the cold cloud together with the absence of the scattering energy from ice particles. In test 4, the hail particles are broken into much smaller sizes keeping the same water content. All frequencies undergo some increase due to decreased scattering. However, the increase for 37 GHz is larger than for 85 GHz again due to relative changes in the size parameters. The decrease in the particle size causes larger reduction in the volume scattering extinction at 37 GHz, which will also be further explored in Section 4.3. In test 5, the hail concentration is doubled. All frequencies have some degree of T_b decrease due to increased ice scattering. Higher frequencies experience more scattering. However, in test 6, when the hail content is doubled again, 85-GHz T_b

experience a smaller decrease than that of 37 GHz. This is consistent with Kodama et al. (2007) stating that at the presence of intense amounts of hail particles, 85 GHz tends to saturate and thus allows 37 GHz to exhibit a stronger sensitivity and serve as a better proxy for ice scattering in this situation. The 85-GHz T_b is more sensitive to relatively small precipitation-size ice particles in the upper part of clouds, while 37-GHz T_b is more sensitive to supercooled or large frozen or supercooled hydrometeors, such as large graupel, and large aggregated snowflakes right above the melting layer (Cecil and Zipser 2002; Kodama et al. 2007). Both 37 and 85 GHz are adopted to detect and classify ice microphysics fields in this convective storm.

TRMM passed over the LBA convective scene at 2100 UTC. Figure 4.2 shows the observed TMI T_b s at 37v and 85v. The enclosed box, measuring approximately 100 km by 100 km, is the focus of this study. The convective core shows up as T_b depression centers in both frequencies. The 85-GHz T_b depression is much deeper than the 37 GHz, which is consistent with results in Table 4.1.

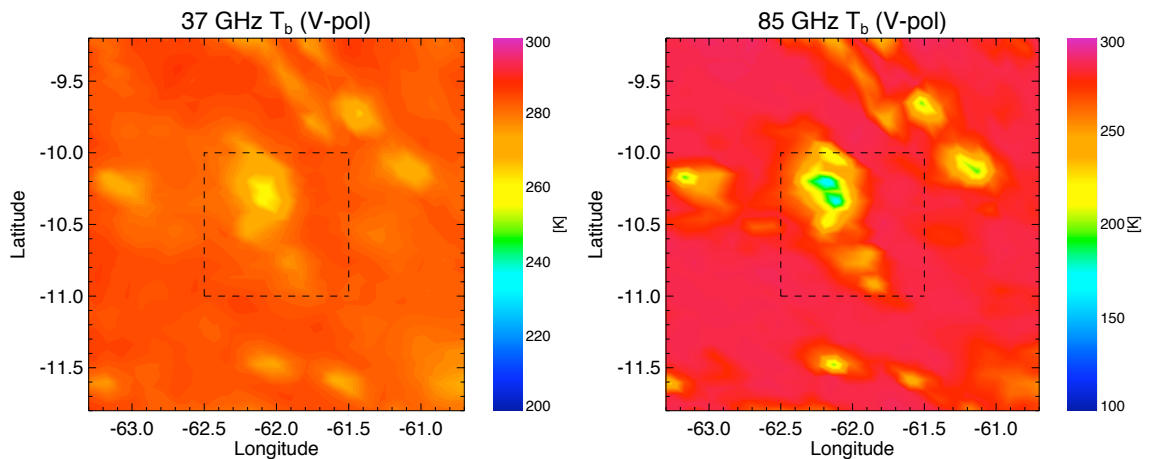


Figure 4.2 (left) TMI observed 85v T_b (right) and 37v T_b over a 3° by 3° scene. The 1° by 1° box enclosed by the dashed line is the focused area for this study.

4.2.2 Regional Atmospheric Modeling System (RAMS) Simulation

RAMS is used to simulate the convective storm for comparison with the observations. First of all, the model is described, as well as its microphysics parameterization schemes.

4.2.2.1 RAMS

The RAMS model (Cotton et al. 2003) is a CRM developed at Colorado State University (CSU) by merging a non-hydrostatic cloud model (Tripoli and Cotton 1982) and two hydrostatic-mesoscale models (Tremback et al. 1985; Mahrer and Pielke 1977). RAMS is built upon a full set of compressible atmospheric dynamic and thermodynamic equations using Arakawa-C grid and σ_z terrain-following coordinate system with variable vertical grid spacing to increase resolution near ground and in the boundary layer. The ‘time-split’ time differencing schemes are adopted to damp the propagation of the fast wave modes and several parameterizations are implemented to describe different physical processes.

4.2.2.2 RAMS MICROPHYSICS PARAMETERIZATION

The bulk microphysical schemes in RAMS (Walko et al. 1995; Meyers et al. 1997) define seven hydrometeor categories including cloud water, rain, pristine ice crystals, snow, aggregates, graupel, and hail. Within a grid, the hydrometeor size distributions are represented using a generalized gamma distribution function for each class

$$n(D) = N_t f_{gam}(D) = \frac{N_t}{\Gamma(\nu)} \left(\frac{D}{D_n} \right)^{\nu-1} \frac{1}{D_n} \exp\left(-\frac{D}{D_n}\right) \quad (4.1)$$

where the number density n is a function of the diameter D . Here, N_t is the total number concentration, Γ is the gamma function, ν is the shape parameter of the gamma distribution, and D_n is the characteristic diameter. The mass m of a particle with diameter D is expressed in power law formula

$$m = \alpha_m D^{\beta_m} \quad (4.2)$$

where α_m and β_m are coefficients that are constant for each species. Using the integral property of gamma distribution, the mean mass diameter can be calculated by

$$D_m = D_n \left(\frac{\Gamma(\nu + \beta_m)}{\Gamma(\nu)} \right)^{\frac{1}{\beta_m}} . \quad (4.3)$$

Hydrometeor density is given by

$$\rho_h = \frac{6\alpha_m}{\pi} D^{\beta_m - 3} . \quad (4.4)$$

For cloud, rain, graupel, and rain that are assumed spherical in the model, $\beta_m = 3$, therefore, their densities are held constant at 1000, 1000, 300, and 900 kg m⁻³, respectively. For pristine ice, snow, and aggregates, their densities vary with diameter.

The mass mixing ratio of the hydrometeor category is given by

$$r = \frac{N_t}{\rho_a} \alpha_m D_n^{\beta_m} \frac{\Gamma(\nu + \beta_m)}{\Gamma(\nu)} = \frac{N_t}{\rho_a} \alpha_m D_m^{\beta_m} . \quad (4.5)$$

Physical processes in the schemes include nucleation of cloud droplets, nucleation of ice crystals, vapor diffusional growth and heat diffusion, evaporation and sublimation, freezing and melting, collisions between hydrometeors, shedding of water by hail, sedimentation, and secondary ice production. Options of the parameterization include a one moment scheme in which either r or N_t is prognosed and D_n is diagnosed from Eq. (4.5), and a two moment scheme in which both r and N_t are prognosed given a prescribed

ν of the distribution. Between the two, the advantages of predicting two parameters of the hydrometeor size spectra in precipitation processes was noted in Srivastava (1978). Additionally, two moments can improve the prediction of complex microphysical processes by allowing more degrees of freedom of the hydrometeor spectra for each category. Improvements should also be expected in the calculations of radar reflectivity and radiative transfer calculations, which are both dependent on the realistic representation of size and the number concentration of the hydrometeors (Meyer et al. 1997). Therefore, the two moment scheme is adopted in this simulation.

4.2.2.3 SIMULATION OF THE STORM

A semi-ideal simulation starting at 1200 UTC on 23 February was run for 12 hours at 1 km horizontal resolution using RAMS to reproduce the characteristics of the LBA storm shown in Figure 4.2. The model configuration is summarized in Table 4.2. Vertical coordinate includes 40 levels with 37-m resolution near the surface so that the boundary processes can be well captured. The vertical resolution stretches up to 1028 m with a ratio of 1.14 and the model top extends to approximately 23 km. The model is initialized with Rebio Jaru station's 1200 UTC sounding with topography provided by the global U.S. Geological Survey (USGS) surface data (approximately 1-km resolution). Adopted parameterizations include Klemp/Wilhelmson lateral boundary condition with 20 m s^{-1} phase speed and Harrington radiation scheme for both shortwave and longwave radiation. The two moment microphysics scheme is adopted and the shape parameter ν of the size distribution for each hydrometeor is pre-assigned (3, 2, 2, 2, 2, 2, for cloud, pristine ice, snow, aggregates, graupel, and hail, respectively). The surface fluxes are nudged as surface forcing to help stimulate convection along thermodynamically unstable

Table 4.2 RAMS model configuration for the simulation.

Model aspect	Setting
Grid	Arakawa C grid Single grid Horizontal grid: $\Delta x = \Delta y = 1$ km 100 x 100 points Vertical grid: Δz variable; 40 vertical levels; Model top ~ 23 km
Initialization	Horizontally homogeneous Rebio Jaru station's 1200 UTC sounding
Topography	Global U.S. Geological Survey (USGS) surface data
Time step	4 s
Microphysics scheme	Two-moment bulk microphysics Water species: vapor, cloud water, rain, pristine ice, snow, aggregates, graupel, hail all activated CCN concentration: 250 cm^{-3}
Convection initiation	Observed surface forcing Latent and sensible heat fluxes are nudged
Boundary conditions	Klemp/Wilhelmson
Radiation scheme	Harrington

regions. Latent and sensible heat fluxes measurements collected at ABRACOS Hill and Ji Parana (Lang et al. 2007) are used to construct the flux time series expressed by cosine functions whose amplitudes and periods are determined from the observation data. The simulation of the storm is divided into two areas and the inner and outer areas are forced with both latent and sensible heat flux time series whose functions have different magnitudes but equal 11-hour periods. The Rebio Jaru sounding and details of the surface forcing used in this study can be found in Lang et al. (2007). Convection first kicks off at the boundary between these two areas where the forcing gradient is the largest and, therefore, the most unstable.

The first five hours of the simulation is considered “model spin-up time” when clouds start to form from the moist air. At around 1730 UTC, the domain-averaged surface rainfall is found to increase sharply during the next 1.5 hours and reach its peak at

1910 UTC. Rainfall starts to decrease afterwards as the storm decays. Simulation results are output every 10 minutes. The 47th output (hereafter referred to as T47), for instance, corresponds to 1950 UTC when the storm is experiencing the early stage of the decaying process. Model outputs include thermodynamic properties and hydrometeor profiles, from which the optical properties including extinction coefficients, scattering coefficients, and asymmetry parameters can be calculated to serve as inputs to simulate the T_b s at TMI frequencies. A two-stream radiative transfer model (Kummerow 1993) with Eddington approximation and an independent pixel plane-parallel assumption is used in this work as the observational operator. The differences between this model and an eight-stream discrete ordinate solution for the realistic and multilayered cloud hydrometeor profiles did not exceed 3° K for the microwave range between 6.6 to 183 GHz. Compared to the uncertainties from the microphysical profiles generated by the CRM, this model is accurate enough for the current purpose although it provides only an approximate 3-D effect and no polarization information of nonspherical particles (Kummerow 1993). Surface emissivity is initially fixed at 0.93 for all channels in the calculation. This value is based on the 2006 annual mean surface emissivity retrieved from Advanced Microwave Scanning Radiometer for EOS (AMSR-E) that carries similar frequencies as TMI (Bytheway and Kummerow 2010). The size distributions [Eq. (4.1)] and hydrometeor densities [Eq. (4.4)] for RAMS are used in the T_b simulations. The T_b s are then averaged from the model resolution to TMI resolutions using a 2-D Gaussian filter with the Full Width at Half Maximum (FWHM) set to each frequency's respective footprints (Kummerow et al. 1998). Cyclic boundary conditions are applied in the averaging.

The simulated T_b scenes for 37 and 85 GHz at TMI resolutions are displayed in Figure 4.3. When compared with the observed scenes presented in Figure 4.2, the

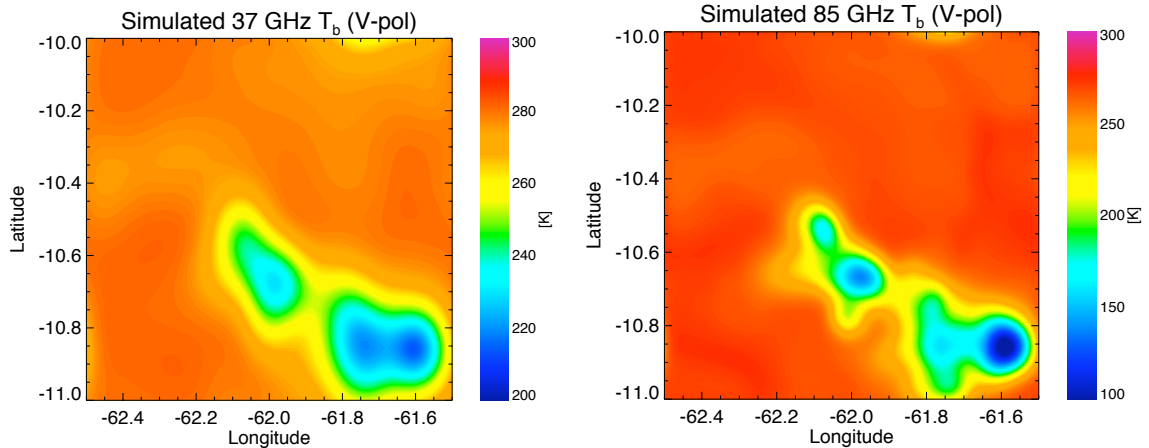


Figure 4.3 (left) Simulated 37-GHz and (right) 85-GHz T_b for the 1° by 1° study area at 1950 UTC during the decaying stage.

discrepancies are obvious. The simulated convective core is separated from the observed one by about half a degree (50 km) in the SE direction, and there also exists a separate weaker core on the NW of the main core. Besides the differences in location and morphology, the convection generated in the simulation is also more intense than the observation with T_b at 85 GHz around 100 K versus the observed value of 180 K. This indicates that either the model is over-producing large ice particles or T47 is early in the decaying process with the convections still too strong when compared to the observation snapshot.

4.3 Cluster Analysis

Different cloud regimes within the same storm system bear different microphysical properties. For example, the convective core contains hail and graupel particles produced in the strong updraft, while stratiform clouds are mostly composed of low-density

particles including pristine ice, snow, and aggregates. It is crucial for cloud models to produce correct microphysical properties for each cloud type so that realistic scattering/rainfall relationships are established by simulations for improved rainfall retrievals over land. To define cloud regimes in the scenes, “k-means cluster analysis” is employed to group pixels or grids with coherent physical properties.

4.3.1 Description of Analysis

Cluster analysis is a classification method that groups data with similar properties together into self-similar categories. First of all, centroids are chosen and the Euclidean distance from each data point to each centroid is computed. The data point is then assigned to the closest centroid. The center of each resulting cluster is recalculated and the distances are computed again to the new centroid and the clusters are redefined. The iterative process continues until the clusters are stable. The clustering analysis follows the work of Boccippio et al. (2005) and Finn (2006). The specific clustering technique used in this study is the “k-means technique” described by Anderbert (1973). Using cluster analysis, the storm scene can be classified into several cloud types, in which each cluster is expected to possess distinct microphysical properties.

Due to high surface emissivity over land, precipitation is generally retrieved through the scattering signals from large precipitating ice particles in the passive microwave methods. Targeted at improving land precipitation, the criteria for clustering in this study is based on ice microphysics. T_b s at high microwave frequencies are good proxies of ice microphysics, as was examined in the previous sensitivity experiments. Therefore, the T_b vector was clustered into similar 37v, 37h, 85v, and 85h T_b s. Because

the range of T_b at 85 GHz is significantly larger than at 37 GHz, scaling is applied first following:

$$T_b = T_b \times \frac{\max(T_b(85h)) - \min(T_b(85h))}{\max(T_b) - \min(T_b)} . \quad (4.6)$$

4.3.2 Determining the Number of Clusters to Use

The observation scene can be clustered into an arbitrary number of regimes. The optimal number should be chosen based on several criteria described below. Smaller mean standard deviations within each cluster are desired to ensure that each cluster represents self-similar cloud properties. A distinct range for each cluster is also desired so that pixels are not ambiguous in the classification and each cluster has unique microphysical characteristics. Finally, it is desirable for clusters to bear physical meanings instead of simply representing mathematical constructs. Classifications ranging from two to six clusters are assessed next.

With only two clusters, the convective and non-convective region emerges due to their first order difference in ice microphysical properties. The standard deviation of T_b within each cluster, however, is relatively large denoting large variability within each cluster. Mean standard deviation generally decreases with the number of clusters adopted. The mean and standard deviation of T_b s for each channel when using three, four, five, and six clusters are shown in Figure 4.4.

With three clusters, each cluster is distinctly separated for all channels. With four clusters, there exists overlap at 85 GHz but the clusters are distinct at 37-GHz classification; while with five clusters, there exists overlap at 37 GHz but the clusters are distinct at 85-GHz classification. However, when six clusters are used, T_b ranges overlap

for both frequencies between clusters, allowing ambiguity in classifying pixels located within the overlapping range. Therefore, the choice of six clusters is discarded. Cluster number three, four, and five are potential candidates with mathematical distinctness in each cluster to represent each cloud regime uniquely. The choice was made based on the uniqueness in physical properties for each cluster.

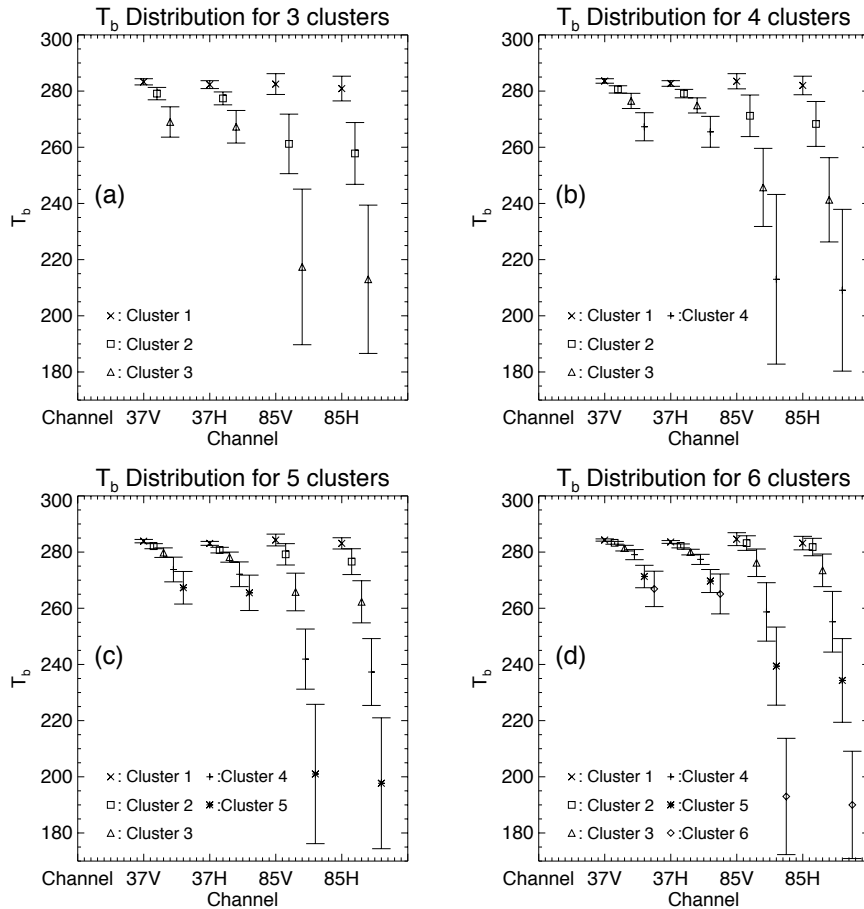


Figure 4.4 T_b distributions (mean and standard deviation) at 37 GHz and 85 GHz for each cluster at the case of (a) three clusters, (b) four clusters, (c) five clusters, and (d) six clusters.

Observed TMI T_b s, PR retrieved rainfall/water paths, and VIRS retrieved cloud properties can be used to infer physical properties of the underlying clouds within TMI 85-GHz footprints (Rapp et al. 2005). PR surface rain rate, 85-GHz polarization, 37- and

85-GHz T_b relationship, and mean visible cloud reflectance are examined together, as shown in Figure 4.5.

When three clusters are used, cluster 1 contains pixels with warm 37- and 85- GHz T_b s with a small standard deviation, as shown in Figure 4.4a. This cluster corresponds to nonraining pixels whose variance is mostly caused by factors such as surface emissivity and cloudiness. This cluster includes some ice particles that produce 85-GHz polarization signal and produces a mean visible reflectance around 0.55. Polarization at 85 GHz is an indication of ice particle shape and orientation (Anagnostou and Kummerow 1997; Prabhakara et al. 2001). Cluster 2 contains more ice that depresses the mean T_b s by 5 to 20 K, produces higher 85-GHz polarization and cloud reflectivity as well as some rain. Cluster 3 contains pixels with much lower T_b with large standard deviations that correspond to an inhomogeneous distribution of precipitating ice particles associated with the convective core that contains relatively high rain rates and large cloud reflectance (mean reflectance is 0.8), as shown in Figure 4.5.

For the case of four clusters, another cloud type between the nonraining cluster and convective cluster emerges. The two intermediate clusters, that is, cluster 2 and 3 correspond to pixels including different amounts and/or species of ice particles so that cluster 3 depresses the T_b s more strongly, produces higher rain rates and has larger polarization signals. These two clusters may include different microphysics and thus deserve being investigated further. Compared with using four clusters, one more intermediate cloud type is separated with five clusters. The physical properties of the new cluster tend to lie between those of cluster 1 and 2 of the four-cluster scenario, and its surface rainfall is very small. This makes this cluster less interesting to this work whose

focus is more on the microphysics of raining scenes. Therefore, four clusters are used as a compromise between mathematical similarity and physical interpretation.

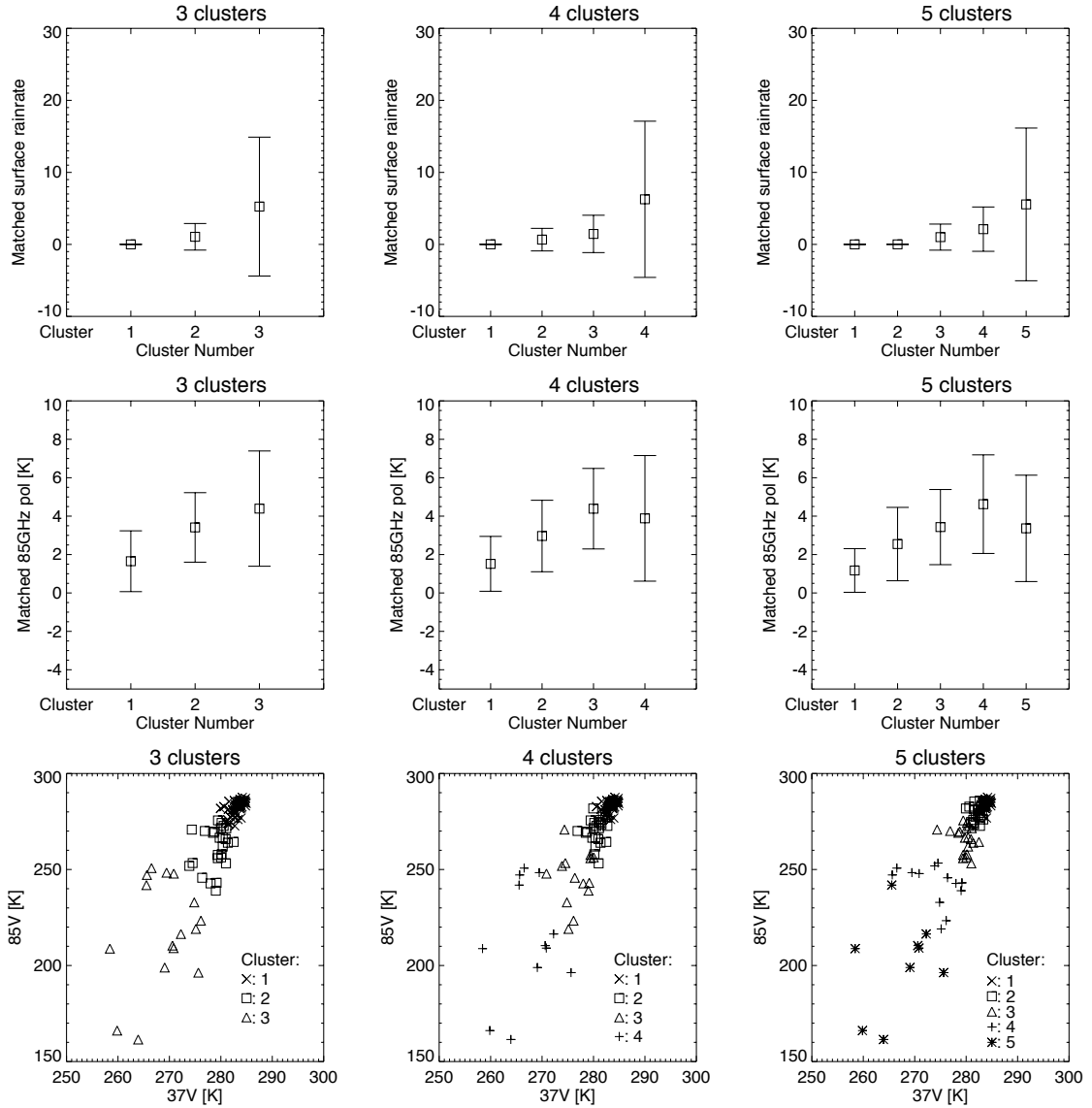


Figure 4.5 Physical property comparisons for using three clusters (left panels), four clusters (middle panels), and five clusters (right panels) including PR surface rainfall (upper panels), 85-GHz polarization information (middle panels), and T_b relationship between 85-GHz and 37-GHz T_b s (lower panels).

4.3.3 The Observed Clusters

Figure 4.6 displays the four clusters of the observation. Figure 4.7 shows the VIRS visible and infrared image of this storm with the contour of cluster 1 overlaid. The visible

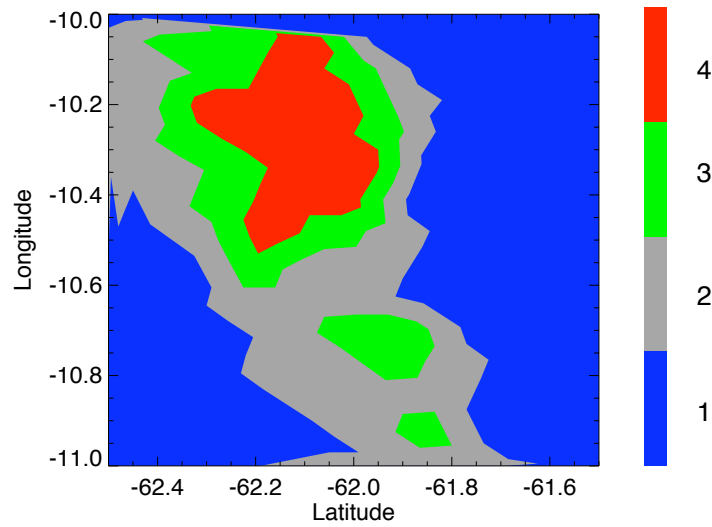


Figure 4.6 The four clusters for observation with clustering criteria defined by observation T_b scenes.

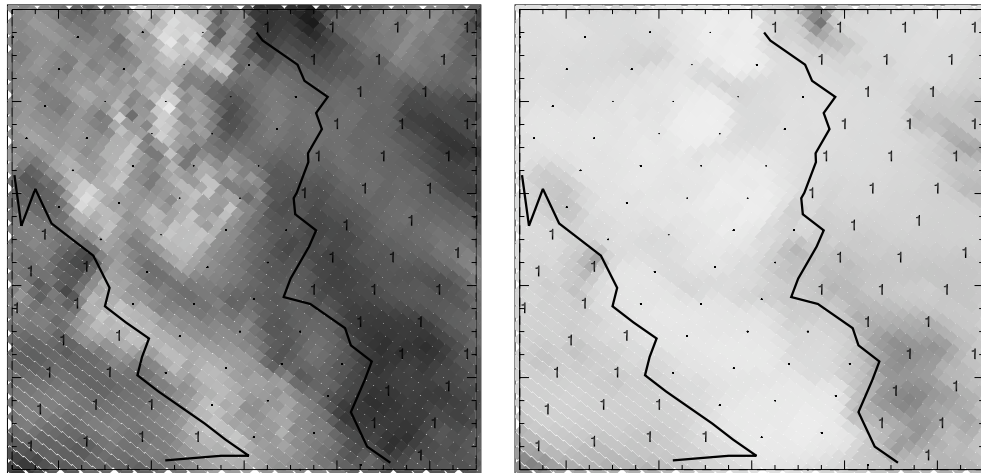


Figure 4.7 VIRS (left) visible and (right) infrared image at $10.8 \mu\text{m}$. Cluster 1 contour is overlaid.

image shows that cluster 1 compares well to the darker region of the visible image that is associated with the relatively lower reflectance (mean value for this cluster is 0.53). Cluster 1, therefore, can be associated with either clear sky or thin cirrus. The existence of thin cirrus is further confirmed by the silk-like morphology in the visible image and also the low cloud top temperature inferred from the infrared image. Together with the

fact that this cluster includes little rain as shown in Figure 4.5, cluster 1 is called the ‘clear sky/thin cirrus cluster’.

It is clear from the infrared image that the whole area of interest is mostly covered with clouds. The reflectance ratio of $0.6 \mu\text{m}/1.6 \mu\text{m}$ has been used in the MODIS cloud mask algorithms to identify the cloud phase (King et al. 1996). The absorption efficiency for both water and ice is small but similar around $0.6 \mu\text{m}$, while the absorption for ice is larger than that for water at around $1.6 \mu\text{m}$ (Warren 1984; Hale and Querry 1973) such that the reflectance at $1.6 \mu\text{m}$ is smaller for ice than for water. The ratio is thus larger for ice than for water. For each TMI pixel that is assigned a cluster number, reflectance ratios are calculated for all the VIRS pixels included within the TMI footprint. Figure 4.8 shows

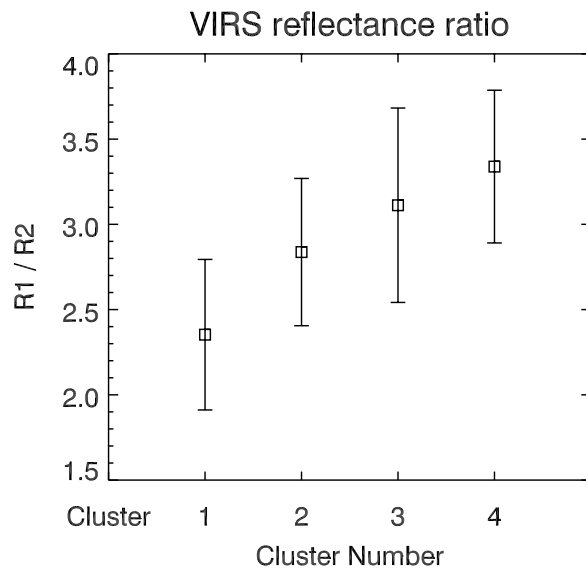


Figure 4.8 Reflectance ratio of the visible versus near-infrared channel on VIRS as a function of the cluster number with standard deviation imposed.

the mean and standard deviation of the reflectance ratio for each cluster. The ratio increases with cluster number, suggesting that the percentage of ice in the cluster increases with cluster number. Cluster 2, therefore, contains higher percentage of water

phase at the cloud top compared to clusters 3 and 4. Together with the cirrus cover as shown in the infrared image of Figure 4.7, cluster 2 is most likely associated with multi-layer clouds with lower level water clouds covered by cirrus. Figure 4.5 shows that this cluster produces small rain rates and this cluster is termed as the ‘cloudy’ regime.

Figure 4.5 shows that cluster 3 contains intermediate rain rates and has the strongest 85-GHz polarization signal with mean value greater than 4 K. Large polarization is caused by oriented nonspherical ice particles such as pristine ice, snow, and aggregates that exist in stratiform regions of the storm (Heymsfield and Fulton 1994a; Anagnostou and Kummerow 1997). The spatial location of cluster 3, surrounding the deep scattering denoted by cluster 4, provides evidence that cluster 3 corresponds to the storm’s stratiform anvil region. Figure 4.9 shows the cross section of the radar reflectivity at

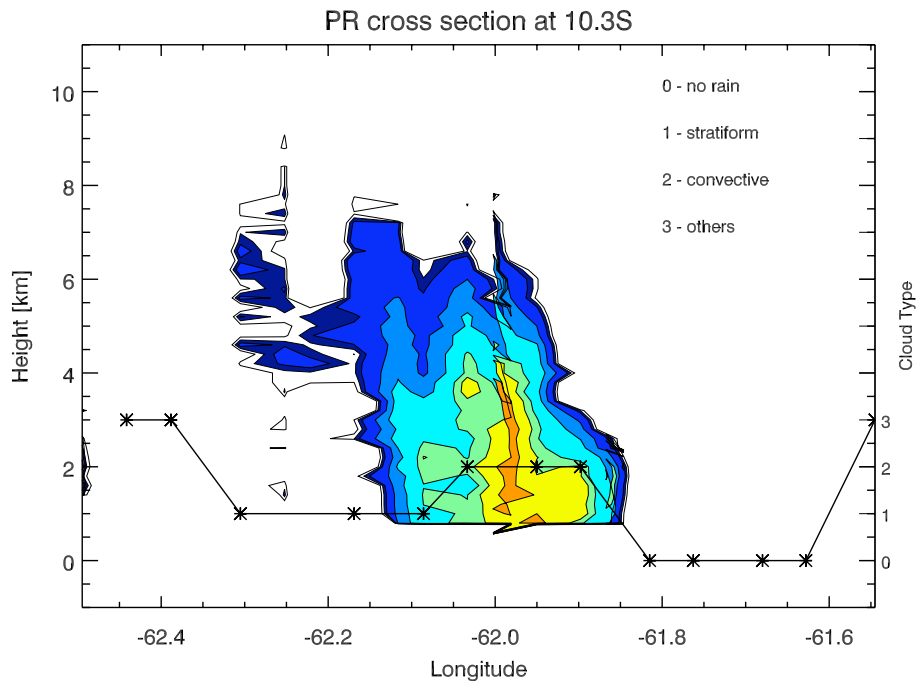


Figure 4.9 PR reflectivity cross section at 10.3°S overlaid by the cloud type classification from PR 2A25 algorithm.

10.3° S overlaid by the cloud type classification from PR 2A25 product. It is clear that the stratiform anvil lies adjacent to the convective core that corresponds to the high reflectivity region. Cluster 3 is defined as the ‘stratiform anvil cluster’.

Figure 4.5 shows that cluster 4 is associated with larger rainfall and more intense T_b depressions that are produced by strong scattering of large precipitating particles representative of the ‘convective core’. Resemblance of cluster 4 to the T_b depression areas in Figure 4.2 together with the higher reflectivity in Figure 4.9 further verify the convective properties of this cluster. Cluster 4, therefore, is defined as the ‘convective cluster’.

Liquid Water Path (LWP) and Ice Water Path (IWP) can be calculated from PR 2A25 products using the linearly interpolated precipitation water parameter coefficients from the five nodes (Iguchi et al. 2000). The mean LWP for each cluster is 0.02, 0.12, 0.59, and 0.76 kg m⁻²; and the mean IWP for each cluster is 0.01, 0.07, 0.19, and 0.72 kg m⁻². These values are consistent with the properties of the defined cloud types.

4.4 Analysis and Discussion

To compare the simulation to observation for each cloud type, the simulation clusters need to be defined first.

4.4.1 Assigning Simulation Pixels to Clusters

The simulation produces significantly different T_b s from the observations as evidenced by a comparison of Figures 4.2 and 4.3. Here, each simulation pixel is assigned to a corresponding observation cluster based on the pixel’s closeness to the clusters’ centroid T_b vectors to ensure that the two sets of clusters are based on the same criteria. For example, Figure 4.10 shows the simulation clusters for T47. The convective

cluster is consistent with the T_b depressions in Figure 4.3 and the stratiform portion of the simulated storm also lies adjacent to the convective core as in Figure 4.6.

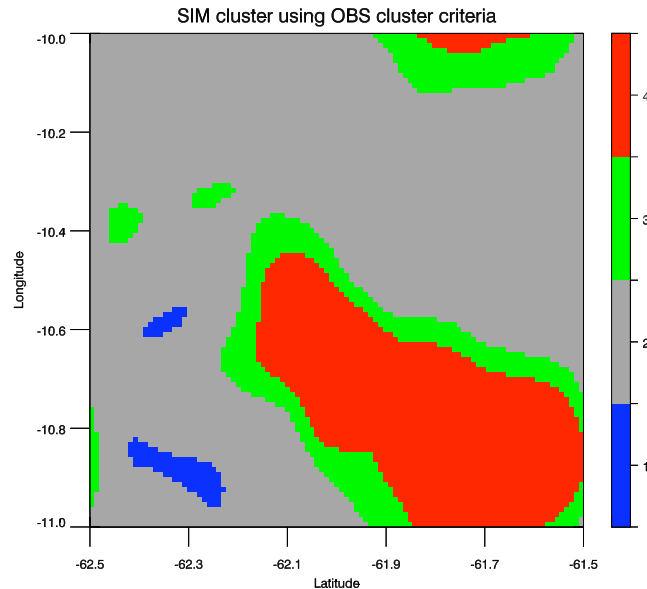


Figure 4.10 Simulation clusters at T47 based on the observation cluster criteria.

4.4.2 Analysis by Cluster

The CRM simulation for this convective cloud is semi-ideal and it has the ‘cold start’ procedure for model spin up before meaningful cloud and precipitation are predicted. However, the microphysical properties of a specific cloud type should be consistent regardless of the developing stages of the storm. Thus, T35, T47, and T59 at two hours’ interval that cover the cumulus, mature and decaying stages of the storm ensemble are combined together for analysis instead of deciding upon the closest (e.g., Wiedner et al. 2004) or the most appropriate (e.g., Lang et al. 2007) time step in the simulation for the comparisons.

Figure 4.11 shows the mean microphysical profiles for each simulation cluster. The profiles are averaged to TMI’s 85-GHz resolution applying the same Gaussian filter that is used in calculating the T_b s. Cluster 1 includes mostly clouds, as shown in panel

4.11a, which is caused by the overproduction of clouds in the model. Figure 4.12 shows the overwhelming cloud fields at the early stage (T35) and the mature stage (T47) of the

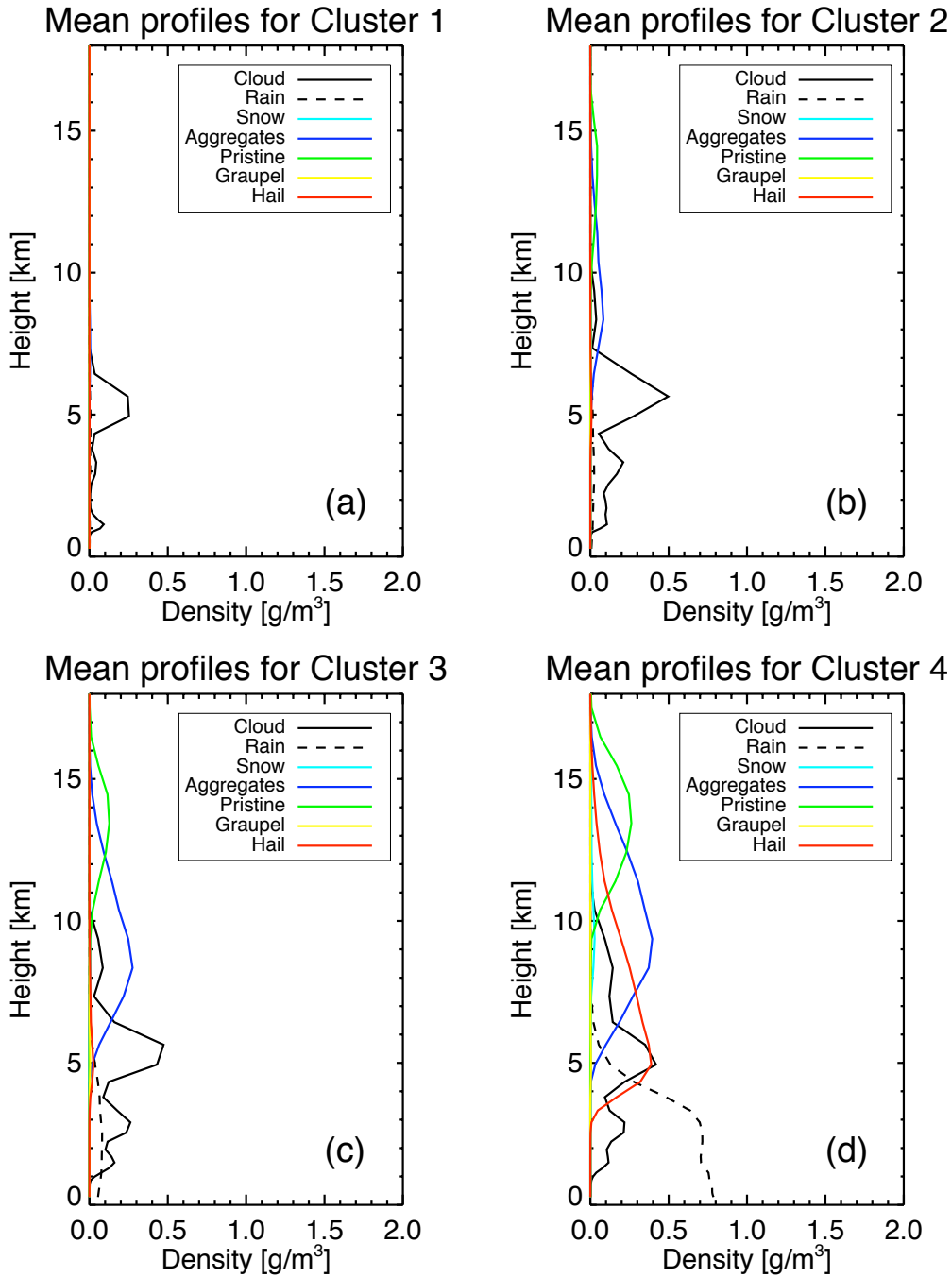


Figure 4.11 Mean profile of each hydrometeor species for each simulation cluster.

storm. This is most likely caused by the sounding used for the initialization, which is contaminated by mid-level clouds. The production of snow and graupel is small in this simulation. For clusters 2 to 4, pristine ice, aggregates, and rain amounts increase with the cluster number. Hail becomes abundant in cluster 4, which can also be seen from the hail mixing ratio contour in the right panel of Figure 4.12. The distribution of hail is consistent with the convective cluster in Figure 4.10.

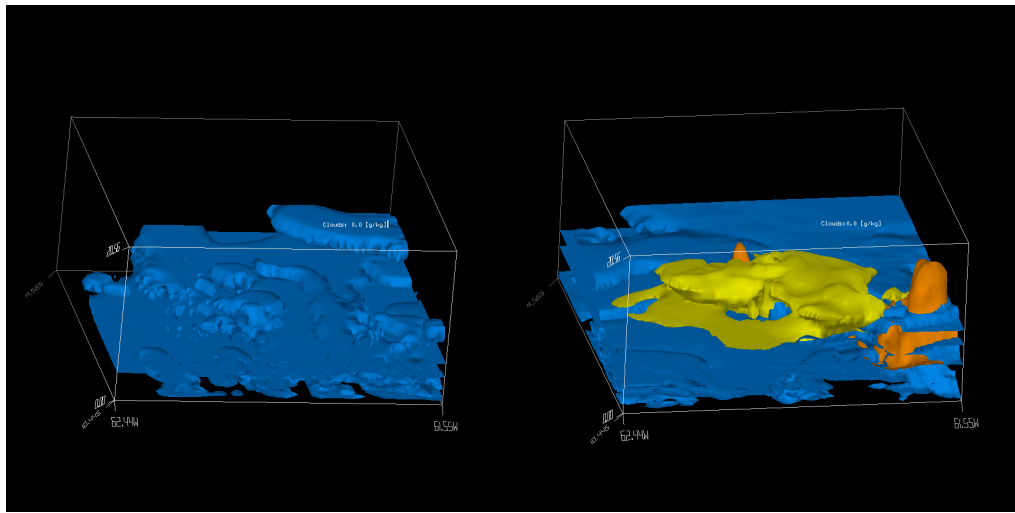


Figure 4.12 (left) Cloud field at T35 with contour mixing ratio of 0.0 g kg^{-1} ; (right) Cloud (blue), aggregates (yellow), and hail (orange) fields at T47 with contour mixing ratios of 0.0 g kg^{-1} , 1.0 g kg^{-1} , and 1.0 g kg^{-1} , respectively.

4.4.2.1 T_B COMPARISONS FOR CLUSTER 1

Figure 4.13a shows the comparison of the observed and simulated T_b ranges (within 1σ) for cluster 1 when the surface emissivity is fixed at 0.93 for each frequency. The comparison shows that the simulated T_b ranges at all channels are lower than the observed ones, and the discrepancies reach 5 K in some frequencies. Lower T_b s may be caused either by too little emission, too much extinction, or an insufficient signal from the surface. To test the sensitivity of the T_b discrepancies to potential errors in the column water vapor, all the water vapor profiles in this cluster are tuned to saturation. Figure

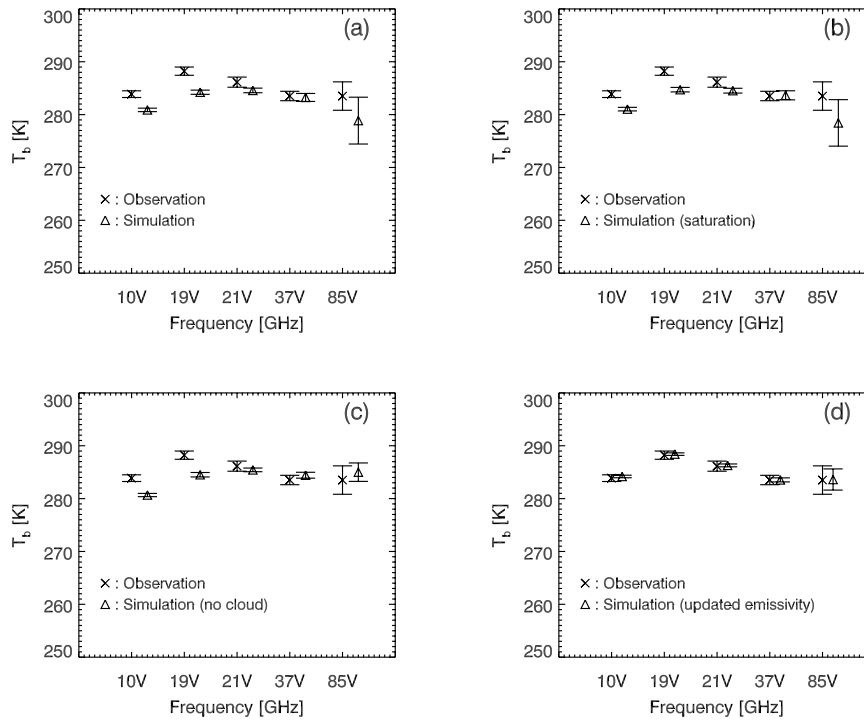


Figure 4.13 T_b comparison of cluster 1 at each frequency between observation and simulation in which (a) surface emissivity for each channel is set to 0.93; (b) water vapor profiles are set to saturation for each pixel; (c) all cloud particles are removed; d) surface emissivities are updated for each frequency.

4.13b shows that T_b s increase slightly, but the impact on reducing the discrepancies is negligible. The sensitivity to excessive extinction is examined by removing all the cloud particles. Figure 4.13c shows that the removal of cloud produces a negligible impact for the lower frequencies, while having an excessive impact over higher frequencies. Another potential bias source for the T_b simulation of this cluster is the presumed surface emissivities ϵ . The observed T_b s can be used to find the correct ϵ to be used in the model because thin cirrus is present in the observation cluster but it is basically invisible to the microwave frequencies. As such, the observations mostly reflect the surface properties. An average ϵ is obtained for each frequency from this cloud free cluster. A detailed

description of the physical relationship between T_b and ε can be found in Bytheway and Kummerow (2010). The new emissivities are employed for the rest of the clusters.

4.4.2.2 T_B COMPARISONS FOR CLUSTER 2

With different weighting functions, T_{bs} at 37 GHz (shortened as $T_b(37)$ hereafter) and T_{bs} at 85 GHz (shortened as $T_b(85)$ hereafter) exhibit different degrees of sensitivity to the microphysical properties, as manifested in Table 1. Figure 4.14a shows the T_b difference between 37v and 85v (shortened as dT_b hereafter) as a function of $T_b(85)$ between the observed scene and the simulated storms for cluster 2. A linear regression corresponding to the observed relationship (open squares) is plotted to highlight the differences with the simulated values (in gray scale). For this cluster, the simulation at $T_b(85)$ are somewhat colder than the observation. It also produces smaller dT_{bs} at the same $T_b(85)$.

To obtain a better match between the observation and the simulation, static adjustments of the simulated microphysics are performed. Mean freezing level in the simulation is approximately 4.63 km, and Figure 4.11b indicates the existence of large amounts of supercooled water in this cluster that is related to the initialization sounding. When the supercooled water is completely removed, the $T_b(85)$ range increases and the dT_b also increases at the same $T_b(85)$ as shown in Figure 4.14b. After the adjustment, the observation pixels are mostly included within the simulation. In this non-convective scene, the supercooled water can depress T_{bs} by elevating the weighting functions to lower temperatures. This liquid also decreases the dT_{bs} . Therefore, the removal of the supercooled water brings the dT_{bs} over $T_b(85)$ relationship closer to that of the observation for this cluster. The physical reason will be further explored in Section 4.3.

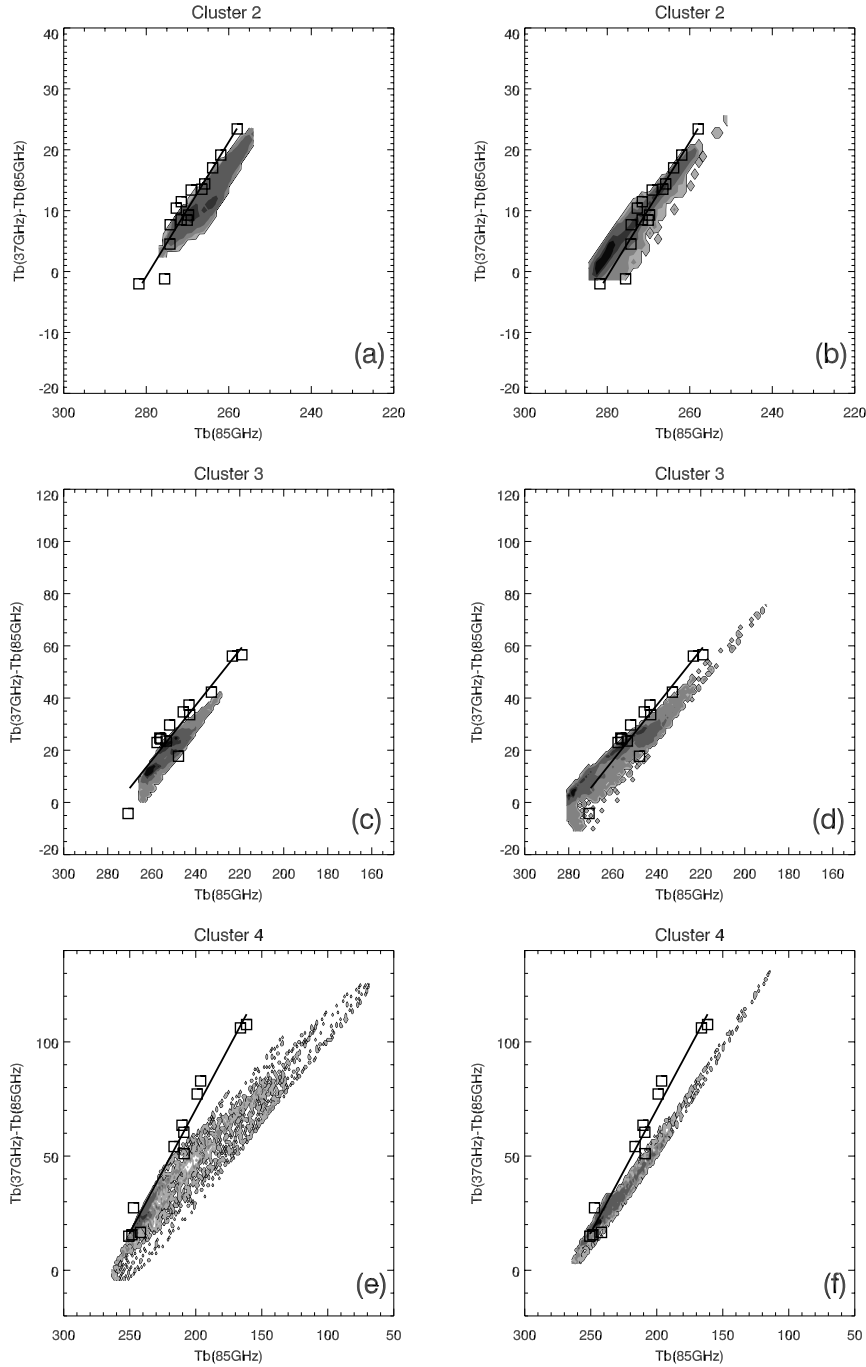


Figure 4.14 The dT_b over $T_b(85)$ relationship comparison between the observation and the simulation (a) for cluster 2 in the control run, (b) for cluster 2 in the sensitivity test when all the supercooled water is removed, (c) for cluster 3 in the control run, (d) for cluster 3 in the sensitivity test when all the supercooled water is removed, (e) for cluster 4 in the control run, and (f) for cluster 4 in the sensitivity test when the intercept of hail PSD is increased. Diamonds stand for the observed values, overlaid by its linear regression; gray scale contours stand for the simulated values.

4.4.2.3 T_B COMPARISONS FOR CLUSTER 3

Figure 4.11c shows that cluster 3 is dominated by clouds, pristine ice, and aggregates. The existence of the large amounts of nonspherical aggregates in the stratiform cloud is consistent with the observations, demonstrating the model's ability to produce the correct particle species. The simulated cluster produces higher $T_b(85)$ range and smaller dT_b at the same $T_b(85)$, shown in Figure 4.14c. As in cluster 2, removing all the supercooled water increases the dT_b and seems to fix the discrepancies quite well as shown in Figure 4.14d. Besides removing all the supercooled water, the match can be improved further by increasing the aggregates amounts while increasing the PSD's intercept to produce more but smaller aggregates particles.

4.4.2.4 T_B COMPARISONS FOR CLUSTER 4

Figure 4.11d shows that all hydrometeor species are further increased in cluster 4, especially the hail particles that are generally associated with strong convection. Figure 4.14e shows that the simulated dT_b s are lower than those in the observations and the underestimation is especially obvious in the low $T_b(85)$ regime, which is depressed by the large precipitating-sized ice particles (hail in this case). A few pixels in this cluster contain higher $T_b(85)$ s that extend into the lower cluster regimes. These outliers are found to be associated with relatively larger LWPs and lower $T_b(37)$. These lower $T_b(37)$ s will cause the pixels to be assigned to a higher cluster number even with relatively warmer $T_b(85)$ s. To facilitate our understanding, simplifications are made in this section including that the particle densities for all species are held constant and v , the shape parameter defined in Eq. (4.1), is assumed to be 1 for the size distribution of the precipitating particles. Figure 4.14f shows that when the intercept of the hail PSD is

increased, the simulated slope gets closer to that of the observation although there is still lack of agreement. A larger intercept with the same hail IWP produces more but smaller hail particles. This modification produces warmer $T_b(85)$ and larger dT_b , as was demonstrated from test 4 in Table 4.1.

4.4.3 General Relationships

Sensitivity tests are performed in this section to better understand the adjustments in Section 4.2. Figure 4.15a shows the dT_b over $T_b(85)$ relationship as a function of hydrometeor species over land. It can be seen that liquid species (cloud and rain) alone

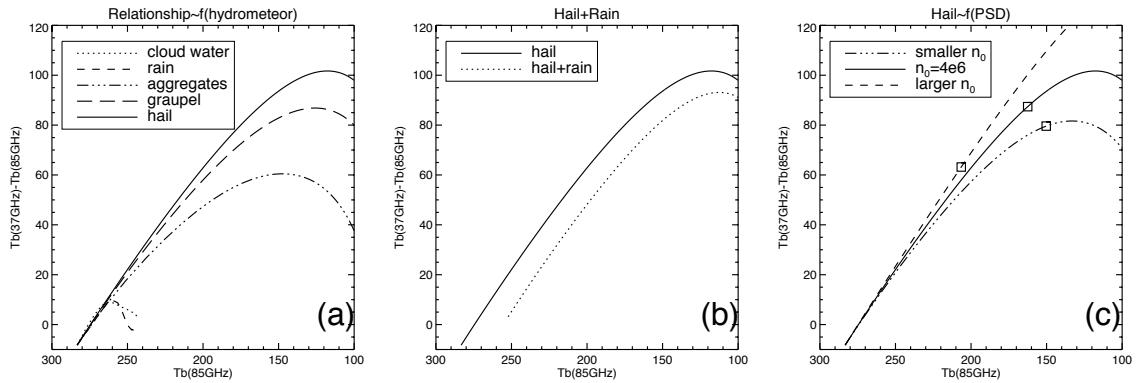


Figure 4.15 The relationship of dT_b over $T_b(85)$ as a function of (a) hydrometeor species, (b) hydrometeor combination, and (c) hail PSD. Squares denote the cases with the same hail IWP.

cannot produce very low $T_b(85)$ or very large dT_b . Maximum values for dT_b appear to be below 10 K. Ice species can produce much lower $T_b(85)$ and much larger dT_b . Hail can produce larger dT_b than graupel or aggregates. When rain is added to hail, as shown in Figure 4.15b, dT_b is lowered for all brightness temperatures. Figure 4.15c shows the impact of changing the intercept parameter on the dT_b versus $T_b(85)$ fit. It is revealed that hail Particle Size Distribution (PSD) with larger n_0 can produce larger dT_b at the same $T_b(85)$.

Mie theory is applied here to understand the above results. The size parameter x is defined as $x = 2\pi r / \lambda$, where r is the particle radius and λ is the wavelength. As the λ of 85 GHz is approximately 2.3 times smaller than that of 37 GHz, the x of 85 GHz is roughly 2.3 times larger than that of 37 GHz for a particle with the same size.

Figure 4.16 shows the Mie extinction efficiency Q_{ext} as a function of x for three particles with different dielectric properties. Their refractive indices are $1.77+1.0i$, $1.77+0.0001i$, and $1.33+0.0001i$, that roughly represent properties of rain, hail, and graupel, respectively. The real part of a refractive index represents the scattering characteristics while the imaginary part represents the absorption characteristics of the

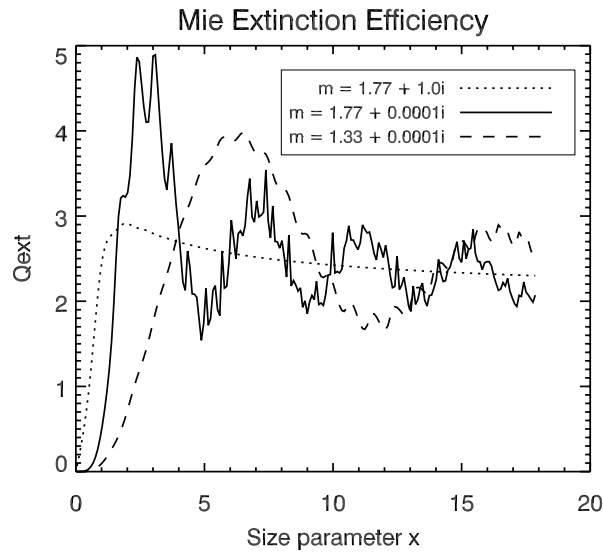


Figure 4.16 Mie extinction efficiency as a function of x for particles with different refractive indexes.

particle. For all three cases, the difference in Q_{ext} between 37 and 85 GHz increases until x for 85 GHz reaches the Q_{ext} peak, after which the difference decreases. For rain, the peak x is approximately 2, which is equivalent to a radius of 1.1 mm at 85 GHz. Therefore, liquid drops cannot produce very large dT_b since larger drops reduce the dT_b value.

Furthermore, adding liquid to ice will weaken the ability to produce large dT_b at the same 85 GHz. Liquid particles have large imaginary refractive indices, so that they are both efficient absorbers and emitters. Therefore, liquid drops cannot produce very low $T_b(85)$ s. Aggregates, graupel, and hail particles are all regarded as ice matrix with air inclusions in the calculation of their dielectric constants (Maxwell-Garnett 1904). The density of hail is larger than that of graupel, which is larger than the density of aggregates. These densities will determine the fraction of air inclusion and thus the refractive index of the mixture. As hail has a larger real part in the refractive index than graupel, its slope before the Q_{ext} peak is steeper, as shown in Figure 4.16, and, therefore, the dQ_{ext} difference is larger. This produces a larger dT_b . The decrease of dT_b after the peak of the curves in Figure 4.15 is caused by the decrease of 85-GHz Q_{ext} after its peak in Figure 4.16. This explains the phenomena that in the extremely intense convective storms, $T_b(85)$ saturates while $T_b(37)$ has a larger sensitivity on the storm intensity (Kodama et al. 2007).

To aid in the interpretation, the special case of $\nu=1$ for the generalized gamma distribution, Eq. (4.1) reduces to the exponential distribution:

$$n(D) = \frac{N_t}{D_n} \exp\left(-\frac{D}{D_n}\right). \quad (4.7)$$

Compared with the general form of the exponential distribution $n(D) = n_0 e^{-\lambda D}$, the intercept is

$$n_0 = \frac{N_t}{D_n} \quad (4.8)$$

and the slope is

$$\lambda = \frac{1}{D_n}. \quad (4.9)$$

Liquid Water Content (LWC) or Ice Water Content (IWC) of spherical particles can be expressed as

$$LWC / IWC = \int_0^{\infty} \frac{\pi}{6} D^3 \rho(D) n(D) dD = \frac{n_0 \pi \rho}{\lambda^4}, \quad (4.10)$$

which gives

$$\lambda = \left(\frac{n_0 \pi \rho}{LWC} \right)^{1/4}. \quad (4.11)$$

From Eqs. (4.8), (4.9), and (4.11), we can get

$$N_t = n_0 D_n = \frac{n_0}{\lambda} = n_0^{3/4} \left(\frac{LWC}{\pi \rho} \right)^{1/4}. \quad (4.12)$$

With the same hail IWC, larger intercept n_0 produces larger N_t from Eq. (4.12), which means more hail particles. It also produces larger λ as seen from Eq. (4.11), which means a smaller D_n according to Eq. (4.9) and hence a smaller D_m according to Eq. (4.3). In other words, while the mass is conserved, there will be more but smaller hail particles when the intercept n_0 gets larger. Squares in Figure 4.15c correspond to the cases that share the same hail IWP at different PSD. By increasing the PSD intercept, more but smaller hail particles produce larger dT_b at the same $T_b(85)$.

The dT_b over $T_b(85)$ relationship was demonstrated above to contain information of the microphysical properties and the observed relationship. It can, therefore, be used to diagnose the model microphysics.

4.4.4 Dynamic Adjustments

The adjustments in Section 4.2 demonstrate that static modification of the simulated microphysics can produce improved agreement with the observation. However, these static adjustments ignore the pertinent microphysical processes. Changing the hail

PSD intercept will not only change the hail sizes, but also the mean terminal fall velocity that modulates the collection and coalescence process and also the evaporation and melting processes that impact the strength of the downdraft and the intensity of the cold pool (Van Den Heever and Cotton 2004). To this end, a dynamic adjustment provides a more consistent and physical picture. Taking cluster 4 as the example, the goal of this section is to perform a dynamic adjustment that leads to more abundant but smaller hail particles compared with the control run.

Keeping all the settings identical to the control run, a sensitivity experiment is carried out by increasing the hail PSD ν from 2 to 5. This experiment is named ‘HAILGNU5’. The PSD and particle densities follow the same ones as in RAMS for the T_b simulation in this section. Comparison of Figures 4.17a and 4.17b shows that the dT_b

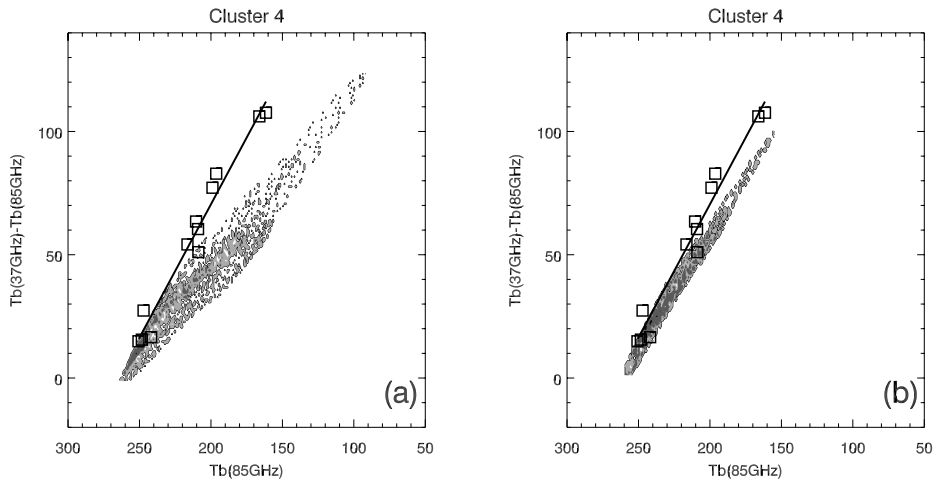


Figure 4.17 The dT_b over $T_b(85)$ slope comparisons for cluster 4. (a) Control run with hail shape parameter set to 2; (b) sensitivity run with hail shape parameter set to 5.

over $T_b(85)$ relationship in HAILGNU5 gets significantly closer to that of the observation than in the control run. It is noteworthy again that compared with the improvement in Figure 4.14f, this adjustment in HAILGNU5 is physically and microphysically consistent. Figure 4.18 shows the comparisons of the mean density and number

concentration N_i of cluster 4 for each species and also the comparison of the mean D_m for hail. Panels 4.18n and 4.18o reveal that HAILGNU5 is capable of generating more abundant (larger N_i) but smaller (smaller D_m) hail particles.

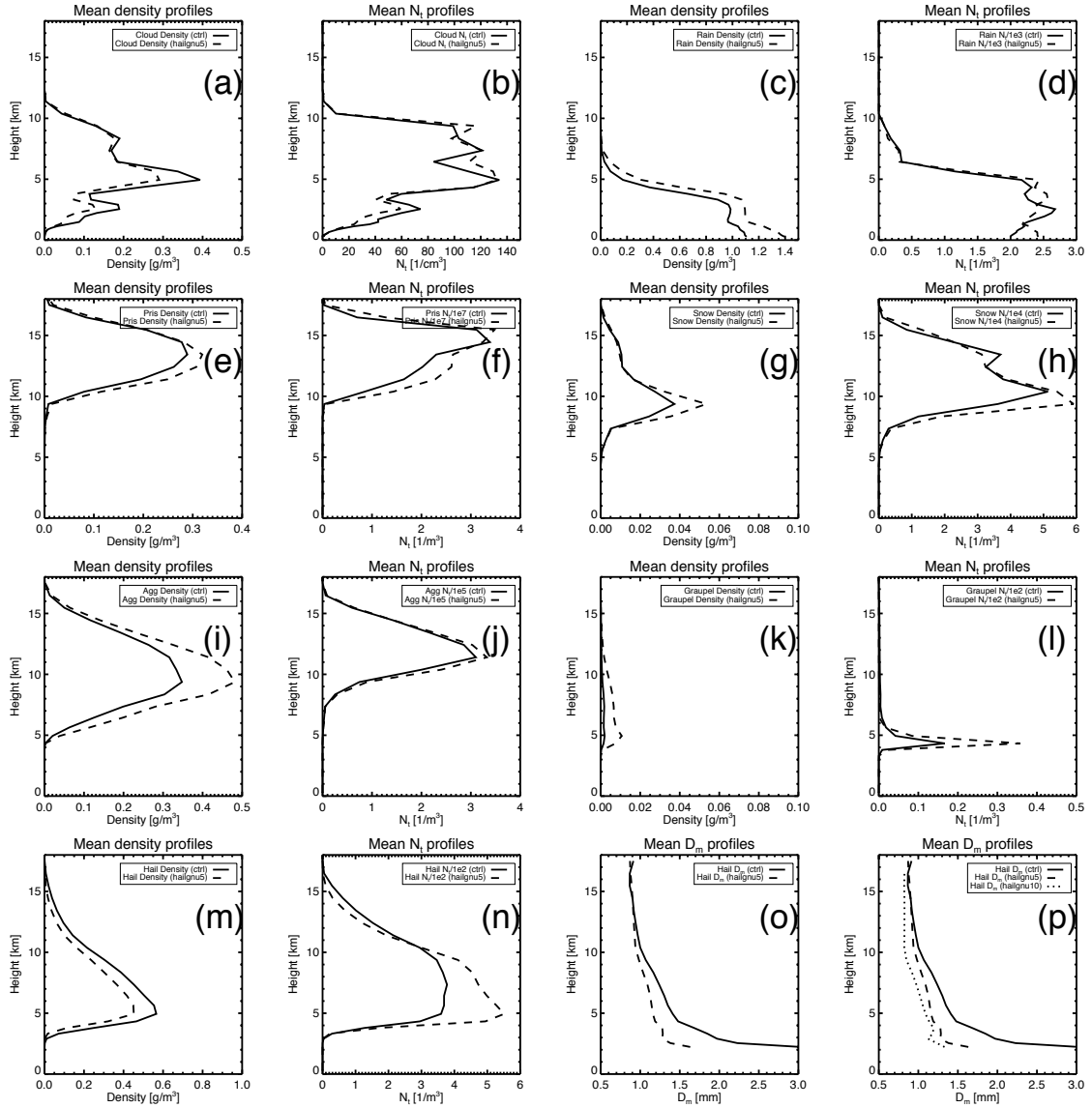


Figure 4.18 (a-n) Comparison of the mean density and number concentration N_i of cluster 4 for each hydrometeor species. (note that the scale for N_i is different for each species); (o) comparison of the mean hail D_m of cluster 4; (p) comparison of the hail mean D_m comparison for the simulation with $v=2, 5$, and 10 , individually.

Figure 4.18 illustrates the model behavior. With a fixed D_m , the distribution gets narrower when ν is increased (refer to Figure 1 in Walko et al. 1995) and D_n decreases in value. In RAMS, smaller D_n values result in reduced bulk collection rates for hail owing to the reduced terminal velocity associated with smaller D_n ; the riming efficiency of hail in the binned riming scheme is dependent on particle sizes and is, therefore, also impacted (Loftus 2011). These changes will on the other hand augment the other processes. It can be seen from Figure 4.18 that the mean density and N_t for pristine ice, snow, and aggregates all increase. The melting of these ice particles produces more rain drops and the increased rain droplets in turn collect more low-density ice particles if these rain drops are able to rise above the freezing level, i.e., in updraft, to produce the resultant more abundant but smaller hail particles compared with the control run. Figure 4.18p shows that the D_m of hail is further decreased when ν is increased to 10. This verifies that the change of hail properties from increasing hail ν can be reproduced.

CHAPTER 5

CONCLUSIONS AND FUTURE WORK

Microwave radiation is unique due to its longer wavelength and its direct interaction with the hydrometeors, hence, the microwave radiances contain valuable information of the microphysical properties. Chapter 2 described the radiative transfer of the microwaves through a precipitating atmosphere and the interaction with hydrometeors at microwave frequencies in a great detail, focusing on microwave imagers. Surface type, that is ocean or land, plays an important role in interpreting the microwave observations. The ocean surface is radiometrically cold so that the emissions from the raining cloud at lower frequencies (< 37 GHz) stand out from the background. The land surfaces generally have high emissivities and, therefore, only the scattering signal from precipitating-ice particles within the storm can be detected by the higher frequencies (≥ 37 GHz). These observations can, therefore, serve as microphysics proxies and can be used for model and observation comparisons. Chapter 3 and 4 each presented a model and observation comparison case using low SSM/I frequencies over ocean and high TMI frequencies over land.

GPROF and 1D-Var rainfall retrievals are compared, as they are both inversion algorithms based on the Bayes' theorem aimed at reproducing the observations given available *a-priori* information. The PR/TMI combination does allow the combined

algorithm to partition the cloud and rainwater. GPROF utilizes an observationally generated database from PR/TMI while 1D-Var uses the ECMWF model forecast FG field of temperature and moisture for *a-priori* information. The state vector to be solved in the minimization procedure includes microphysical profiles in GPROF and thermodynamic profiles in the 1D-Var. Retrieved microphysical properties for 1D-Var are outputs from the moist physics schemes given the retrieved temperature and humidity profiles and other model variables as inputs. However, 1D-Var makes use of an imperfect moist physics parameterization, which must also be linearized for assimilation purposes. The moist physics controls the ratio of cloud to rain in the 1D-Var retrievals, but this ratio is much higher than observed in the GPROF database, i.e., modeled cloud amounts are excessive as a fraction of rain amounts. The cloud and rainwater partitioning in the 1D-Var model was, therefore, evaluated using the GPROF *a-priori* database in this study.

Comparisons were first made using case studies of raining pixels extracted from 12-hour data on 30 September 2007 over a 10° by 10° region in the tropical east Pacific centered at $[120^\circ\text{W}, 10^\circ\text{N}]$. Differences between the two retrieval algorithms can be categorized into four categories based upon their agreements on three-channel T_{bs} and on their CWP/RWP ratios. Among the four categories, category 2 defined the scenario when T_{bs} agree while microphysics did not. This is the category in which the retrieval is successful at reproducing the T_{bs} but the retrieved cloud and rain properties was not observed by PR/TMI. From statistical analysis using one month's global retrievals in October 2008, it was found that category 2 occurred as often as 46.9% of all the 1D-Var retrievals. The agreement in T_{bs} was due to the comparable retrieved TPW between the two algorithms to match the same observation signals, while the microphysical

discrepancy was found specifically to be due to the difference in allocating the TWP between CWP and RWP. The dependence of the bias on regional variability was explored by selecting four regimes including the SE Pacific regime, the West Pacific regime, the East Pacific regime, and the Northern Hemisphere storm track regime. It was found that although all regimes shared the same issue of improper distribution of cloud and rainwater within the 1D-Var cloud scheme, the two retrievals produced similar spatial patterns. The dependence of the ratio on spatial variability was found to be related to the portion of stratiform rain, although the definition of stratiform was not equivalent in these two algorithms.

This work explored solutions to improve the cloud/rain ratio in the 1D-Var retrieval using several representative raining cases that have a wide range of rain intensities. It was found that the implementation of higher microwave frequency channels was beneficial to better constrain the ratio due to increased sensitivity at these frequencies in differentiating cloud water from rainwater. Adding in 37 GHz was sufficient for drizzle cases ($\leq 1 \text{ mm h}^{-1}$) while adding in 85 GHz had a greater impact for larger rain rate cases ($\geq 5 \text{ mm h}^{-1}$). Therefore, to improve the retrieval quality, we suggest that higher frequencies be added to the 1D-Var's three-channel retrieval algorithm. The comparisons between GPROF and 1D-Var can also be applied to other inversion algorithms.

Limited by the computation efficiency and current knowledge, CRM microphysics parameterizations still require significant assumptions. Biases in the CRM microphysics need to be identified and corrected. This work developed a method to use remote sensing observations to diagnose the model microphysical deficiencies in

different cloud types so that improvement of the simulations of each cloud type can be made separately. The work focuses on illustrating the methodology instead of exploring the exhaustive solutions of the improvement, which will depend on the specific cloud model and simulation.

A convective storm was captured by TRMM at its decaying stage over the TRMM LBA region. Frequencies at 37 and 85 GHz were sensitive to ice scattering and can be used as proxies of ice microphysics in the convective storms. Cluster analysis of the T_{bs} at 37 and 85 GHz of TMI was performed and four clusters are found to be the optimal choice for representing the distinct microphysics over the selected storm scene. Using the matched retrieval properties from PR and VIRS, the four associated cloud types were labeled as: ‘clear/thin cirrus’, ‘cloudy’, ‘stratiform anvil’, and ‘convective’. The relationship of dT_b versus $T_b(85)$ was found to contain relevant information of the microphysical properties including hydrometeor species and size distributions. It was found that the semi-ideal simulation produced an overwhelmingly cloudy background, and proper surface ϵ values in the RTM were essential to provide a consistent clear sky background. To improve the simulated relationships of the ‘cloudy’ and ‘stratiform’ cluster, the large amounts of supercooled water needed to be removed. Keeping the same hail content but fixing the hail size distribution generally fixed the T_b for the ‘convective’ cluster. Physically consistent microphysical pictures instead of static adjustment of the microphysical scenes were desired. To demonstrate the dynamic adjustment with the goal of improving the microphysics of the convective cluster, a sensitivity simulation was carried out by increasing the hail PSD gamma exponent value. Compared with the control run, the new simulation was capable of producing more but smaller hail particles and,

therefore, generating a closer relationship to that of the observation.

When field experiments are not easily available, the specification of the engineering parameters in the parameterizations that need to be prescribed by the model users are uncertain and should ideally depend on the types of clouds being simulated. This work provides a procedure of using satellite observations to guide the choice of these adjustable parameters. In the long term, this work also reveals the potential of constraining these parameters using data assimilation techniques.

The improved microphysics, especially of the ice species, can help build improved microphysics-radiation databases for the microwave physical rainfall retrieval algorithms over land. The improved microphysics in the CRMs can also provide improved precipitation products at higher temporal and spatial resolutions, which is demanded by the hydrological communities. The method can also be applied to other types of satellite observations that may contain sensitivity to different microphysical properties.

REFERENCES

- Adler, R. F., H.-Y. M. Yeh, N. Pasad, W.-K. Tao, and J. Simpson, 1991: Microwave simulations of a tropical rainfall system with a three-dimensional cloud model. *J. Appl. Meteor.*, 30, 924-953.
- Anagnostou, E. N., and C. Kummerow, 1997: Stratiform and convective classification of rainfall using SSM/I 85GHz brightness temperature observations. *J. Atmos. Ocean. Tech.*, 14, 570-575.
- Anderbert, M. R., 1973: *Cluster analysis for applications*. Academic Press, New York.
- Bauer, P., 2001a: Over-ocean rainfall retrieval from multisensor data of the Tropical Rainfall Measuring Mission. Part I: Design and evaluation of inversion databases. *J. Atmos. Ocean. Tech.*, 18, 1315-1330.
- Bauer, P., 2001b: Including a melting layer in microwave radiative transfer simulation for clouds. *Atmos. Res.*, 57, 9-13.
- Bauer, P., A. J. Geer, P. Lopez, and D. Salmond, 2010: Direct 4D-Var assimilation of all-sky radiances. Part I: Implementation. *Quart. J. Roy. Meteor. Soc.*, 136, 1868-1885. Also available as ECMWF Tech. Memo. 618, from <http://www.ecmwf.int>.
- Bauer, P., P. Amayenc, C. D. Kummerow, and E. A. Smith, 2001: Over ocean rainfall retrieval from multi-sensor data of the Tropical Rainfall Measuring Mission. Part II: algorithm implementation. *J. Atmos. Oceanic Technol.*, 19, 1838-1855.
- Bauer, P., E. Moreau, F. Chevallier, and U. O'Keefe, 2006a: Multiple-scattering microwave radiative transfer for data assimilation. *Quart. J. Roy. Meteor. Soc.*, 132, 1259-1281.
- Bauer, P., P. Lopez, A. Benedetti, D. Salmond, and E. Moreau, 2006b: Implementation of 1D+4D-Var assimilation of precipitation-affected microwave radiances at ECMWF. I: 1D-Var. *Quart. J. Roy. Meteor. Soc.*, 132, 2277-2306.

- Bauer, P., P. Lopez, D. Salmond, A. Benedetti, S. Saarinen, and E. Moreau, 2006c: Implementation of 1D+4D-Var assimilation of precipitation-affected microwave radiances at ECMWF: II: 4D-Var. *Quart. J. Roy. Meteor. Soc.*, 132, 2307-2332.
- Berg, W., and R. Chase, 1992: Determination of mean rainfall from the special sensor microwave/imager (SSM/I) using a mixed lognormal distribution. *J. Atmos. Ocean. Tech.*, 9, 129-141.
- Berg, W., C. Kummerow, and C. Morales, 2002: Differences between east and west Pacific rainfall systems, *J. Climate*, 15, 3659-3672.
- Berg, W., T. L'Ecuyer, and S. van den Heever, 2008: Evidence for the impact of aerosols on the onset and microphysical properties of rainfall from a combination of satellite observations and cloud-resolving model simulations. *J. Geophys. Res.*, 113, D14S23, doi:10.1029/2007JD009649.
- Biggerstaff, M. I., E.-K. Seo, S. Hristova-Veleva, and K.-Y. Kim, 2006: Impact of cloud model microphysics on passive microwave retrievals of cloud properties. Part I: Model comparison using EOF analyses, *J. Appl. Meteor.*, 47, 930-954.
- Blossey, P. N., C. S. Bretherton, J. Cetrone, and M. Kharoutdinov, 2007: Cloud-resolving model simulations of KWAJEX: Model sensitivities and comparisons with satellite and radar observations. *J. Atmos. Sci.*, 64, 1488-1508.
- Boccippio, D. J., W. A. Petersen, and D. J. Cecil, 2005: The tropical convective spectrum. Part I: Archetypal vertical structures. *J. Climate*, 18, 2744-2769.
- Bytheway, J., and C. Kummerow, 2010: A Physically Based Screen for precipitation over complex surfaces using passive microwave observations. *IEEE Trans. Geosci. Remote Sensing*, 48(1), 299-313.
- Cecil, D. J., and E. J. Zipser, 2002: Reflectivity, ice scattering, and lightning characteristics of hurricane eyewalls and rainbands. Part II: Intercomparison of observations. *Mon. Wea. Rev.*, 130, 785-801.
- Chaboureaud, J.-P., J.-P. Cammas, P. J. Mascart, J.-P. Pinty, and J.-P. Lafore, 2002: Mesoscale model cloud scheme assessment using satellite observations. *J. Geophys. Res.*, 107, 4301, doi:10.1029/2001JD000714.
- Chang, A. T. C., L. S. Chiu, C. Kummerow, and J. Meng, 1999: First results of the TRMM microwave imager (TMI) monthly oceanic rain rate: comparison with SSM/I. *Geophys. Res. Lett.* 26, 2379-2382.
- Chevallier, F., and P. Bauer, 2003: Model rain and clouds over oceans: Comparison with SSM/I observations. *Mon. Wea. Rev.*, 131, 1240-1255.

- Chevallier, F., and G. Kelly, 2002: Model clouds as seen from space: Comparison with geostationary imagery in the 11- μ m window channel. *Mon. Wea. Rev.* 130, 712-722.
- Cifelli, R., W. A. Petersen, L. D. Carey, S. A. Rutledge, and M. A. F. da Silva Dias, 2002: Radar observations of the kinematic, microphysical, and precipitation characteristics of two MCSs in TRMM LBA, *J. Geophys. Res.*, 107(D20), 8077, doi:10.1029/2000JD000264.
- Conner, M. D., and G. W. Petty, 1998: Validation and intercomparison of SSM/I rain-rate retrieval methods over the continental United States, *J. Appl. Meteor.*, 37, 679-700.
- Cotton W. R., and Coauthors, 2003: RAMS 2001: Current status and future directions. *Meteor. Atmos. Phys.*, 82, 5-29.
- Czekala, H., 1998: Effects of ice particle shape and orientation on polarized microwave radiation for off-nadir problems. *Geophys. Res. Lett.*, 25, 1669-1672.
- Eddington, A. S. 1916: On the radiative equilibrium of the stars. *Mon. Not. Roy. Astronom. Soc.* 77, 16-35.
- Elsaesser, G. S., and C. D. Kummerow, 2008: Toward a fully parametric retrieval of the nonraining parameters over the Global Oceans, *J. Appl. Meteor.*, 47, 1599-1618. DOI: 10.1175/2007JAMC1712.1.
- Evans, K. F., and G. L. Stephens, 1995: Microwave radiative transfer through clouds composed of realistically shaped ice crystals. Part I: Single scattering properties. *J. Atmos. Sci.*, 52, 2041-2057.
- Evans, K. F., and J. Vivekanandan, 1990: Multiparameter radar and microwave radiative transfer modeling of nonspherical atmospheric ice particles. *IEEE Trans. Geosci. Remote Sens.*, 28, 423-437.
- Ferraro, R. R., 2007: Past, present and future of microwave operational rainfall algorithms. In: *Measuring Precipitation from Space - EURAINSAT and the Future*, V. Levizzani, P. Bauer and F. J. Turk, eds., Springer, 189-198.
- Ferraro, R. R., and G. F. Marks, 1995: The development of SSM/I rain rate retrieval algorithms using ground based radar measurements. *J. Atmos. Ocean. Tech.*, 12, 755-770.
- Finn, S. E., 2006: *Rainfall classification using reflectivity structure: validation and application*. MS thesis, Colorado State University.
- Geer, A., and P. Bauer, 2011: Observation errors in all-sky data assimilation. *Quart. J. Roy. Meteor. Soc.*, 00, 1-15.

- Geer, A. J., P. Bauer, and P. Lopez, 2007: Lessons learnt from the 1D+4D-Var assimilation of rain and cloud affected SSM/I observations at ECMWF. Available as ECMWF Tech. Memo. 535, from <http://www.ecmwf.int>.
- Geer, A. J., P. Bauer, and P. Lopez, 2008: Lessons learnt from the operational 1D+4D-Var assimilation of rain and cloud-affected SSM/I observations at ECMWF. *Quart. J. Roy. Meteor. Soc.*, 134, 1513-1525.
- Geer, A. J., P. Bauer, and P. Lopez, 2010: Direct 4D-Var assimilation of all-sky radiances. Part II: Assessment. *Quart. J. Roy. Meteor. Soc.*, 136, 1886-1905.
- Geer, A. J., P. Bauer, and C. W. O'Dell, 2009: A revised cloud overlap scheme for fast microwave radiative transfer in rain and cloud. *J. Appl. Meteor.*, 48, 2257-2270.
- Greco M., and E. N. Anagnostou, 2001: Overland precipitation estimation from the TRMM passive microwave observations, *J. Appl. Meteor.*, 40(8), 1367-1380.
- Grody, N. C., 1991: Classification of snow cover and precipitation using the Special Sensor Microwave/Imager (SSM/I). *J. Geophys. Res.*, 96, 7423-7435.
- Grody, N. C., 1993: Remote sensing of the atmosphere from satellites using microwave radiometry. *Atmospheric remote sensing by microwave radiometry*. 572pp. Editor M. A. Janssen. pp. 259 - 334.
- Grody, N. C., A. Gruber, and W. C. Shen, 1980: Atmospheric water content derived from the Nimbus-6 scanning microwave spectrometer over the tropical Pacific. *J. Appl. Meteorol.* 19, 986-996.
- Hale, G. M. and M. R. Querry, 1973: Optical constants of water in the 200-nm to 200- μ m wavelength region. *Appl. Opt.*, 12(3), 555-563. Doi: 1364/AO.12.000555.
- Heymsfield, G. M., and R. Fulton, 1994a: Passive microwave and infrared structure of mesoscale convective systems. *Meteor. Atmos. Phys.*, 54, 123-139.
- Heymsfield, G. M., and R. Fulton, 1994b: Passive microwave structure of severe tornadic storms on 16 November 1987. *Mon. Wea. Rev.*, 122, 2587-2595.
- Hollinger, J. P., 1989: DMSP Special Sensor Microwave/Imager calibration/validation. Final Report, Vol. I., Space Sensing Branch, Naval Research Laboratory, Washington D. C.
- Hong, Y., C. Kummerow, and W. S. Olson, 1999: Separation of convective and stratiform precipitation using microwave brightness temperature, *J. Appl. Meteorol.*, 38, 1195-1213, doi:10.1175/1520-0450(1999)038<1195:SOCASP>2.0.CO;2.

- Hou, A., G. S. Jackson, C. Kummerow, and C. M. Shepherd, 2008: Global precipitation measurement, in *Precipitation: Advances in Measurement, Estimation, and Prediction*, edited by S. Michaelides, pp. 1-39, Springer, Berlin.
- Houghton, H. G., 1968: On precipitation mechanisms and their artificial modification, *J. Appl. Meteorol.*, 7, 851-859.
- Houze, R. A., Jr., 1993: *Cloud Dynamics*. Academic Press, 573 pp.
- Iguchi, T., T. Kozu, R. Meneghini, J. Awaka, K. Okamoto, 2000: Rain-profiling algorithm for TRMM Precipitation Radar. *J. Appl. Meteorol.*, 39, 2038-2052.
- Karstens, U., C. Simmer, and E. Ruprecht, 1994: Remote sensing of cloud liquid water. *Meteorol. Atmos. Phys.*, 54, 157-171.
- Khairoutdinov, M. F., and D. A. Randall, 2003: Cloud resolving modeling of the ARM summer 1997 IOP: Model formulation, results, uncertainties, and sensitivities. *J. Atmos. Sci.*, 60, 607-625.
- Kidd, C., 1998: On rainfall retrieval using polarization-corrected temperatures. *Int. J. Remote Sens.*, 19, 981-996.
- Kidder, S. Q., and T. H. Vonder Haar, 1995: *Satellite Meteorology: An introduction*. Academic Press, San Diego, 466pp.
- King, M. D., S.-C. Tsay, S. E. Platnick, M. Wang, and K.-N. Liou, 1996: Cloud retrieval algorithms for MODIS optical thickness, effective particle radius, and thermodynamic phase. MODIS Algorithm Theoretical Basis Document ATBD-MOD-05. [Available on-line at <http://eosps0.gsfc.nasa.gov/atbd/modis/atbdmod05new.html>.]
- Kodama, Y. M., H. Okabe, Y. Tomisaka, K. Kotono, Y. Kondo, and H. Kasuya, 2007: Lightning frequency and microphysical properties of precipitating clouds over the Western North Pacific during Winter as derived from TRMM multisensor observations. *Mon. Wea. Rev.*, 135, 2226-2241.
- Kummerow, C., 1993: On the accuracy of the Eddington approximation for radiative transfer in the microwave frequencies. *J. Geophys. Res.*, 98(D2), 2757-2765.
- Kummerow, C., and L. Giglio, 1994: A passive microwave technique for estimating rainfall and vertical structure information from space, Part I: Algorithm description. *J. Appl. Meteorol.*, 33, 3-18.
- Kummerow C., and J. A. Weinman, 1988: Radiative properties of deformed hydrometeors for commonly used passive microwave frequencies. *IEEE Trans on Geo. And Rem. Sens.*, 26(5), 629-638.

- Kummerow, C., H. Masunaga, and P. Bauer, 2007: A next-generation microwave rainfall retrieval algorithm for use by TRMM and GPM. In: *Measuring Precipitation from Space - EURAINSAT and the Future*, V. Levizzani, P. Bauer and F. J. Turk, eds., Springer, 235-252.
- Kummerow, C., W. S. Olson, and L. Giglio, 1996: A simplified scheme for obtaining precipitation and vertical hydrometeor profiles from passive microwave sensors. *IEEE Trans. Geosci. Remote Sens.*, 34, 1213-1232.
- Kummerow, C., W. Berg, J. Thomas-Stahle, and H. Masungana, 2006: Quantifying global uncertainties in a simple microwave rainfall algorithm. *J. Atmos. Ocean. Tech.*, 23, 23-37.
- Kummerow, C., Barnes, W., T. Kozu, J. Shiue, and J. Simpson, 1998: The tropical rainfall measuring mission (TRMM) sensor package. *J. Atmos. Ocean. Tech.*, 15, 809-817.
- Kummerow, C. D., S. Ringerud, J. Crook, D. Randel, and W. Berg, 2011: An observationally generated *a-priori* database for microwave rainfall retrievals. *J. Atmos. Ocean. Tech.*, 28, 113-130.
- Kummerow, C., Y. Hong, W. S. Olson, S. Yang, R. F. Adler, J. McCollum, R. Ferraro, G. Petty, D.-B. Shin, and T. T. Wilheit, 2001: The evolution of the Goddard Profiling Algorithm (GPROF) for rainfall estimation from passive microwave sensors. *J. Appl. Meteor.*, 40, 1801-1820.
- Kummerow, C., and Coauthors, 2000: The status of the Tropical Rainfall Measuring Mission (TRMM) after two years in orbit. *J. Appl. Meteorol.*, 39, 1965-1982.
- Lang, S., W.-K. Tao, R. Cifelli, W. Olson, J. Halverson, S. Rutledge, and J. Simpson, 2007: Improving Simulations of convective systems from TRMM LBA: Easterly and Westerly Regimes. *J. Atmos. Sci.*, 64, 1141-1164.
- Leary, C. A., and R. A. Houze Jr., 1979: The structure and evolution of convection in a tropical cloud cluster. *J. Atmos. Sci.*, 36, 437-457.
- Liebe, H. J., G. A. Hufford, and Mo. G. Cotton, 1993: Propagation modeling of moist air and suspended water/ice particles at frequencies below 1000 GHz. *AGARD Conf. Proc.*, 542, 3.1-3.10.
- Lin, B. and P. Minnis, 2000: Temporal variations of land surface microwave emissivities over the atmospheric radiation measurement program southern Great Plains site. *J. Appl. Meteorol.*, 39(7), 1103-1116.
- Liou K. N., 2002: *An introduction to atmospheric radiation. International Geophysics Series*, Volume 84, 583pp.

- Liu, G., J. A. Curry, and R.-S. Sheu, 1995: Classification of clouds over the western equatorial Pacific Ocean using combined infrared and microwave satellite data, *J. Geophys. Res.*, 100, 13,811-13,826.
- Loftus, A., 2011: Development of a triple-moment bulk hail microphysics scheme for use in investigation of hail sensitivities to aerosols. *Manuscript in preparation*.
- Mahrer, Y., and R. A. Pielke, 1977: A numerical study of the airflow over irregular terrain. *Beitrage zur Physik der Atmosphere*, 50, 98-113.
- Marzano, F. S., A. Mugnai, G. Panegrossi, N. Pierdicca, E. A. Smith, and J. Turk, 1999: Bayesian estimation of precipitating cloud parameters from combined measurements of spaceborne microwave radiometer and radar, *IEEE Trans. Geosci. Remote Sens.*, 37, 596-613.
- Matsui, T., X. Zeng, W.-K. Tao, H. Masunaga, W. S. Olson, S. Lang, 2009: Evaluation of long-term cloud-resolving model simulations using satellite radiance observations and multifrequency satellite sensors. *J. Atmos. Ocean. Tech.* 26, 1261-1274.
- Maxwell-Garnett, J. C., 1904: Colours in Metal Glasses and in Metallic Films. *Philosophical Transactions of the Royal Society of London, Series A*, 203, 385-420.
- McCollum, J. R., and R. R. Ferraro, 2003: Next generation of NOAA/NESDIS TMI, SSM/I, and AMSR-E microwave land rainfall algorithms, *J. Geophys. Res.*, 108(D8), 8382, doi: 10.1029/2001JD001512.
- McFarquhar, G. M., and Coauthors, 2006: Factors affecting the evolution of Hurricane Erin (2001) and the distributions of hydrometeors: role of microphysical processes. *J. Atmos. Sci.*, 63, 127-150.
- Meiold-Mautner, I., C. Prigent, E. Defer, J. R. Pardo, J.-P. Chaboureau, J.-P. Pinty, M. Mech, and S. Crewell, 2007: Radiative transfer simulations using mesoscale cloud model outputs: comparisons with passive microwave and infrared satellite observations for midlatitudes. *J. Atmos. Sci.*, 64, 1550-1568.
- Meyers, M. P., R. L. Walko, J. Y. Harrington, and W. R. Cotton, 1997: New RAMS cloud microphysics parameterization. Part II: The two-moment scheme. *Atmos. Res.*, 45, 3-39.
- Mishchenko, M. I., and L. D. Travis: 1998: Capabilities and limitations of a current FORTRAN implementation of the T-matrix method for randomly oriented rotationally symmetric scatters. *J. Quant. Spectrosc. Radiat. Transfer*, 60, 309-324.
- Mishchenko, M. I., J. W. Hovenier, and L. D. Travis, 2000: *Light Scattering by Nonspherical Particles: Theory, Measurements, and Application*. Academic Press, 690pp.

Mishchenko, M. I., L. D. Travis, and A. A. Lacis, 2002: Scattering, Absorption, and Emission of Light by Small Particles. Cambridge University Press, Cambridge, 486pp. http://www.giss.nasa.gov/~crmim/publications/book_2.pdf

Mugnai, A., E. A. Smith, and G. J. Tripoli, 1993: Foundation of physical-statistical precipitation retrieval from passive microwave satellite measurements. Part II: Emission source and generalized weighting function properties of a time dependent cloud-radiation model. *J. Appl. Meteor.*, 32, 17-39.

Olson, W. S., 1989: Physical retrieval of rainfall rates over the ocean by multispectral radiometry: Application to tropical cyclones. *J. Geophys. Res.*, 94, 2267-2280.

Olson, W. S., Y. Hong, C. D. Kummerow, and J. Turf, 2001: A texture-polarization method for estimating convective-stratiform precipitation area coverage from passive microwave radiometer data, *J. Appl. Meteorol.*, 40, 1577-1591, doi:10.1175/1520-0450(2001)040<1577:ATOMFE>2.0.CO;2.

Olson, W. S., C. D. Kummerow, Y. Hong, and W.-K. Tao, 1999: Atmospheric latent heating distributions in the Tropics derived from passive microwave radiometer measurements. *J. Appl. Meteor.*, 38, 633-664.

Panegrossi, G., and coauthors, 1998: Use of cloud model microphysics for passive microwave-based precipitation retrieval: significance of consistency between model and measurement manifolds. *J. Atmos. Sci.*, 55, 1644-1673.

Parker, M. D., and R. H. Johnson, 2004: Structures and dynamics of quasi-2D mesoscale convective systems. *J. Atmos. Sci.*, 61, 545-567.

Petty, G. W., 1994: Physical retrievals of over-ocean rain rate from multichannel microwave imagery. Part I: Theoretical characteristics of normalized polarization and scattering indices. *Meteor. Atmos. Phys.*, 54, 79-99.

Petty, G. W., 2006: *A first course in atmospheric radiation*. Sundog Publishing, Madison, Wisconsin, 460pp.

Petty, G. W., and J. Turk, 1996: Observed multichannel microwave signatures of spatially extensive precipitation in tropical cyclones. Preprints, *Eighth Conf. on Satellite Meteorology and Oceanography*, Atlanta, GA, Amer. Meteor. Soc., 291-294.

Prabhakara, C., R. Iacovazzi Jr., and J. M. Yoo, 2001: TRMM observations of polarization difference in 85 GHz: information about hydrometeors and rain rate. *J. of the Meteor. Soc. of Japan*, 79, 701-707.

Prigent, C. F. Aires, and W. B. Rossow, 2006: Land surface microwave emissivities over the globe for a decade. *Bull. Amer. Meteorol. Soc.*, 87(11), 1573-1584.

- Prigent, C., W. B. Rossow, and E. Matthews, 1997: Microwave land surface emissivities estimated from SSM/I observations. *J. Geophys. Res.*, 102(D18), 21867-21890.
- Prigent, C., J. R. Pardo, M. I. Mishchenko, W.B. Rossow, 2001: Microwave polarized scattering signatures in clouds: SSM/I observations with radiative transfer simulations. *J. Geophys. Res.*, 106, 28243-28258.
- Rabier, F., H. Jarvinen, E. Klinker, J. F. Mahfouf, and A. Simmons, 2000: The ECMWF operational implementation of four-dimensional variational assimilation. I: Experimental results with simplified physics. *Quart. J. Roy. Meteor. Soc.* 126, 1148-1170.
- Randall, D. A., M. Khairoutdinov, A. Arakawa, and W. Grabowski, 2003: Breaking the cloud parameterization deadlock. *Bull. Amer. Meteor. Soc.*, 84, 1547-1564.
- Randall, D. A., K.-M. Xu, R. J. C. Somerville, and S. Iacobellis, 1996: Single-column models and cloud ensemble models as links between observations and climate models. *J. Climate*, 9, 1683-1697.
- Rapp, A. D., C. Kummerow, W. Berg, and B. Griffith, 2005: An evaluation of the proposed mechanism of the adaptive infrared Iris hypothesis using TRMM VIRS and PR measurements. *J. Climate*. 18, 4185-4194.
- Reynolds, R. W., N. A. Rayner, T. M. Smith, D. C. Strokes, and W. Wang, 2002: An improved in situ and satellite SST analysis for climate. *J. Climate*, 15, 1609-1625.
- Rickenbach, T. M., R. N. Ferreira, J. B. Halverson, D. L. Herdies, and M. A. F. Silva Dias, 2002: Modulation of convection in the southwestern Amazon basin by extratropical stationary fronts, *J. Geophys. Res.*, 107(D20), 8040, doi:10.1029/2000JD000263.
- Roberti, L., and C. Kummerow, 1999: Monte Carlo calculations of polarized microwave radiation emerging from cloud structures. *J. Geophys. Res.*, 104, 2093-2104.
- Rodgers, C. D., 2000: *Inverse Methods for Atmospheric Sounding: Theory and Practise*. World Scientific Publishing, Co., River Edge, NJ.
- Schols, J., J. Haferman, J. Weinman, C. Prabhakara, M. Cadeddu, and C. Kummerow, 1997: Polarized microwave radiation model of melting deformed hydrometeors. Preprints, *Ninth Conf. on Atmospheric Radiation*, Long Beach, CA, Amer. Meteor. Soc., 270-273.
- Skamarock, W. C., M. L. Weisman, and J. B. Klemp, 1994: Three-dimensional evolution of simulated long-lived squall lines. *J. Atmos. Sci.*, 51, 2563-2584.

- Smith, E. A., X. Xiang, A. Mugnai, and G. Tripoli, 1994: Design of an inversion-based precipitation profile retrieval algorithm using an explicit cloud model for initial guess microphysics. *Meteor. Atmos. Phys.*, 54, 53-78.
- Smith, E. A., and Coauthors, 1992: Foundations for statistical-physical precipitation retrieval from passive microwave satellite measurements. Part I: Brightness-temperature properties of a time-dependent cloud-radiation model. *J. Appl. Meteor.*, 31, 506-531.
- Spencer, R. W., H. M. Goodman, and R. E. Hood, 1989: Precipitation retrieval over land and ocean with SSM/I: Identification and characteristics of the scattering signal. *J. Atmos. Oceanic Technol.*, 6, 254-273.
- Spencer, R. W., B. B. Hinton, and W. S. Olson, 1983: Nimbus-7 37 GHz radiances correlated with radar rain rates over the Gulf of Mexico. *J. Clim. Appl. Meteor.*, 22, 2095-2099.
- Spencer, R. W., D. W. Martin, B. B. Hinton, and J. A. Weinman, 1983: Satellite microwave radiances correlated with radar rain rates over land. *Nature*, 304, 141-143.
- Srivastava, R., 1978: Parameterization of raindrop size distributions. *J. Atmos. Sci.*, 35, 108-117.
- Tao, W.-K., and J. Simpson, 1989: Modeling study of a tropical squall-type convective line. *J. Atmos. Sci.*, 46, 177-202.
- Tremback, C. J., G. J. Tripoli, and W. R. Cotton, 1985: A regional scale atmospheric numerical model including explicit moist physics and a hydrostatic time-split scheme. Preprints, 7th Conference on Numerical Weather Prediction, June 17-20, 1985, Montreal, Quebec, AMS.
- Tripoli, G. J., and W. R. Cotton, 1982: The Colorado State University three-dimensional cloud/mesoscale model--1982. Part I: General theoretical framework and sensitivity experiments. *J. de Rech. Atmos.* 16, 185-220.
- Troitsky, A. V., A. M. Osharin, A. V. Korolev, and J. W. Strapp, 2003: Polarization of thermal microwave atmospheric radiation due to scattering by ice particles in clouds. *J. Atmos. Sci.*, 60, 1608-1620.
- Tsang, L., J. A. Kong, and R. T. Shin, *Theory of Microwave Remote Sensing*, Wiley, New York, 1985.
- Turk, J., and J. Vivekanandan, 1995: Effects of hydrometeor shape and orientation upon passive microwave brightness temperature measurements. *Microwave Radiometry and Remote Sensing of the Environment*, D. Solimini, Ed., VSP Press, pp. 187-196.

- Ulaby, F. T., Moore, R. K., and Fung, A. K., 1981: *Microwave Remote Sensing, Active and Passive*. Volume I: Microwave Remote Sensing Fundamentals and Radiometry. Addison- Wesley, 456pp.
- Van Den Heever and Cotton, 2004: The impact of hail size on simulated supercell storms. *J. Atmos. Sci.*, 61, 1596-1609.
- Varma, A. K., and G. Liu, 2010: On classifying rain types using satellite microwave observations. *JGR*, 115, doi:10.1029/2009JD012058.
- Walko, R. L., W. R. Cotton, M. P. Meyers, and J. Y. Harrington, 1995: New RAMS cloud microphysics parameterization: Part I: The single-moment scheme. *Atmos. Res.*, 38, 29-62.
- Warren, S. G., 1984: Optical constants of ice from the ultraviolet to the microwave. *Appl. Opt.*, 23, 1206-1225.
- Waterman, P., 1965: Matrix formulation of electromagnetic scattering. *Proc. IEEE*, 53, 805-812.
- Waterman, P., 1971: Symmetry, unitary and geometry in electromagnetic scattering. *Phys. Rev. D*3, 825-839.
- Weng, F., B. Yan, and N. C. Grody, 2001: A microwave land emissivity model. *J. Geophys. Res.*, 106 (D17), 20115-20123.
- Wiedner, M., C. Prigent, J. R. Pardo, O. Nuissier, J.-P. Chaboureau, J.-P. Pinty, and P. Mascart, 2004: Modeling of passive microwave responses in convective situations using output from mesoscale models: comparison with TRMM/TMI satellite observations. *J. Geophys. Res.*, 109(D06214), doi:10.1029/2003JD004280.
- Wilheit, T. T., 1979: A model for the microwave emissivity of the ocean's surface as a function of wind speed. *IEEE Trans. Geosci. Electron.*, 17, 244-249.
- Wilheit, T. T., A. T. C. Chang, and L. S. Chiu, 1991: Retrieval of monthly rainfall indices from microwave radiometric measurement using probability distribution functions. *J. Atmos. Ocean. Tech.*, 8, 118-136.
- Wu, R., and J. A. Weinman, 1984: Microwave radiances from precipitating clouds containing aspherical ice, combined phase, and liquid hydrometeors. *J. Geophys. Res.*, 89, 7170-7178.
- Zeng, X., W. K. Tao, S. Lang, A. Y. Hou, M. Zhang, and J. Simpson, 2008: On the sensitivity of atmospheric ensemble states to cloud microphysics in long-term cloud-resolving model simulations. *J. Meteor. Soc. Japan*, 86A, 45-65.

Zhou, Y. P., W.-K. Tao, A. Y. Hou, W. S. Olson, C.-L. Shie, K.-M. Lau, D.-D. Chou, X. Lin, and M. Grecu, 2007: Use of high-resolution satellite observations to evaluate cloud and precipitation statistics from cloud-resolving model simulations. Part I: South China Sea Monsoon Experiment. *J. Atmos. Sci.*, 64, 4309-4329.

Ziper, E. J., 1977: Mesoscale and convective-scale downdrafts as distinct components of squall-line circulation. *Mon. Wea. Rev.*, 105, 1568-1589.

APPENDIX A

IMPLEMENTATION OF T-MATRIX TO THE EDDINGTON RTM FOR STRATIFORM/CONVECTIVE SEPARATION

A.1 Introduction

A.1.1 Observed Polarization Signals in Stratiform Clouds

Clouds and precipitation can be broadly categorized in two major types, namely convective and stratiform. It is well known that convective precipitation regions are associated with vigorous turbulent updrafts and downdrafts with high rain rates, while stratiform regions are associated with relatively weak updrafts and downdrafts and light to moderate rain rates (Zipser 1977; Leary and Houze 1979; Houze 1993). They both produce distinct heating profiles and convective rain heats up the entire troposphere while stratiform rain heats the upper layers but cools down the lower layers of the troposphere (Tao and Simpson 1989). The primary microphysical process responsible for convective rainfall is the collection of cloud water by rain particles, or riming in the strong updraft; while the primary microphysical process responsible for stratiform clouds and rainfall is vapor deposition on ice particles, or aggregation (Houghton 1968). The partition between the two is important to understand with regard to clouds and the associated microphysics and thermodynamics, and their impacts on tropical hydrological and energy cycles.

Furthermore, rain type information is important in the microwave rainfall retrieval algorithms (Kummerow et al. 1996; Kummerow et al. 2000). Therefore, convective/stratiform separation is of great significance and relevance.

The focus of the current work is on microwave observations. Several partition algorithms have been developed using passive microwave observations including Liu et al. (1995), Anagnostou and Kummerow (1997), Hong et al. (1999), Olson et al. (2001), and Varma and Liu (2010), among some of which the polarization information at 85 GHz has been utilized. Olson et al. (1999) also utilized the approximate inverse relationship between 85.5-GHz polarization difference and the convective fraction to constrain retrievals of precipitation and latent heating from SSM/I observations.

Spencer et al. (1989) and Heymsfield and Fulton (1994a,b) found that over land, SSM/I observations at 85 GHz differed between vertical and horizontal polarizations on the order of 5 K or greater in stratiform precipitation regions, while in regions of strong convection, 85 GHz is nearly unpolarized. Without physical verifications, they hypothesized that the polarization was caused by the precipitation-sized ice particles in the stratiform clouds, such as snow and aggregates, which tend to be oriented horizontally when falling through the relatively weak vertical motions. The orientation then results in preferential scattering in the horizontal polarization; whereas vigorous updrafts in convective regions could lead to the potential tumbling of ice hydrometeors whose preferred orientation would be lost, and, therefore, similar scattering signatures in both polarizations would be produced. Prabhakara et al. (2001) also explored the relationship between an 85-GHz polarization difference, hydrometeors, and rain rates.

A.1.2 Sensitivity of Polarization to Nonspherical Ice Particle Properties

Microwave radiative transfer calculations have been performed over the oriented aspherical ice hydrometeors in the clouds to test the above hypothesis (Turk and Vivekanandan 1995; Petty and Turk 1996; Schols et al. 1997). Polarization differences of greater than 5 K in 85 GHz for these oriented particles have been found to support this hypothesis. Similar polarization differences are also obtained in Roberti and Kummerow (1999) using a Monte Carlo model and their results suggest that besides ice particle orientation, the relative amounts of asymmetric snow and more spherical graupel in different regimes could also be contributing to the observed differences.

Troitsky et al. (2003) investigated the polarization of thermal microwave atmospheric radiation due to scattering by ice particles in clouds during the Alliance Icing Research Project in Ottawa, Canada during the winter of 1999/2000. They found that the magnitude of the polarization difference depended on the ice water path and had no correlation with the liquid water path, while the microwave radiation intensity was determined by the liquid water path. They also found a relationship between the polarization differences at 37 and 85 GHz and the cloud microstructure including ice crystal shapes and characteristic sizes.

A number of theoretical studies (e.g., Czekala 1998; Evans and Vivekanandan 1990; Evans and Stephens 1995; Turk and Vivekanandan 1995; Prigent et al. 2001) have discussed the polarization of microwave radiation by nonspherical particles and a detailed review can be found in Mishchenko et al. (2000). Their findings indicate that the emergent polarized brightness temperature will contain not only information on the total

ice water path, but also information on the microphysics including size, shape/asphericity, orientation, and density of the ice particles.

The current Eddington RTM uses scattering properties determined from Mie theory and thus assumes that all hydrometeor species are spherical. Therefore, to simulate the observed polarization signature from nonspherical ice particles at higher microwave frequencies, nonspherical particles must be assumed in the calculation of the scattering properties to account for the difference in the vertical and horizontal polarizations. Therefore, the T-matrix method has been implemented in this work.

A.2 Implementation of the T-matrix Method in the Eddington RTM

A.2.1 Eddington Approximation and Mie Scattering

Two stream or Eddington approximations are used in many general circulation and climate models to parameterize the radiative transfer processes due to their efficient computation, which is critical to model simulations (Liou 2002). Eddington's approximation uses a similar approach to that of the two-stream approximation and was originally used for studies of radiative equilibrium in stellar atmospheres (Eddington 1916). In Eddington's approximation, both the intensity I and phase function P are expanded in Legendre polynomial terms:

$$I(z, \theta, \phi) = I_0(z) + I_1(z) \cos \theta + \dots \quad (\text{A.1})$$

$$P(\cos \Theta) = 1 + 3g \cos \Theta + \dots \quad (\text{A.2})$$

where θ is the zenith angle, ϕ is the azimuth angle, and Θ is the scattering angle.

The approximation can reproduce T_b s quite well compared to discrete ordinate models with multiple streams (Kummerow 1993). Furthermore, T_b errors from the uncertainty of input parameters are much larger than the ones from the approximations of the radiative transfer code.

For particles with large size parameters whose phase functions have forward diffraction peaks, their peaks cannot be accurately reproduced using a sum of just the low-order terms in the expansion. A Dirac δ -function is introduced to represent the forward peak and the phase function P is expressed as:

$$P(\cos\Theta) \approx AP'(\cos\Theta) + 4B\delta(\cos\Theta - 1) \quad (\text{A.3})$$

where Θ is the scattering angle, $P'(\cos\Theta)$ is the δ -scaled phase function, and coefficients A and B determine how the total phase function is partitioned between the two items. Subsequently, the asymmetry factor g , optical depth τ , and single-scattering albedo $\tilde{\omega}$ are adjusted using the similarity principle to get:

$$g' = \frac{g - B}{1 - B} \quad (\text{A.4})$$

$$\tau' = (1 - B\tilde{\omega})\tau \quad (\text{A.5})$$

$$\tilde{\omega}' = \left(\frac{1 - B}{1 - B\tilde{\omega}}\right)\tilde{\omega} \quad (\text{A.6})$$

δ -Eddington approximation is adequate enough to handle the brightness temperature calculations for the satellite measured microwave frequencies applied in the current study.

Hydrometeors are generally assumed spherical so that Lorenz-Mie scattering can be applied and solutions can be attained from solving the Maxwell equations including the extinction efficiency

$$Q_e = \frac{2}{x^2} \sum_{n=1}^{\infty} (2n+1) \text{Re}(a_n + b_n) \quad (\text{A.7})$$

and the scattering efficiency

$$Q_s = \frac{2}{x^2} \sum_{n=1}^{\infty} (2n+1) (|a_n|^2 + |b_n|^2) \quad (\text{A.8})$$

where x is the size parameter and a_n and b_n are the Mie scattering coefficients that are expressed in spherical Bessel functions, which are functions of size parameter x and refractive index m .

However, the polarization difference described in Section A.1.2 cannot be captured under the Mie assumption and, therefore, scattering from nonspherical particles must be included. The T-matrix method was used in the Eddington framework (Kummerow and Weinman 1988; Wu and Weinman 1984) to explain the observed polarization differences without sacrificing computational efficiency. The most up-to-date T-matrix algorithm is developed by Mishchenko (http://www.giss.nasa.gov/staff/mmishchenko/t_matrix.html) and its recent improvements have made this method applicable to size parameters exceeding 100. The algorithm and its implementation in the Eddington RTM framework is both described and documented below.

A.2.2 *T-Matrix Method*

Based on numerically solving Maxwell's equations, the T-matrix method is a powerful exact technique for calculating light scattering by nonspherical particles. It was initially introduced by Waterman (1965, 1971) for computing electromagnetic scattering by single, homogeneous nonspherical particles based on the Huygens principle, which states that any point on a wave front of light may be regarded as the source of secondary

waves and that the surface that is tangent to the secondary waves can be used to determine the future position of the wave. The standard scheme to compute the T matrix for single homogeneous scatters in the particle reference frame is based on the Extended Boundary Condition Method (EBCM). It produces identical results to the Mie scheme in spherically symmetric cases. In many applications, it compares favorably with other techniques with respect to efficiency, accuracy, and size parameter range (Mishchenko 2000).

In the case of the scattering of a plane electromagnetic wave by a single nonspherical particle in a fixed orientation with respect to the reference frame, the incident and the scattered fields (E^{inc} and E^{sca}) can be expanded in vector spherical wave functions RgM_{mn} , RgN_{mn} , M_{mn} , and N_{mn} as follows:

$$E^{inc}(R) = \sum_{n=1}^{\infty} \sum_{m=-n}^n [a_{mn} RgM_{mn}(kR) + b_{mn} RgN_{mn}(kR)] \quad (\text{A.9})$$

$$E^{sca}(R) = \sum_{n=1}^{\infty} \sum_{m=-n}^n [p_{mn} M_{mn}(kR) + q_{mn} N_{mn}(kR)], \quad |R| > r_0 \quad (\text{A.10})$$

where a_{mn} , b_{mn} , p_{mn} , and q_{mn} are the expansion coefficients, k is the free-space wavenumber, and r_0 is the radius of a circumscribing sphere of the scattering particle. Because of the linearity of Maxwell's equations and boundary conditions, the coefficients for the scattered field and for the incident field also has a linear relationship and can be expressed by a transition matrix (or T-matrix) T:

$$p_{mn} = \sum_{n'=1}^{\infty} \sum_{m'=-n'}^{n'} [T_{mm'n'n'}^{11} a_{m'n'} + T_{mm'n'n'}^{12} b_{m'n'}] \quad (\text{A.11})$$

$$q_{mn} = \sum_{n'=1}^{\infty} \sum_{m'=-n'}^{n'} [T_{mm'n'n'}^{21} a_{m'n'} + T_{mm'n'n'}^{22} b_{m'n'}], \quad (\text{A.12})$$

which can be compactly written as:

$$\begin{bmatrix} p \\ q \end{bmatrix} = \mathbf{T} \begin{bmatrix} a \\ b \end{bmatrix} = \begin{bmatrix} T^{11} & T^{12} \\ T^{21} & T^{22} \end{bmatrix} \begin{bmatrix} a \\ b \end{bmatrix} \quad (\text{A.13})$$

This equation lays down the basis of the T-matrix method. Given a_{mn} and b_{mn} calculated from the incident wave and the knowledge of the T matrix for the given scatter, the scattered field $E^{sca}(R)$ can be calculated using equations (A.10), (A.11), and (A.12). The T matrix can be computed using the above-mentioned EBCM, for further details refer to Tsang et al. (1985) and Mishchenko and Travis (1998). A fundamental feature of the T-matrix approach is that it depends only on the physical and geometrical characteristics of the scattering particle (shape, size, and refractive index) and is completely independent of the incident and scattered field (Mishchenko et al. 2000).

A.2.3 Implementation of the T-Matrix Algorithm in the RTM

The Mishchenko's double-precision T-matrix code for nonspherical particles with a fixed orientation provides results only for a single particle. The following tables document the output and input parameters of the code.

Table A.1 Output parameters of the T matrix code.

Parameter	
S11,S12,S21,S22	Elements of the amplitude matrix
Z11,Z12,Z13,Z14 Z21,Z22,Z23,Z24 Z31,Z32,Z33,Z34 Z41,Z42,Z43,Z44	Elements of the phase matrix

Table A.2 Input parameters of the T matrix code.

Parameter	
AXI	Equivalent-sphere radius
RAT	=1 – the size of the particles is specified in terms of the equal-volume-sphere radius. ≠1 – the size of the particles is specified in terms of the surface-equivalent-sphere radius
LAM	Wavelength of incident light
MRR & MRI	Real and imaginary parts of the refractive index
NP & EPS	Specify the shape of the particles: NP = -1: spheroids (EPS is the ratio of the horizontal to rotational axes. EPS>1 for oblate spheroids and EPS<1 for prolate spheroids) NP = -2: cylinders (EPS is the ratio of the diameter to the length) NP > 0: Chebyshev particles with NP as the degree of the Chebyshev polynomial (EPS is the deformation parameter) NP = -3: generalized Chebyshev particles (describing the shape of distorted water drops.)
DDELTA	Desired absolute accuracy of computing the expansion coefficients
NDGS	Parameter controlling the number of division points in computing integrals over the particle surface.
ALPHA & BETA	Euler angles (in degrees) specifying the orientation of the scattering particle relative to the laboratory reference frame.
THETA0	Zenith angle of the incident beam in degrees
THETA	Zenith angle of the scattered beam in degrees
PHI0	Azimuth angle of the incident beam in degrees
PHI	Azimuth angle of the scattered beam in degrees

For a single scatterer, given size, wavelength, shape, refractive index, incidence angles, and orientation angles, the extinction cross section C_e , scattering cross section C_s , and asymmetry parameter g for the given polarization can be calculated from the following formulas:

$$C_e = -\frac{1}{k_1^2 |E_0^{inc}|^2} \text{Re} \sum_{n=1}^{\infty} \sum_{m=-n}^n [a_{mn} (p_{mn})^* + b_{mn} (q_{mn})^*] \quad (\text{A.14})$$

$$C_s = -\frac{1}{k_1^2 |E_0^{inc}|^2} \text{Re} \sum_{n=1}^{\infty} \sum_{m=-n}^n [|p_{mn}|^2 + |q_{mn}|^2] \quad (\text{A.15})$$

$$g = \langle \cos \Theta \rangle = \frac{1}{4\pi} \int_{4\pi} d\hat{r} P(\hat{r}, \hat{n}^{inc}) \hat{r} \cdot \hat{n}^{inc} = \frac{1}{C_s} \int_{4\pi} d\hat{r} \frac{dC_s}{d\Omega} \hat{r} \cdot \hat{n}^{inc} \quad (\text{A.16})$$

where,

k_l is the wave number in the surrounding media,

Θ is the angle between the incidence \hat{n}^{inc} and scattering directions \hat{r} ,

P is the phase function, and

Ω is the solid-angle field of view of the detector.

The expansion coefficients a_{mn} , b_{mn} , p_{mn} , and q_{mn} are functions of the polarization.

Refer to 5.18a, 5.18b, 2.169 in Mishchenko et al. (2002) for details.

Same as the integration over size in the Mie code, ensemble averaging over particle shapes, sizes, and orientations have to be performed for each hydrometeor species at each layer. The interface to the radiative transfer calculation requires the ensemble averaged volume extinction coefficient $\langle k_e \rangle$, single-scattering albedo $\langle \omega \rangle$, and asymmetry parameter $\langle g \rangle$ for the Eddington approximation.

C_e , C_s , and g are ensemble averaged over size r , and orientation angles α and β to get the volume coefficients. Taking the extinction coefficients k_e as an example:

$$\langle k_e \rangle = \int_{r_{\min}}^{r_{\max}} \int_{\alpha_{\min}}^{\alpha_{\max}} \int_{\beta_{\min}}^{\beta_{\max}} C_e(r, \alpha, \beta) \sin \beta d\beta \cdot d\alpha \cdot n(r) dr, \quad (\text{A.17})$$

where $n(r)$ is the particle size distribution. By using the appropriate normalized quadrature formulas, the calculation is carried out as:

$$\langle k_e \rangle = \sum_{i=1}^{n_r} w_{r,i} n(r_i) \sum_{j=1}^{n_\alpha} w_{\alpha,j} \sum_{k=1}^{n_\beta} w_{\beta,k} C_e(r_i, \alpha_j, \beta_k) \sin \beta_k, \quad (\text{A.18})$$

where w is the corresponding weighting coefficient. $\langle k_s \rangle$ can be computed in the same manner using C_s . With $\langle k_e \rangle$ and $\langle k_s \rangle$ calculated,

$$\langle \omega \rangle = \langle k_s \rangle / \langle k_e \rangle . \quad (\text{A.19})$$

To calculate $\langle g \rangle$, the orientation averaged scattering cross section $\langle C \rangle_{\text{orient}}$ and asymmetry parameter $\langle g \rangle_{\text{orient}}$ needs to be calculated first.

$$\langle g \rangle = \frac{1}{\langle k_s \rangle} \sum_{i=1}^{n_r} \omega_{r,i} n(r_i) \langle C_{s,i} \rangle_{\text{orient}} \langle g_i \rangle_{\text{orient}} . \quad (\text{A.20})$$

With $\langle k_e \rangle$, $\langle \omega \rangle$, and $\langle g \rangle$ available for each layer for both incident vertical and horizontal polarization, the Eddington RTM is then applied to simulate the brightness temperature at both polarizations to compute the differences. Examples are shown in the following section.

A.3 Examples

The polarization signal is assumed to originate only from the snow particles, and, therefore, the T-matrix code replaces the Mie code for snow only. It is worthwhile to note that the definition of snow in the current case includes both snow and aggregates particles. The specification of the input parameters for the particular implementation is described below.

1) Particle Size

The particle size distribution for snow is assumed to be exponential:

$$n(D) = n_0 e^{-\lambda D}, \quad (\text{A.21})$$

where D is the diameter, $n(D)$ is the particle number density per diameter increment, n_0 is the distribution intercept, and λ is the slope of the distribution. n_0 is prescribed as 10^8 m^{-4} for snow. Given snow water content at each level together with n_0 , λ is constrained.

In the code, $RAT = 1$ to specify the radius to be equal-volume-sphere radius, and AXI ranges from $25 \mu\text{m}$ to 1 cm .

2) Particle Shape

Snow particles are assumed to be symmetric oblate spheroids with $NP = -1$ and $EPS = 1.5$ or 3 .

3) Refractive index

Snow particles are assumed to be mixtures of ice and air. With snow density prescribed as 0.1 kg m^{-3} , ice fraction can be calculated. The Maxwell–Garnett formula (Maxwell-Garnett 1904) is then used to calculate the effective permittivity of the mixture using the fraction. The MRR and MRI of the refractive index can then be obtained.

4) Orientation

The snow particles are assumed to be primarily horizontally oriented with an oscillation canting angle of 20° . Therefore, $ALPHA$ ranges between 0° and 360° , and $BETA$ ranges between 0° and 20° .

5) Other parameters

For the Eddington approximation, $\cos(\text{THET0}) = 0.5$, $\cos(\text{THET}) = 0.5$, $\text{PHI0} = 0^\circ$, and PHI is ranged from 0° to 360° to obtain an azimuthal average. For the current calculations, $\text{DDEL T} = 0.001$ and $\text{NDGS} = 2$, which are the recommended values for compact particles. In this work, Gauss-Legendre quadrature is applied for integration over angles (the coefficients are normalized), and trapezoid rule is used for integration over sizes in the current work.

In the implementation, subroutine `MISH_TMATRIX()` calculates the T matrix and saves it as a global variable. Subroutine `MISH_SCAT_PROPS2()` calculates C_e , C_s ,

and g for a single α and β at both vertical and horizontal polarizations. The subroutine `AVG_SCAT_PROPS2 ()` calculates the orientation (ALPHA and BETA) ensemble averaged efficiencies $\langle k_e \rangle$, $\langle k_s \rangle$, and $\langle g \rangle$. Finally, `TMATRIX_SNOW ()` performs the size integration. The vertical and horizontal polarizations are calculated by separate calls to the RTM. A subsample of simulation results are shown below.

A.3.1 Polarization Difference over One Profile

Figure A.1 shows the selected profiles over land that will be tested. The snow layer is expected to produce a polarization signal. RTM is set to simulate T_{bs} for TMI

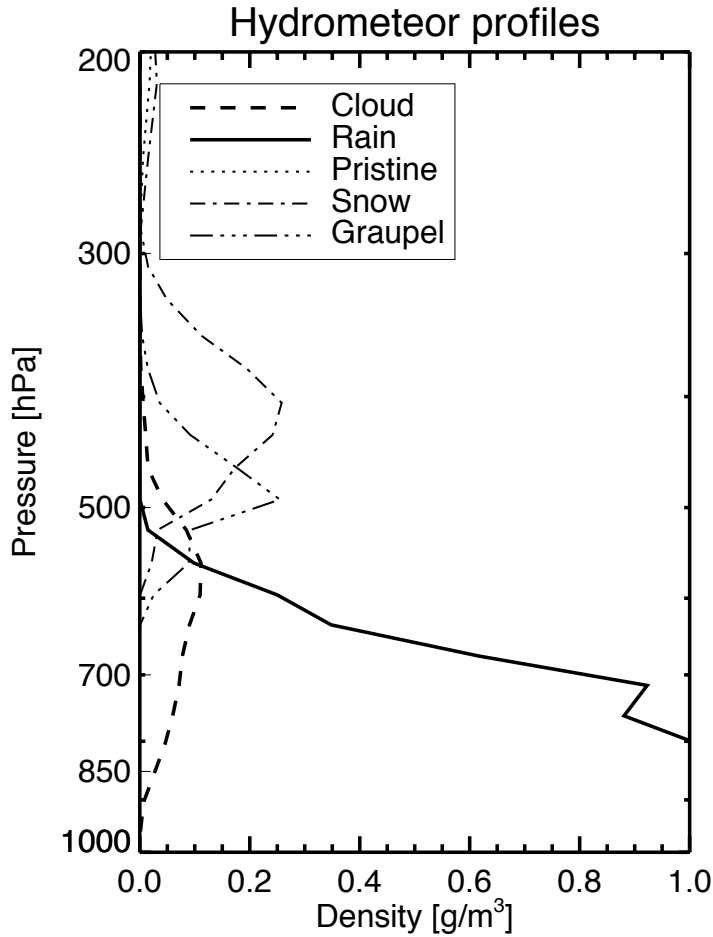


Figure A.1 The selected raining scene to test the implementation.

with a viewing angle of 53.1° . Since scattering is significant only in higher microwave frequencies, T_b differences in 37 and in 85 GHz are compared. Table A.3 enumerates the comparison between using the Mie code and the T-matrix code. Note that the results do not consider the melting of particles in the RTE.

Table A.3 T_b s for 37 and 85 GHz using Mie code and T-matrix code individually.

Case	T_b (K)	37H	37V	85H	85V
1 (snow only)	Mie	274.06	274.06	271.50	271.50
2 (snow only)	T-matrix (sphere) EPS = 1.000001	274.06	274.06	271.50	271.50
3 (snow only)	T-matrix (nonspherical) EPS = 1.5	274.09	274.06	272.24	271.53
4 (snow only)	T-matrix (nonspherical) EPS = 3	274.18	274.10	273.97	272.41
5 (snow only)	T-matrix (nonspherical) EPS = 1.5 Snow \times 5	267.63	267.11	238.24	233.30
6 (all hydrometeors)	Mie	256.10	256.10	237.45	237.45
7 (all hydrometeors)	T-matrix (nonspherical) EPS = 1.5	256.13	256.10	238.00	237.49
8 (all hydrometeors)	T-matrix (nonspherical) EPS = 1.5 Snow \times (1/2)	256.47	256.46	241.80	241.75

A.3.2 Discussion

Cases 1 through 5 only consider the existence of snow particles in Figure A.1 by removing all of the other hydrometeor species and, therefore, the extinction of the radiation originates from atmospheric gases and snow, while cases 6, 7, and 8 take into account all of the species. Here we focus on T_b s in 37 and 85 GHz because polarization signals are more noticeable in higher frequencies, and, therefore, the role of scattering is more important in the extinction process.

In case 1, the T_{bs} are calculated under the Mie assumption that the snow particles are assumed to be spherical. Therefore, no polarization signal is produced from isotropic scattering. To validate the T-matrix implementation, in case 2, the T_{bs} are calculated using the T-matrix code by assuming spherical snow (the aspect ratio EPS is set to 1.000001 instead of 1 to avoid potential rare case overflow problems). In cases 1 and 2, T_{bs} converge to meet the same results, confirming the correct implementation of the T-matrix to the Eddington RTM.

In case 3, the nonspherical snow particles are assumed to be oblate spheroids with an aspect ratio of 1.5. As the oscillation angles of these particles are constrained within 20° , the upwelling radiation is polarized by the horizontally oriented spheroids and a difference of 0.71 K is produced in 85 GHz T_b . However, the scattering difference is not significant enough in 37 GHz and only produces a 0.03 K difference. Increased nonsphericity and increased snow content both are expected to increase the polarization signal and they are tested individually. In case 4, the aspect ratio is increased to 3 so that each snow particle becomes a more effective polarizer. In this scenario, differences in 85 GHz increase to 1.56 K and in 37 GHz increase slightly up to 0.08 K. In case 5, when the snow water content is increased five fold at each level, the polarization reaches 4.94 K at 85 GHz and 0.52 K at 37 GHz. Therefore, both increasing the snow aspect ratio and increasing the snow content can increase the polarization signals, as expected.

When all of the hydrometeors are included in the calculation of case 7, T_{bs} drop substantially. Assuming a 1.5 aspect ratio for the snow, a 0.51 K polarization signal in 85 GHz is produced compared to the 0.71 K in case 3. The 0.2 K decrease is caused by the decreased upwelling radiation below the snow layer. In case 8, when the snow content is

reduced to half of the original content at each level, the 85-GHz polarization signal is negligible.

Of the above tested cases, case 5 is more representative of a stratiform cloud with an abundance of snow, and case 8 is more representative of a convective cloud with a large amount of graupel and hail. The difference between these two cases strongly suggests the ability of this implemented code to cope with the stratiform/convective separation.

The quadrature integrations of ALPHA, BETA, THETA, and PHI are extraordinarily time consuming, which as a result prevents the immediate use of the code. Therefore, to utilize the T-matrix code efficiently in the future applications, look-up tables must be built offline to speed up the calculations. For each frequency, the extinction coefficient, single scattering albedo, and asymmetry parameter should be tabulated as a function of refractive index, parameters controlling the size distribution, shape parameter, and orientation with respect to the reference frame. This will be performed in future work.

LIST OF ABBREVIATIONS

1D	One-dimensional
4D	Four-dimensional
AMSR-E	Advanced Microwave Scanning Radiometer – Earth Observing System
CRM	Cloud Resolving Model
CSU	Colorado State University
CWP	Cloud Water Path
DMSR	Defense Meteorological Satellite Program
DPR	Dual-frequency Precipitation Radar
dT_b	the T_b difference between 37v and 85v
EBCM	Extended Boundary Condition Method
ECMWF	European Centre for Medium-Range Weather Forecasts
FG	First Guess
FWHM	Full Width at Half Maximum
GCM	Global Climate Model
GMI	GPM Microwave Imager
GPM	Global Precipitation Mission
GPROF	Goddard PROFiling algorithm
IFS	Integrated Forecasting System
IWC	Ice Water Content

IWP	Ice Water Path
LWC	Liquid Water Content
LWP	Liquid Water Path
LT	Local Time
MODIS	Moderate Resolution Imaging Spectroradiometer
PR	Precipitation Radar
PSD	Particle Size distribution
RAMS	Regional Atmospheric Modeling System
RTE	Radiative Transfer Equation
RTM	Radiative Transfer Model
RTTOV-SCATT	Radiative Transfer for the TIROS Operational Vertical Sounder SCATTering
RWP	Rain Water Path
SSM/I	Special Sensor Microwave/Imager
SST	Sea Surface Temperature
T_b	Brightness temperature
$T_b(37)$	T_{bs} at 37 GHz
$T_b(85)$	T_{bs} at 85 GHz
TMI	TRMM Microwave Imager
TOA	Top Of Atmosphere
TPW	Total Precipitable Water
TRMM-LBA	Tropical Rainfall Measuring Mission – Large-scale Biosphere Atmosphere
TWP	Total Water Path

USGS	U.S. Geological Survey
UTC	Coordinated Universal Time
VIRS	Visible and Infrared Scanner